UNIVERSITY OF SOUTHAMPTON

FACULTY OF ENGINEERING AND THE ENVIRONMENT

School of Engineering Sciences

CFD MODELLING OF THE THERMAL DEGRADATION OF BIOMASS IN FLUIDIZED BEDS

by

NANHANG DONG

Thesis for the degree of Doctor of Philosophy

July 2014

UNIVERSITY OF SOUTHAMPTON

ABSTRACT

FACULTY OF ENGINEERING AND THE ENVIRONMENT

School of Engineering Sciences

Doctor of Philosophy

CFD MODELLING OF THERMAL DEGRADATION OF BIOMASS IN FLUIDIZED BEDS

by Nanhang Dong

Pyrolysis is considered as a promising technology of recovering bioenergy from biomass into gas, liquid and solid fuels. A series of works have been carried out previously on the fundamentals and the decomposition mechanism of pyrolysis empirically. Based on these experimental works, numerical approaches are employed to achieve a better understanding of the pyrolysis mechanism or aid the applications in experimental and industrial area.

In order to construct a systematic model of the thermochemical processes in biomass pyrolysis in a fluidized bed, the mass and heat transfer processes are investigated by two sub-subjects: modelling of the heat exchange between an immersed tube and a fluidized bed; modelling of mixing-segregation phenomena of binary mixture loaded in a fluidized bed as bed materials. Based on the finished studies, two reacting beds are represented by Eulerian approaches. The fast pyrolysis and catalytic pyrolysis of biomass is modelled by incorporating the corresponding kinetic schemes into the mass and heat transfer processes. The relevant models, coefficients and functions are tested and discussed for the

sensitivity and the simulation results show qualitative consistence with the existing experimental works.

The general model for thermochemical processes of biomass in the fluidised beds is built up in the present work successfully. The entire structure and methods can be introduced into other applications but not limited to biomass pyrolysis. The further optimization based on this model can be a useful tool on design of a large-scale pyrolyzor.

Keywords: biomass; heat transfer; mixing-segregation; fast pyrolysis; catalytic pyrolysis;

Contents

List of Tables

List of Figures

DECLARATION OF AUTHORSHIP

I, Nanhang Dong

declare that the thesis and the work presented in it are my own and has been generated by me as the result of my own original research.

"CFD MODELLING OF THE THERMAL DEGRADATION OF BIOMASS IN FLUIDISED BEDS"

I confirm that:

1. this work was done wholly or mainly while in candidature for a research degree at this University;
2. where any part of this thesis has previously been submitted for a degree or any other qualification at this University or any other institution, this has been clearly stated;
3. where I have consulted the published work of others, this is always clearly attributed;
4. where I have quoted from the work of others, the source is always given. With the exception of such quotations, this thesis is entirely my own work;
5. I have acknowledged all main sources of help;
6. where the thesis is based on work done by myself jointly with others, I have made clear exactly what was done by others and what I have contributed myself;
7. parts of this work have been published as given in the list of publications

Signed: ……..

Date:……

Acknowledgements

There are so many thanks I will express at the end of my PhD study.
First of all, I would like to send my sincerest thanks to my supervisors, Professor Kai H. Luo and Professor S. Gu, who have offered a great support on the project in the past four years. With their patience and help, I can progress step by step in the new subject in a new country. Say thanks to them again.

I would also like to express my thanks to my colleagues: Dr Lindsay, Dr Kostas, Dr Spyros, Dr Hani, Dr Nanda, Dr Arvind, Dr Costas, Dr Dinesh and Mr Moses. Coffee time in the kitchen is amazing to know each other more. I enjoy the time with you and miss you all in my whole life. Specially, thanks to my first and close friend in UK, Dr Jay who is not only a scholar but also a good chef.

I would also like to express my great gratitude to Professor C.J. Banks, Dr S. Heaven in Soton Uni., Professor R.H. Liu in SJTU, Dr P.M. Lv and Dr Z.L. Zhao in GIEC who offered a financial support on my exchange in China.

Finally, thank you, my dear wife Ida …

I gratefully acknowledge the financial support from the UK Engineering and Physical Sciences Research Council (EPSRC) grant EP/G034281/1 and EU FP7 ECOFUEL grant (project reference number: 246772).

Nomenclature

Dimensionless Numbers

Ar	Archimedes number	dimensionless
Nu	Nusselt number	dimensionless
Pr	Prandtl number	dimensionless
Re	Reynolds number	dimensionless

Greek and Roman symbols

g	Acceleration due to gravity	m/s^2
E	Activation energy	J/mol
φ	Angle	$degree$
Λ	Area	m^2
ρ	Density	kg/m^3
d	Diameter	m
κ_{Θ_s}	Diffusion coefficient	$kg/m\,s$
C_D	Drag coefficient	dimensionless
G	Elastic modulus	GP_a
F	Force	N
R	Gas constant	$J/Kmol$
Θ	Granular temperature	m^2/s^2
$\dot{h}$	Heat transfer coefficient	W/m^2K
H	Height	m
$\bar{\bar{I}}$	Identity matrix	dimensionless
$\vec{R}$	Interphase interaction force	N
K	Interphase momentum exchange coefficient	$kg/m^3\,s$
m	Mass	kg
$\dot{Y}$	Mass fraction of species	dimensionless

n	Number concentration	$1/m^3$
γ	Poisson ratio	/
A	Pre-exponential factor	$1/s$
p	Pressure	Pa
g_o	Radial distribution function	dimensionless
r	Radius	m
$\bar{\bar{D}}$	Rate of strain tensor	m/s
k_i	Reaction constant	$1/s$
e_{ss}	Restitution coefficient	dimensionless
ω	Rotational velocity	m/s
$\dot{S}$	Source term	/
ζ	Space time	s
Cp	Specific heat	$J/kg\,K$
ϕ	Sphericity	dimensionless
T	Temperature	K
λ	Thermal conductivity	$W/m\,K$
t	Time step	s
u	Translational velocity	m/s
$\bar{\bar{\tau}}$	Viscous stress tensor	Pa
μ	Viscosity	$kg/s\,m$
V	Volume	m^3
ε	Volume fraction	dimensionless
h	Volumetric heat transfer coefficient	W/m^3K

Subscripts

b	Bed
bio	Biomass
buo	Buoyancy
cel	Cellulose

cha	Char
col	Collision
dra	Drag
fee	Feeding
fix	Fixed bed
fri	Friction
g	Gas phase
gra	Gravity
hp	Heat penetration
hem	Hemicellulose
lig	Lignin
ini	initial
mf	Minimum fluidization
mb	Minimum bubbling
p	Particle
r	Radial
rea	Reactor
san	Sand
sli	Slip
s	Solid phase
si	Solid phase i
ssa	Specific surface area
sf	Superficial
syn	Syngas
tor	Torque

superscripts

eff	Effective
T	Transposed matrix

Chapter 1: Introduction

1.1 Biomass and Bioenergy Recovery

Due to the conflict between the rapidly increasing energy consumption and the limited storage of fossil resources, discovery and utilization of renewable energy have attracted a world-wide attention for decades. Biomass energy (bioenergy) can be one of the substitutes of the unsustainable resources for essential living/industrial activities. Bioenergy is recovered from solar energy stored in plants (*e.g.*, Straw, Sugar cane and Algae) in the form of chemical energy by photosynthesis. As the low emissions of SO_2, NO_x and $Soot$ [1], utilization of bioenergy can be an effective way to reduce air pollution. On the other hand, the carbon cycle is in a short period involving the processes of photosynthesis absorption during the plant growth and emissions from biomass consumptions such as combustion. The concept of "*Carbon-neutral"* is proposed for the zero net emission of CO_2 in the absorption and emission processes although it is still controversial among researchers at the expenses of transportation, storage, *etc*. Compared to solar and wind energy, the bioenergy is flexible in the form of either a direct heat/power source or solid, liquid and gaseous fuels.

Due to the low energy density of biomass (1.5 GJ/m^3, less than 10 % of bio-oil) [2], direct combustion of biomass for a heating system is regarded as a simple and inefficient method to utilize bioenergy. Several disadvantages should be noticed which hinder the biomass potential applications: *a*. low heat value; *b*. seasonal/periodic production; *c*. regional distribution; *d*. diverse species; *e*. transportation and storage expenses. To overcome the existing issues, numbers of techniques for the conversion of biomass to bioenergy were developed including digestion, gasification and pyrolysis of biomass, *etc*. The technologies related to either biochemical or thermochemical processes recover bioenergy into liquid/gaseous fuels or chemical feedstocks. Compared to combustion, both gasification and pyrolysis are promising methods to obtain higher heat value fuels in

the form of liquid or gas, which are also easily collected and transported. Technically, biomass gasification occurs at high temperature (typically more than 800 ℃) under a partial oxidation circumstance by air or an oxygen agent. The primary products, hot raw gasification gases, can be used for co-firing or indirect firing in heating-up processes. Meanwhile the high quality synthetic gases are supposed to be further synthesized into liquid fuels or chemicals (*e.g.*, methanol and ammonia) [3, 4]. The liquid fuel known as bio-oil is produced directly from the condensation of biomass pyrolysis vapours with the by-products, char and syngas. Compared to gasification, pyrolysis takes place at a relatively lower temperature in the absence of oxygen. In gasification, the technical optimization of minimizing tar yields is an issue standing in the way of the industrial-scale applications. On the contrary, the maximum yields of bio-oil are expected to improve the conversion rate of biomass to liquids in biomass pyrolysis.

1.2 Biomass Pyrolysis

The fractional yield distributions of end-products (char, tar and syngas) from biomass pyrolysis highly rely on the feedstock composition and the operational conditions. Due to the diverse species distribution, the suitable plants were specified and cultivated while the genetic engineering studies were involved to adjust the proportional components to increase the yields of products. Studies reveal that char is produced predominately at low temperature in a long residence time meanwhile the high temperature benefits the production of syngas [5]. At moderate temperature and a short residence time, the maximum yields of bio-oil up to 75 wt.% are achievable [6]. The pyrolysis processes are categorized according to the degrading temperature and the heating rate as shown in Table 1.1 [7]. Different particle sizes and residence time are specified for each process. Generally, biomass fast or flash pyrolysis aims to produce the primary product of bio-oil whilst biomass slow pyrolysis produces charcoal traditionally.

Table 1.1 Main operational parameters for pyrolysis processes

	Slow pyrolysis	Fast pyrolysis	Flash pyrolysis
Pyrolysis T (℃)	300-700	600-1000	800-1000
Heating rate (℃/s)	0.1-1	10-200	>1000
Particle size (mm)	5-50	<1	<0.2
Residence time (s)	300-550	0.5-10	<0.5

Fast pyrolysis is a thermal decomposition process at a moderate temperature in which the feedstock is heated to degrade in the absence of air into char, vapours (tar) and syngas such as *CO*, CO_2, methane, *etc*. Meanwhile the expected liquid product (bio-oil) is condensed in a condenser from the pyrolysis vapours. Several principles were concluded by Bridgwater [6] for maximum yields of bio-oil from biomass fast pyrolysis: *a*. specific degrading temperature around 500 ℃; *b*. rapid heating-up of cold biomass feed; *c*. a short residence time; *d*: steep condensation of the hot pyrolysis vapours. The removal of char is also a critical issue as char accelerates the vapours cracking between contact of vapours and char [8].

Bio-oil is a complex mixture of oxygenated hydrocarbons such as esters, ethers, aldehydes, ketones, phenols, carboxylic acids and alcohols [9]. The comparison of bio-oil and heavy fuel oil by Oasmaa *et al*. [10] is shown in Table 1.2. As the presence of aldehydes and ketones, bio-oil is hydrophilic with the moisture content up to 30 wt.%. Due to the low PH value, high oxygen rate and low energy density, bio-oil cannot be directly used as a substitute for traditional transportation fuels such as diesel oil and gasoline. The direct co-combustion of the bio-oil and diesel mixture as a transportation fuel meets great challenges such as the immiscible issues [11]. A proper emulsifier is necessary to dissolve bio-oil in diesel. This utilization also requires a new design of the engine to solve the issues of high levels of corrosion and abrasion.

Table 1.2 Typical properties of wood pyrolysis bio-oil and heavy fuel oil

Property	Bio-oil	Heavy fuel oil
Moisture content (wt.%)	15-30	0.1
PH	2.5	-
Specific gravity	1.2	0.94
Elemental composition (wt.%)		
C	54-58	85
H	5.5-7.0	11
O	35-40	1
N	0-0.2	0.3
Ash	0-0.2	0.1
HHV (MJ/kg)	16-19	40
Viscosity (cP)(50℃)	40-100	180
Solids	0.2-1	1
Distillation residue (wt.%)	Up to 50	1

Quality upgrading of bio-oil has been widely studied by reducing the oxygen rate and improving the hydrocarbon ratio [12-14]. Catalytic cracking of the pyrolysis vapours is one of the options to improve the bio-oil quality by detaching the oxygen content from bio-oil via catalyst. Producing petroleum-like fuels from bio-oil were carried out by using the ZSM-5 zeolite catalyst in catalytic pyrolysis [15]. In de-oxygenation of bio-oil by catalyst, the components of high molecular weight in the pyrolysis vapours degrade into the components of low molecular weight. Several technical issues need to be resolved step by step including selectivity, deactivation and regeneration of catalyst.

1.3 Fluidised Beds

Gas-solid fluidized beds have been widely used in various industrial sectors such as coal combustion/gasification, catalytic cracking of heavy oil, particle coating, particle drying

and blending, *etc*. The bubble's behaviour and particle translation in the gas-solid fluidised beds are extremely complicated and the relevant mechanism has been studied for decades. Compared to other types of contacting methods including fixed beds, circulating beds, rotating cone reactors, moving beds, *etc.* [6], the bubbling fluidized beds behave excellent on temperature control and mass & heat transfer. Rapid mixing and translation of solids lead to a uniform temperature distribution and the high heat transfer rate between gas and solids throughout the beds [16]. Considering the advantages above, the fluidized bed reactors are widely employed for producing bio-oil from the biomass fast pyrolysis in lab- or pilot- scale. Figures 1.1 and 1.2 show the fluidized bed reactors in lab-scale in Guanzhou Institute of Energy Conversion (GIEC, China) and Shanghai Jiao Tong University (SJTU, China) respectively. Figure 1.3 shows a pilot-scale reactor in Shaanxi Province (China).

Figure 1.1 A fluidized bed reactor in lab-scale at GIEC.

Figure 1.2 A fluidized bed reactor in lab-scale at SJTU.

Figure 1.3 A downer reactor in pilot-scale.

1.4 Pyrolysis Modelling

Kinetic scheme development is necessary to describe the mass transfer among species or the pathways of chemical reactions during pyrolysis progresses. Although the reacting mechanism of fast pyrolysis is too complex to introduce in a detailed way in current stage, global or semi-global schemes describing the mass depletion of biomass and the formation of intermediate- and end- products were summarized and introduced [17]. In the multi-component scheme, biomass fast pyrolysis is described by degrading of three pseudo-components: cellulose, hemicellulose and lignin, individually [18]. However a uniform composition is defined for biomass in single-component schemes and furthermore the one-step schemes which give the end-products from biomass in one step [19] are developed to the multi-step schemes by considering the intermediates and secondary cracking of pyrolysis vapours [20-23]. With the studies in-depth, the optimized schemes are prospective to represent the detailed biomass pyrolysis processes in future.

Based on the knowledge such as mass and heat transfer in fluidized beds and kinetics of biomass thermal decomposition, a numerical model to describe the biomass fast pyrolysis processes in a fluidized bed is supposed to be available by incorporating all the existing progresses. However, it is not a task to simply assemble the different sections. Several commercial or open source software including ANSYS FLUENT, MFix, OpenFoam and MultiFlow are available for modelling of mass and heat transfer in multiphase flow. By coupling the kinetics into the modelling works, the entire processes of biomass pyrolysis in a fluidized bed reactor can be represented. The quantitative results are expected by building up the model with suitable mathematical equations or empirical correlations/functions. Generally, the setup of numerical models is significant to resolve the issues such as spatial/ temporal limitation, unavailable measurements for invisible or extremely small scale phenomena and optimization of geometry and operational parameters in pilot-/industrial-scale.

1.5 Thesis Objective

The objective of the current project is to construct a numerical model to represent the physicochemical processes of biomass fast/catalytic pyrolysis in a fluidised bed reactor. The progress of this project is based on the studies of multiphase hydrodynamics, conductive and convective heat transfer, reaction scheme development, numerical approaches optimization, *etc*. Simulations of the fast pyrolysis and catalytic pyrolysis via Eulerian approaches are planned by incorporating the kinetic schemes into the mass and heat transfer in a fluidized bed reactor. To achieve this purpose, the work was commenced by investigating the heat exchange and the hydrodynamics of multiphase flow in unreactive fluidized beds via the computational fluid dynamics (CFD) software, ANSYS FLUENT. Then the kinetic schemes describing the fast pyrolysis or catalytic pyrolysis were programmed by *C* language and coupled into a multiphase flow model by user define function (UDF).

Temperature is one of the dominate factors that affect the yield distribution of pyrolysis end-products. A modelling work of heating up of a fluidized bed by an immersed tube was carried out. The heat transfer coefficient between the hot tube and the cold fluidized bed were predicted with the modified thermal conductivities of gas and solids. Meanwhile the effects of different tube shapes were addressed by investigating the flow pattern of the bed and the heating up efficiency of the hot tube.

Particle translation and bubble behaviour are significant phenomena in gas-solid bubbling fluidization. The flow pattern is very complicated in binary bed mixtures due to the mixing and segregation of particles of different sizes and/or densities. To qualify the feasibility of Eulerian approaches, the mixing-segregation phenomena were represented by modelling of fluidized beds loaded with solids in size/density difference.

Due to the limitation of Eulerian approaches in particle scale, the influence of intra-particle heat conduction on the chemical reaction progress cannot be studied directly. A correlation describing the heat conduction effect was employed to modify the biomass degrading rate in the modelling of biomass fast pyrolysis. The implementation of the empirical correlations is a brave attempt on improving the accuracy of the modelling of fast pyrolysis of large biomass particles via Eulerian approaches.

Modelling of catalytic pyrolysis is carried out based on the reported experimental work. A kinetic scheme proposed for catalytic pyrolysis was employed to obtain the fractional yield distribution of end-products. The qualitative consistency between the simulations and the experimental results delivers that the numerical model constructed is suitable to describe the chemical reactions in a bubbling fluidized bed reactor. The extended application of the model can be carried out by applying different kinetics for biomass fast/catalytic pyrolysis.

1.6 Thesis Novelty

Compared to the extensive works on fast pyrolysis and catalytic pyrolysis in experiments, the numerical applications in the subjects are limited. As mentioned above, the modelling of biomass pyrolysis in a fluidized bed is a systematic project by combining all of the knowledge in different sub-projects. Hence the empirical and numerical development in studies of multiphase flow, heat transfer, kinetic scheme of chemical reactions and numerical approaches dominate the model setup. The novelty of the present work is constructing a general numerical model to represent the fast pyrolysis and catalytic pyrolysis by Eulerian approaches via commercial software ANSYS FLUENT. The main contributions of the project are demonstrated as following aspects: generally, the self-developed *C*-subroutines for the kinetic schemes of fast pyrolysis or catalytic pyrolysis have been successfully introduced into the simulations. Based on the constructed model, the flow patterns of fluidized beds are represented while the sensitivity of the parameters, functions and coefficients in use is discussed. In the details

of sub-projects: *a*. the prediction of heat transfer coefficient is improved by using the effective thermal conductivities into the heat exchange between a tube and the fluidized bed; *b*. the mixing and segregation of binary mixtures belonging to Geldart groups B and B/D [24] are studied systematically by Eulerian approaches; *c*. the intra-particle heat conduction is considered by incorporating a *C*-subroutine into the modelling for fast pyrolysis of large biomass particles by Eulerian approaches; *d*. the catalytic pyrolysis processes are numerically represented and validated with the experimental data. By considering the convenient handling of the commercial software and the flexibility of the numerical model, the similar work is possible to be carried out in pilot- or industrial-scale.

1.7 Thesis Structure

This thesis is composed of 8 chapters:

Chapter 1 introduces the general information about biomass, bioenergy and recovery techniques such as gasification and pyrolysis. The advantages and disadvantages in recovery and application of bioenergy from biomass are discussed while the principles to obtain the maximum yields of bio-oil are demonstrated. A brief introduction of objective of this thesis is given together with novelties of the current work.

Chapter 2 carries out the detailed literature review of numerical applications on all sub-subjects such as multiphase flow, heat transfer, kinetic scheme development, *etc*. Based on the extensive works, the suitable approaches can be summarized and employed to set up the numerical model for the current project.

Chapter 3 gives the fundamentals of multiphase flow. The reaction mechanisms are represented by the kinetic schemes. The relevant governing and constitutive equations are listed together with the mass transfer routes during biomass pyrolysis. Several assumptions in the current work are pointed out in this chapter.

Chapter 4 studies the heating up of the fluidized bed by a hot tube numerically. Although the heat exchange in a fluidized bed has been widely studied, the heat transfer coefficient between the immersed surface and the bed is still over-predicted. By summarizing the existing works, the correlations termed as effective thermal conductivities are employed to improve the prediction of the heat transfer coefficient.

Chapter 5 represents the mixing-segregation phenomena in a gas-solid fluidized bed loaded with binary bed materials. The mixing index is calculated for different solid mixtures and operational conditions. The simulation results are validated with experimental works while the segregation phenomena of particles with different densities are represented qualitatively.

Chapter 6 shows the simulation of biomass fast pyrolysis. An empirical correlation is employed to represent the influence of the intra-particle heat conduction on reaction progresses. Thermal decomposition of large particles is investigated.

Chapter 7 introduces the modelling of biomass catalytic pyrolysis in bubbling fluidized beds. The upgrading of bio-oil by in-*situ* catalytic pyrolysis in a fluidized bed reactor is considered and the simulation results are validated by the experimental data.

Chapter 8 summarizes the progresses and the contributions of this thesis. The expected optimization of current model is demonstrated for future study.

Chapter 2: Literature review

2.1 Introduction

Fast pyrolysis of biomass has been a promising technique to transform biomass into liquids, namely bio-oil, with by products (char and syngas). From a chemical point of view, biomass is a composite material with different proportions of three pseudo-components (hemicellulose, cellulose, lignin) and extractives [17]. Different thermal stabilities of the three pseudo-components are present in degradation due to different degrading temperature ranges. Application of the thermogravimetric analysis (TGA) is one of the effective techniques to introduce the thermal degradation characteristics of biomass [25]. By comparing the thermogravimetric (TG) and derivative thermogravimetric (DTG) curves, the results indicate that fruit/vegetable-biomass consists of more hemi-cellulose but less cellulose than wood-biomass [26]. Based on the analysis of thermal degrading mechanisms, chemical kinetics studies are progressed by describing biomass thermal decomposition with the one-component mechanism (single-component model) or independent parallel degradation of the three pseudo-components (multi-component model) [19, 20, 27]. In one-component mechanism, a uniform composition is defined for biomass to decompose into end-products. A series of studies has been carried out to investigate the thermal degrading mechanism of biomass [28, 29]. The relevant results show that the fractional yield distribution of the end products relies on the reaction conditions and operational parameters tightly.

According to the principles proposed by Bridgwater [6], the maximum yields of liquids can be achieved in fast pyrolysis of biomass under certain conditions such as temperature, residence time, *etc*. Hence the implementation of the numerical methods is supposed to be an economic way to understand the physicochemical processes and to optimize the system design and operational parameters. Furthermore, the reactors are supposed to be one of the significant sections of biomass fast pyrolysis system. The gas-solid fluidized

beds are widely used for combustion, gasification and pyrolysis due to several advantages illustrated in Chapter 1. The complicated physicochemical processes always take place under specific temperature or/and pressure in the beds, where the mass and heat transfer will give a direct influence on the final product yields. Numerical models are applied to represent the hydrodynamics of multiphase flow in a fluidized bed which is not visually accessible in experiments.

2.2 DPM and TFM

In numerical models, the solid and gas phases are generally treated by two classic approaches, namely Eulerian approach and Lagrangian approach. By the former approach, the solid phases are considered as interpenetrating continua with individual volume fractions however the trajectories and the intra-particle phenomena of individual particles can only be investigated by the latter one. The direct integration of the two approaches derives four types of model to describe the fluidization of gas-solid flow: Eulerian-Eulerian (E-E) model, Eulerian-Lagrangian (E-L) model, Lagrangian-Lagrangian (L-L) model and Lagrangian-Eulerian (L-E) model.

The L-L model is employed to study the particle behaviour in extremely small scale and collisions of the gas particles with the solid particles are represented. It is very fundamental to express the effects of Brownian motion on the gas-solid interactions [30]. The discrete bubble model (DBM), a L-E type of model, is developed to describe the bubble's motion, where the bubbles are treated as discrete entities and the gas-particles emulsion phase as a continuum [31]. Both the two models are rarely used for the high requirement on computational capacity. As reported in literature [32-43], the E-L model and E-E model are applied widely in modelling of multiphase flow.

a. Interaction between gas and a particle

b. Interactions between particles

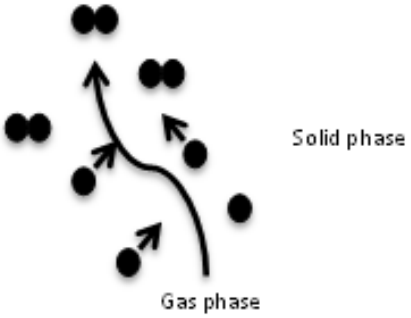

c. interactions between gas/particle and particle

Figure 2.1 Flow pattern of DPM/DEM.

Discrete particle model (DPM) or discrete/distinct element method (DEM) is widely used for applications involving particles. DEM was first introduced by Cundall and Stack [44] which was employed later into the modelling of gas-fluidized bed with the soft-sphere model by Tsuji *et al*. [45] and with the hard-sphere model by Hoomans *et al*. [46], respectively. Hence, several properties can be obtained simultaneously such as gas and solid velocities, bed voidage, particle trajectories, *etc.* These E-L type of models were referred as DPMs (DEMs) by Deen *et al*. [47] in modelling of gas-solid fluidization

whilst DEM was specified for the soft-sphere model by Luding [48]. In DPM/DEM, the gas-solid fluidization is related to gas-particle and particle-particle interactions as shown in Figure 2.1(c). The gas-particle interaction is considered by the drag force exerting on the individual particles given in Figure 2.1(a) whilst the particle-particle interactions by collision forces in Figure 2.1(b). The drag force can be calculated by empirical correlations and the collision behaviour can be described by hard-sphere or soft-sphere models.

In hard-sphere model, particles are assumed as quasi rigid objects for instantaneous collisions which mean no deformation occurs in particle-particle contacts. Particle motions are determined by the momentum conservation in binary collisions. Luding *et al*. [49] reported that the hard sphere model is valid for a dilute system which is dominated by binary collisions. The particle motion in a bubbling fluidized bed was investigated with this model and the simulation results are consistent with the predictions with kinetic theory of granular flow for elastic particle fluidization [50]. The mixing and segregation of binary mixtures [51] and particle residence time [52] in fluidized beds were also studied by the hard-sphere model.

Due to the simpler treatment of collisions with binary contacts, the hard-sphere model is relatively faster than the soft-sphere model in which the multi-particles collisions are taken into account and particles are allowed to overlap slightly [47]. To resolve the overlap, a fixed time step smaller than the duration of a contact is used to ensure the energy conservation, which requires a heavy CPU load for soft-sphere model. Based on DPM with soft-sphere model, solids circulation patterns and average bubble size in a fluidized bed with flat membranes were investigated [53]. A qualitative agreement was achieved between simulation and experimental results on the inversion of the solids circulation and reduced bubble size during gas addition. However the significant discrepancy exists on solids motion and bubble size distribution. Wood gasification [54]

and coal combustion [55] in a bubbling fluidized bed were modelled by the soft-sphere model, respectively.

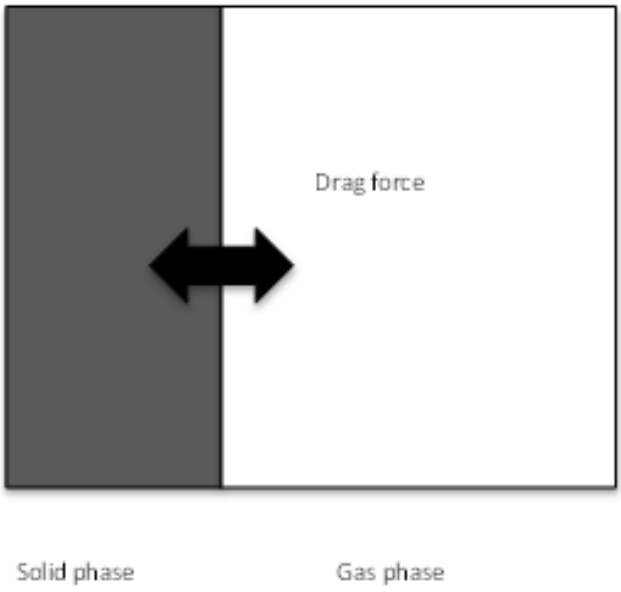

Figure 2.2 Interaction of TFM.

In E-E model, also called two-fluid model (TFM), both gas and solids are described as interpenetrating continua with individual volume fractions and the interphase interaction is addressed by drag force shown in Figure 2.2. In TFM, the effect of particle-particle collisions within solid phase is indirectly described by solid pressure, solid shear viscosity and solid bulk viscosity. In the early stage, an empirical constant was given for viscosities (CVM) and the solid pressure was determined depending on the solid volume fraction experimentally [56]. This model is simple but it could not represent the underlying characteristics of solid phase rheology [30]. Based on an analogy of kinetic theory of gases [57], the kinetic theory of granular flow (KTGF) was developed where the solid pressure and solid viscosity were determined in terms of solid volume fraction, coefficient of restitution and the granular temperature [58-60]. The fluctuating energy dissipation during particle collisions was calculated by the coefficient of restitution

meanwhile the granular temperature was associated with the particle random fluctuation velocity.

The exchange coefficient is used to calculate the drag force exerted on solid particles by gas in gas-solid fluidized beds. Based on the exchange coefficient, the interactions between gas and solid phases are represented and the local voidage in gas-solid flow can be predicted. Interphase interaction in TFM is considered by the drag model. Ergun [61] investigated the interphase momentum exchange in a fixed bed and an Ergun equation was derived for the drag coefficient. For a bubbling fluidized bed, the solid particles are presumed to well disperse in the dense region among bubbles (dilute region). The Gidaspow model [60] describing the gas-solid interphase interactions in both dense and dilute regions has been widely accepted by combining the drag coefficient for dilute region developed by Wen and Yu [62] and Ergun equation for dense region. In these models, the drag force is set up associated with Reynolds number and solid volume fraction. However the physical properties such as particle shape and roughness were not taken into account. The detailed governing and constitutive equations for gas and solid phases by TFM are given in Chapter 3. Several existing drag models including Syamlal-O'Brien [63], Gidaspow [60], and Arastoopour [64] models were reviewed for the implementation into the modelling of FCC particles fluidization. The modified Syamlal-O'Brien model was proposed and supposed to deliver the good prediction in turbulent fluidization of FCC particles [65]. Different TFMs were also available in literature and compared by Boemer *et al*. [66]. Further works need to be done to improve the model for more realistic representation.

Table 2.1 Numerical models available for gas-solid fluid beds

Name	Gas phase	Solid phase	Scale	collisions	Interactions
DPM	Eulerian	Lagrangian	Particles	Soft-sphere model	Gas-particle drag closure
	Eulerian	Lagrangian	Particles	hard-sphere model	Gas-particle drag closure
TFM	Eulerian	Eulerian	Continuous flow	KTGF	Gas-solid drag closure

Due to the simplification of disperse particles to a continuum, it is not computationally expensive as DPM which accounts the motion of each particle in a fluidized bed. Both DPM & hard-sphere model and TFM were employed by Chiesa et al. [67] to study the particulate flow in a fluidized bed. By comparison with the experimental data, DPM & hard-sphere model performs a better consistency than TFM however the corresponding CPU time is four orders of magnitude higher than that for TFM. De Jone *et al*. [53] pointed out that the qualitative agreement can be expected between experiments and modelling with TFM or DPM & soft-sphere model however the quantitative prediction is difficult to deliver. A brief summary of DPM and TFM is given in Table 2.1.

2.3 Heat Transfer in Fluidized beds

Heat transfer including gas-solid heat convection, solid-solid heat conduction and wall/surface-bed heat exchange in gas-solid fluidized beds needs a clear understanding as the thermochemical reactions are primarily dominated by temperature. The issue is the measurement of heat transfer rate is difficult therefore the heat transfer coefficient is generally derived by comparing the temperature distribution in bed between experimental measurements and theoretical calculation.

The heat transfer mechanism was studied between an immersed surface (a stationary wall or a fixed tube) and the gas-fluidized bed by Boterill [68] and Yates [69]. Their experiments showed that the maximum heat transfer coefficient achieved through a sharp increase after the transition from a fixed bed to a fluidized bed occurs. A gradual decline can be observed with the further increase of the fluidizing gas flow rate. The refreshment of fluidized particle packets driven by bubbles near the immersed surface is considered to contribute to the changes of heat transfer coefficient in particle fluidization. Parmar *et al.* [70] measured the heat exchange rate between a freely moving sphere and the bubbling fluidized bed. The decreasing tendency in the stage of high fluidizing intensity was proven but the maximum

heat transfer coefficient was not observed. Meanwhile the heat transfer coefficient was supposed to depend on the bed temperature and the particle size. The absence of sharp increase of heat transfer coefficient was also supported by Collier *et al*. [71]. However the constant heat transfer coefficient was delivered for a fluidised bed as they considered a negligible heat transfer from the immersed sphere to the particulate phase. A semi-empirical single particle model [72] was developed to describe the heat transfer coefficient between an immersed surface and the fluidized bed in which the particle Archimedes number (ratio of gravitational force to viscous force) is higher than 200. The expression of surface voidage near the immersed surface was first proposed, which is supposed to describe the effect of pressure, temperature, particle size, *etc*. The surface voidage was accounted in the single particle model to analyse the relation between hydrodynamics and heat transfer rates. Meanwhile Di Natale *et al*. [72] also claimed that the proposed model cannot reflect the effect of surface shape on heat transfer coefficient. In another work [73], they presented a range of heat transfer coefficients from experiments using different shaped immersed surfaces within a fluidized bed. The findings highlighted the strong influence of surface shape on heat transfer coefficient rather than just thermal properties alone. According to the experimental data, the variation of heat transfer coefficient by different surface shapes was up to 40%. Correspondingly, a shape factor (ratio of vertical probe dimension to probe characteristic dimension) was given into the correlation for prediction of heat transfer coefficient [73]. Mickley and Fairbanks [74] suggested that the particle-wall contact time was an important factor for calculating the heat transfer coefficient between the wall and fluidized beds. Packets of particles contacting with the wall frequently could enhance the heat exchange. All the works are reasonable and verified experimentally however the relevant correlations cannot be applied into the heat transfer modelling by TFM.

Kuipers *et al*. [75] numerically studied the wall-to-bed heat exchange by TFM to determine the influence of bubble motion on the heat transfer. The effective thermal bed conductivity was used by considering the thermal conductivities of fluid and solid phases

together with the bed voidage. The effect of bubble motion on the heat transfer coefficient was determined and the bubble-induced particles refreshment near the wall delivered relatively large wall-to-bed heat transfer coefficients. Tube-to-bed heat transfer was considered by Schmidt *et al*. [76] in modelling of a symmetrical bed with TFM. The results provided a good representation of the bubbling dynamics around the tube however Armstrong *et al.* [77] showed that a symmetrical bed does not represent the heterogeneous behaviour of the particles. Furthermore they found that increasing the number of tubes leads to the breakup of bubbles causing a more heterogeneous bed, which increases particle motion and provides better heat transfer. Patil *et al.* [78] considered a range of different operating conditions and two different closure models, the constant viscosity model (CVM) and the kinetic theory of granular flow (KTGF) model. They found that the KTGF model captured better transitions of the bubbles compared to the CVM model. Unfortunately the heat transfer coefficient was over-predicted compared to the experimental results, particularly when an effective solid thermal conductivity included the influence of particle kinetic conductivity. Armstrong *et al.* [79] extended the simulations over a longer period of time and found that the heat transfer coefficient decreased as the bed dynamics eventually formed a regular dynamic pattern. It was more realistic because experiments were performed over long durations compared to the several seconds that simulations were run for in previous modelling. Yusaf *et al*. [80] considered the effects of the effective solid thermal conductivity and highlighted a model which reduced the heat transfer coefficient considerably compared to previous attempts.

Littman *et al.* [81] reported the measurements of heat transfer to a particle in a fixed bed with low particle Reynolds number which is less than 100. Based on the similar works [82, 83], an Nusselt number correlation which is the ratio of convective to conductive heat transfer across the boundary of a flow, was derived by Gunn [84]. The general form of the expression is a function of the Reynolds number and the Prandtl number (ratio of momentum diffusivity to thermal diffusivity), which can be used to describe the interphase

heat transfer in the fixed and fluidized beds within the viodage (porosity) range of 0.35-1. The detailed expression is given by Equation 3.42 in Chapter 3. This expression can be applied into TFM directly.

DEM is also widely employed to study the heat transfer in a gas-fluidized bed. The contributions of convection, conduction and radiation were quantified for a deep knowledge in controlling the heat transfer in fluidized beds [85, 86]. Heat conduction was investigated due to the particle contacts in a binary mixture loaded in the fluidized bed. The contribution of particle collisional heat conduction was estimated around 10 % of the gas-solid heat convection. Three models were proposed to study the heat transfer between an immersed probe and a fluidized bed by DEM [87]. The simulation results indicated that the heat transfer coefficient can be well predicted by introducing a gas film or gas gap between particles and immersed surface (model 2) which was proposed by Botterill and Williams [88]. Meanwhile the underestimation of heat transfer coefficient was delivered if only the direct body contacts dominated the heat transfer (model 1). Although model 3 was more realistic by considering heat exchange between surrounding gas and surface together with that between direct contacts of solids and surface, the application of model 3 deviated considerably from the experimental data.

By summarizing the existing work, a series of studies has been addressed on understanding the fundamental mechanisms or describing the heat transfer in fluidized beds. For temperature dominated reactions in the fluidized beds, a realistic temperature distribution is important to represent the physicochemical processes. Hence the accurate prediction of heat transfer coefficient from an immersed surface to the bed is significant. However in the current stage, the over-prediction of the heat transfer coefficient by previous models is identified and reported. Improving the prediction of heat transfer coefficient is necessary meanwhile the effects of immersed surface shapes on

hydrodynamics of multiphase flow and heat transfer coefficient need to be studied numerically.

2.4 Hydrodynamics of Fluidized Beds

2.4.1 Modelling of Gas-solid Fluidization

DMP and TFM are widely used in representing the gas-solid fluidization. DPM gives more details such as particle trajectories, particle collisions and interactions between gas and a single particle. Based on DPM, a 3-D numerical model was set up based on a spouted bed with a draft tube in lab scale [89]. The total amount of particles in use was 22000 with the diameter of 3mm. The specific contribution of the model was considering the erosion behaviour for different tube configurations. The corresponding conclusions were delivered via the simulations but the results were not validated by experiments. The simulation of an internally circulating fluidized bed with a batch of approximately 0.1 million particles with the diameter of 1.2 mm, was set up to address the effects on flow behaviour with different gas and solid properties [90]. Especially, the influences of shape, size distribution, solid Young's modulus *etc.* have been identified which cannot be easily applied by TFMs. The interactions between gas and particles in DEM have been investigated by employing three interphase drag correlations to show the variety in simulation of bubbling fluidized beds [91]. The sufficient information of solids in fluid can be obtained from the application of DPM. However the high requirement of computational capacity limits the applications in pilot-/ industrial- scale simulations with a huge amount of particles involved.

For gas-solid two-phase flow, TFM is well accepted due to its relatively low computational intensity. To obtain reliable results from simulations, the investigation of the wall boundary conditions was reported. Three types of wall boundary conditions (BCs) including no-slip (1 for specularity coefficient), free-slip (0 for specularity coefficient) and partial-slip (0 < specularity coefficient < 1) BCs were evaluated in modelling of a

dilute multiphase flow [92]. The small specularity coefficient for partial-slip BC or free-slip BC was reported to deliver the results close to experimental data. The investigation of BCs were also carried out in modelling of back mixing of gas in a gas-fluidized bed [93]. The effects on gas back mixing are enhanced when the specularity coefficient is smaller than 0.05. The performances of partial-slip BCs were compared between the 2-D and 3-D simulations of a bubbling fluidized bed [94]. The best agreement with the experimental data was given by the specularity coefficient of 0.005. Lan *et al*. [95] worked on the effects of wall BCs in a spouted bed. The simulation results were validated by experiments and the specularity coefficient was recommended modestly for a value of 0.05 to give a good prediction in modelling of a spouted bed meanwhile the solid-wall restitution coefficient was supposed to play a minor role. Chen *et al*. [96] presented a detailed work on the influence of parameters such as grid size, BCs together with the turbulent models. However the results were validated by calculation values of classical equations instead of experimental data. The no-slip BCs were defined for both gas and solid phases in the modelling of a self-heating biomass fast pyrolysis reactor [97]. All of the studies pointed out that the BCs impose significant effects on the flow behaviour of gas-solid flow in the reactors. However no universal setting or definition for wall BC was concluded to achieve the accurate results from simulations perfectly. For instance, the free-slip BC was preferred by Chen *et al*. [96]. However it is not realistic because there is no perfectly smooth surface for free slipping. Meanwhile in studies of Lan *et al*. [95], the suggested value for a partial-slip BC can only be used in confidence in specific cases. Consequently, it is difficult to tell which settings/definitions are the most appropriate for simulations in different cases.

The jet penetration behaviour was studied in modelling of a gas-solid fluidized system [98, 99]. The comparison of simulation results with experimental photos indicated that the relevant flow pattern could be represented successfully via TFM coupling with KTGF. In confidence of implementing TFM, the erosion rates of immersed tubes in a bubbling

fluidized bed were calculated [100]. TFM was employed to study the hydrodynamics of gas-solids fluidization at different superficial velocities, different reactor geometries and different gas pressures [35, 101]. The simulation results showed a good agreement with the reported data in literature and they expressed a modesty confidence of TFMs on large scale simulations. Bubble's shape and motions were investigated via TFM while the hydrodynamics was represented by considering of the wall effects [102]. The bubble formation was observed near the wall corners.

The flow pattern of fluidized beds with cohesive particles is complex due to the appearance of agglomerates/clusters. To investigate the motion of agglomerates, the agglomerates-based approach (ABA) was developed and coupled into TFMs [103]. In the ABA, the equivalent agglomerate size was introduced to replace the size of solid particles and the motion of solid particles was delegated to agglomerates behaviour. However, the equivalent agglomerate size derived from force balance was difficult to be defined by appropriate correlations. A cluster-structure-dependent (CSD) drag coefficient model was proposed by Wang *et al.* [104-106] to express the interactions while the clusters were moving in a riser. Correspondingly, the equivalent diameter of the cluster was introduced where the equivalent diameter/size of cluster/agglomerate derived from energy balance instead of force balance in ABA. Furthermore, a term considering the effect of wall friction on gas/solid flow was applied to optimize the CSD drag coefficient [104, 105]. Similar approaches were introduced and named as EMMS (energy-minimization multi-scale)-based multi-fluid model by Hong *et al*. [107] and Wang *et al*.[108]. All the numerical works showed agreement with experimental results, especially on representing the meso-scale heterogeneous structure in circulating fluidized beds. Meanwhile a modified drag coefficient model based on the EMMS model, namely bubble-based EMMS model, was validated in simulation of bubbling fluidized beds by bubbles in place of clusters [109]. Another approach considering the effects of cluster was mentioned by

introducing a scaling factor directly to the universal drag laws [110], which was expected to predict a realistic solid/gas distribution in a turbulent fluidized bed.

The population balance model (PBM) was developed to calculate the particle size distribution (PSD) where the evolution of particles can be described by particle growth, shrinkage, aggregation and breakage. A model for two-phase flow was reported by coupling the PBM into TFM [111-113]. The results obtained from simulations were validated to be effective on inspecting the PSD evolution. Meanwhile the temperature field was predicted based on the model to analyse the effects of operational parameters [114]. By considering mass and heat transfer inside a single particle, a polymeric multiplayer model (PMLM) is incorporated into the PBM-based E-E model to capture the dynamic evolution of PSD in a gas-solid fluidized bed polymerization reactor [115]. Combining the TFM, PBM and PMLM, the polydisperse system is supposed to be investigated in detail, from mass and heat transfer inside the particle to flow pattern inside reactors. By incorporating different models into TFM, the hydrodynamics of different fluidizing regimes including bubbling fluidised beds, turbulent fluidised beds and fast fluidizing beds can be well represented as reported above.

3-dimentional (3-D) simulations of gas-solid fluidized beds were supposed to deliver more realistic result than that from the 2-D models. Peirano *et al*. [116] studied the difference between 2-D and 3-D simulations of a rectangular bubbling fluidized bed. They concluded that the height expansion and pressure spectra can only be predicted accurately in 3-D models due to the natural three-dimensionality of the flow. Compared the profiles of voidage, gas and solid velocities in 2-D and 3-D simulations, significant differences were reported by Li *et al*. [93] and only the qualitative sensitivity analysis via 2-D was approved in their conclusions. In contrast, Xie *et al*. [117] indicated that the 3-D bubbling fluidized bed can be successfully represented with a 2-D model due to the satisfactory qualitative agreement between simulations. The residence time of a particle in

a bubbling fluidized bed was studied in 2-D and 3-D simulations by Papadikis *et al.* [118]. The slightly difference of flow pattern of the fluidized beds was observed however the bed expansion is similar in both cases. The considerable differences were derived based on analysing the particle residence time in the fluidized bed reactor. In 3-D simulations, the particle motion is much more complicated because the asymmetrical flow pattern appears compared to 2-D simulations. Most of the works pronounced that 3-D simulations were preferred to perform the results close to the experimental data. However all of them agreed that the full dimensional models are computationally expensive and time-consuming whilst 2-D simulations are intelligible and acceptable due to the computational power limitation. For instance, the comparison was carried out by Papadikis *et al*. [118] based on the data from simulations running for 3 s. Xie *et al*. [117] summarized the computational time required for 3-D which is several times to one order of magnitude higher than that for 2-D simulations. In 3-D simulations of Li *et al*. [93], the computational time of 8 hours is needed for the 1 second of real-time simulation. In the current study, it is computationally expensive even in 2-D because the heterogeneous and homogeneous chemical reactions are incorporated into the modelling of mass & heat transfer in fluidized beds. The 2-D model is supposed to be applicable for a qualitative discussion.

2.4.2 Modelling of Binary Mixture Fluidization

The mixing-segregation behaviour changes the concentration distribution of solid mixtures in fluidized beds and affects the thermochemical processes directly. Recently fluidized bed reactors have been used for biomass catalytic pyrolysis. The mixture of catalyst and inert particles such as sand are loaded as the bed materials to upgrade the pyrolysis vapours simultaneously by catalytic cracking. It is found that the product fractional distributions are associated with the catalyst percentage in bed materials [119], therefore catalyst concentration distribution in the bed needs to be controlled carefully to achieve the desirable outputs. A gas-fluidized bed with binary solid mixtures is more complicated than that with identical particles. Experimental work reported by Rasul *et al.*

[120] showed the segregation phenomena with layer inversion in fluidization of solids at different sizes, which is more evident with liquid-fluidization than gas-fluidization. Meanwhile the layer inversion for solids at different densities was observed experimentally and was also represented in modelling with DEM [121]. Yusif *et al*. [122] pronounced that the complete mixing of binary mixtures with the ratio of low to high terminal velocities over 0.7 occurs if the ratio of superficial velocity to the mixture minimum fluidization velocity is greater than 5. The minimum fluidization velocities of biomass and sand mixtures were determined experimentally by Oliveira *et al*. [123]. An expression was derived from the experimental data for prediction of the minimum fluidization velocities of binary mixtures. Wu and Baeyens [124] investigated the influences of parameters including solid size ratio, bed aspect ratio, and superficial velocity on final mixing and segregation balance empirically. An expression in terms of particle size ratio and the visible bubble flow rate was given for calculation of mixing index. Based on the experimental data, Lu *et al.* [125, 126] studied the fluidization behaviour of binary mixtures, experimentally and numerically (particle sizes >1.5 mm). TFM was applied to represent the mixing and segregation phenomena while the interphase interaction was considered by a modified Gidaspow model for gas-solid exchange coefficient. They concluded that the given value of restitution coefficient affects the concentration distribution of solid classes from modelling prediction. Seven drag force correlations for interaction between solid phases (sizes >1.5 mm) were compared in CFD modelling of mixing-segregation of binary mixtures [127]. The simulation results showed the similar tendency of segregation progress which leads to an over-prediction of segregation rate. Hence a frictional binary particle drag was introduced into the existing correlations to avoid the underestimation of binary particle drag and the semi-empirical correlations behaved well on predicting bed height and segregation rate. The mixing details such as particle exchange and circulation were captured by Cooper and Coronella [128] with a three-fluid model. Their studies revealed modest but discernible local segregation due to the relative motion of particles when bubbles pass by.

Feng *et al.* [129, 130] employed DEM to study the mixing-segregation in terms of flow patterns, solid concentration and mixing kinetics. It was found that the degree of mixing was highly dependent on the superficial velocity while the final steady state was not decided by the initial packing condition. The effective drag force with a voidage function was investigated and the effective drag coefficient as a function of Re_p was recommended for prediction of mixing degree of binary mixtures [131].

Extensive studies of mixing and segregation of binary materials with small particles such as fluid catalytic cracking (FCC) particles [132-135] or large size solids (larger than 1 mm) [136, 137] were also carried out experimentally and numerically. However the flow pattern of binary mixtures of particles of moderate size was seldom reported by TFM. The detailed investigation needs to be carried out systematically on the mixing segregation balance and it will be helpful on studies of biomass mixing with bed materials, char removal in biomass fast pyrolysis system and catalyst distribution in a biomass catalytic pyrolysis reactor.

2.5 Kinetic Scheme Types

For a reacting fluidized bed, the end-product distribution can be delivered by coupling chemical reactions into the numerical representation of flow pattern and temperature field. The classical method describing the chemical reaction mechanisms is by using the molecular reaction scheme (chemical equation) to display the element transforming routes. Following the knowledge on reaction mechanism of species with corresponding chemical formulae, the detailed chemical equations were given to describe the reactions such as the polymerization of several species or decomposition of a single compound. A kinetic model including 148 species and 557 reactions was developed to deduce the details of cyclohexane pyrolysis [138, 139]. Simulation results indicated that the constructed model successfully predicted most of the pyrolysis products that were collected in experiments and the reacting pathways were also identified clearly. The pyrolysis of tetralin in the temperature range of 850-1500 K was described by a kinetic model with 149 species and

554 reactions. The product distribution predicted from the simulation was in good agreement with the experimental data. It was an indirect proof that the proposed kinetic model can introduce the pathways for tetralin decomposition effectively [140]. In the study of tert-butanol combustion, the pyrolysis of tert-butanol in the temperature range of 950-1850 K was constructed by over 20 pyrolysis species [141] and the kinetic model consisting of 101 species and 511 reactions was validated by experimental results.

In some cases, the model constructed by a series of detailed molecular reactions cannot predict the product distribution as that obtained from experiments. The reasons are attributed to unclear reaction pathways for some species in the processes. Wang *et al*. [142] pointed out that the existing molecular reaction mechanism for Fischer-Tropsch (F-T) naphtha steam cracking failed to give the expected results. A new kinetic model including a primary decomposition of the pseudo-pure compound for naphtha was proposed in Equation 2.1. Following the first order primary reaction, 37 reactions of intermediate products such as CH_4, C_2H_4, C_3H_6, *etc*. can deliver the end-product distribution similar with the results obtained from experiments.

$$Naphtha \rightarrow 0.216H_2 + 0.476CH_4 + 1.631C_4H_4 \ \ldots \qquad 2.1$$

Nevertheless, the reaction mechanisms of biomass thermal decomposition are much more complicated. The whole reaction pathways cannot be introduced clearly due to the issues on identifying the components that appear in reactions. Some researchers have tried to propose the apparent chemical formulae for biomass and tar. A proportional formula was given as CH_xO_y for biomass where x and y are fixed value determined from experimental data [143]. Hence a chemical equation for biomass pyrolysis can be written as Equation 2.2 to define the mass transfer in the primary step of biomass decomposition. The subsequent reactions among the products of the primary step can be easily defined according to existing chemical equations for the corresponding species.

$$CH_xO_y = n_1C + n_2H_2 + n_3H_2O + n_4CO + n_5CO_2 + n_6CH_4 \quad 2.2$$

The biomass fast pyrolysis is very difficult to interpret by detailed molecular reaction schemes as thousands components exist or appear in the reactions [9]. The reacting pathways have not been well addressed and the kinetic schemes are simplified in several steps with grouped end products. As reported in literature [144], the relevant given values including the value of activation energy have to be corrected according to the experimental data. It aims to perform the yields of end products directly by simplifying the intermediate processes.

In general, a single- or multiple- step kinetic model to describe pyrolysis of biomass can be derived from thermogravimetric analysis (TGA) and derivative thermogravimetric (DTG) curves. The kinetic schemes were reviewed in detail by Di Blasi [17]. One or three pseudo-components were identified to decompose into three groups of products. Arrhenius equation was applied into calculating the depletion rate of reactants meanwhile the activation energy and pre-exponential factors were conducted from TG/DTG curves. Comparison of single- and multi- component mechanisms was reported where the two mechanisms were named as one-step model and three-pseudocomponent model, correspondingly [145]. Their work concluded that the multi-component mechanism (three-pseudocomponent model) in first order was consistent with experimental data. Based on the same approaches with various heating rates, further studies in another group showed that the multi-component mechanisms in n-order could give more realistic results for hemicellulose pyrolysis [146]. Furthermore, a new mechanism of cellulose pyrolysis was proposed. The whole process was described by 4 reacting pathways and the pyrolysis products were classified and detailed at the molecular scale [147]. It was a significant contribution on attempting to set up a detailed molecular reaction scheme.

Although the multi-component model shows more details about the biomass pyrolysis than single-component model, the species transforming routes were still unclearly determined. Based on the current approaches, demonstrating the pyrolysis process by molecular reaction scheme seems to be a tough task. Hence, both the single- and multi-component models were accepted widely. By considering the thermal cracking of the pyrolysis vapours (tar), the improved kinetic models coupling the secondary cracking reaction were proposed in predicting the yields of biomass pyrolysis products [20].

2.6 Incorporation of Reactions into Fluidized beds

2.6.1 Modelling of Fast Pyrolysis

Coupling existing molecular reactions into multiphase flow numerically is an applicable method to represent the relevant heat and mass transfer in reactions. The end-product distribution is supposed to be more accurate with the improving understanding in detailed reacting routes. The reactions in a fluid catalytic cracking (FCC) reactor were modelled by coupling 14-lump reaction kinetic scheme with CFD-PBM [111]. 48 reacting pathways were clarified for mass transfer between species. The simulation results showed that the particle size distribution imposed significant effects on hydrodynamics of multiphase flow. In another work of biomass gasification, the proportional formula, CH_xO_y, was defined for biomass [143]. There was no clear information which approach was employed to model the multiphase flow. However it was a new attempt by applying molecular reaction scheme for pyrolysis and gasification into multiphase flow numerically. This type of reaction scheme was also proposed by Boateng and Mtui [144] with the chemical formulae for biomass and pyrolysis vapours (tar), respectively. Bio-oil production of three kinds of biomass samples were predicted and compared with existing experimental data. As the limited reports of this type of schemes, modelling of biomass fast pyrolysis in a fluidized bed with a molecular scheme was seldom carried out.

The pseudo-component/molecular reaction schemes are widely used for describing wood and coal gasification. Based on this reaction scheme, the coal gasification in a fluidized bed reactor was modelled by E-E model or E-L model [119, 148] and the biomass gasification in a fluidized bed with char as the bed materials was numerically studied [149]. Extensive works on modelling of coal/biomass gasification [39, 150, 151] can be attributed to the deep understanding on the relevant mechanisms of hetero- and homo-generous reactions.

The utilizations of the pseudo-component scheme were reported in yield prediction of a single wood particle decomposition based on temperature profiles [152-155]. The radial temperature distribution inside a spherical or cylindrical particle was calculated by consideration of heat conduction from edge to centre. Formation of fractal pore structures has been studied [156] and the effect of different heating rates on pyrolysis progress was studied by modelling a single particle decomposition [157]. CFD coupling with this kinetic scheme for modelling of biomass pyrolysis was also reported. Lathouwers and Bellan [27, 158] introduced the Boltzmann equation to account the collisional transfer in CFD model of dense fluidized beds and the fractional yield distributions of end-products were predicted. One or several particles were identified in CFD modelling of gas-solid fluidized beds to study the flow characteristics and yield distributions of biomass fast pyrolysis [159-162]. Although the number of traced particles is limited by the numerical model in which TFM was employed to represent the hydrodynamics of fluidized bed while DEM for tracing biomass particles, the evolutions of the reacting particles were studied in detail such as the intra-particle heat conduction, particle shrinkage in reaction and particle entrainment in gas flow. The yields of biomass pyrolysis products were calculated by TFM coupling with the multi-component model by Xue *et al*. [163, 164] and the simulation results were validated by experiments. Mellin *et al*. numerically studied biomass fast pyrolysis with the similar approaches in 3-D, in which two different kinetic schemes applied into simulations: a single-component model [165] and a detailed

chemistry scheme [166]. In the latter scheme, biomass is written as $C_6H_{8.46}O_{y3.9}$ while the products of primary reaction were addressed with the reference species [9] including Phenol, Acetone, Acrylic-acid, *etc*. Due to the detailed reacting pathways, a good agreement was delivered between simulation and experimental results. For large particles, the temperature gradients due to the intra-particle heat transfer cannot be neglected and lead to the variation of local reaction rate. Thermal conductivity of wood had been specified and an effective thermal conductivity was delivered as a function of temperature, density and moisture [167]. It is clear that the mass and heat transfer in particle scale is practical by Lagrangian approaches. However the direct inspection is impossible for Eulerian approaches. Hence a modification of reaction constants by the empirical correlation was proposed to describe the effects of intra-particle heat conduction on chemical reactions [168]. The sensitivity of the reaction constant modification was discussed and a further validation needs to proceed.

2.6.2 Modelling of Catalytic Pyrolysis

Upgrading of bio-oil into petroleum-like fuels is one of the hottest topics on utilizing bio-oil. The approach of catalytic cracking used widely in petroleum industry has been introduced into upgrading the quality of bio-oil [169]. Research on the catalytic characteristics was carried out for a deep understanding of catalytic activity, catalytic selectivity and catalyst regeneration in bio-oil upgrading. Nilsen *et al*. [170] reported that metal sites in mesoporous material Al-MCM-41 varied the yields of phenols and coke. Xu *et al*. [171, 172] studied the catalytic activity on the conversion of acetic acid in bio-oil with ruthenium catalyst. Twaiq *et al*. [173] employed catalyst MCM-41 to improve the production of organic liquid product in conversion of palm oil to gasoline. All the experimental works pronounced that the catalytic cracking is effective in bio-oil upgrading to obtain expected products by using a specific catalyst. The experiments on biomass fast pyrolysis were carried out in a novel biomass auto-thermal fast pyrolysis reactor [174-176], which is designed to upgrade the pyrolysis bio-oil by the in-*situ* catalyst with the heat supply from the combustion of by-products. The system was derived from the concept of dual-bed reactors for biomass pyrolysis,

which has been commercialized in developed countries [177, 178]. Thus the technique of online catalytic upgrading of bio-oil is still limited by issues such as selectivity and regeneration of catalyst. ZSM-5 zeolite is one of the well-used catalysts in catalytic pyrolysis to produce petroleum-like fuels. The end-product (bio-oil) from catalytic pyrolysis consists of more aromatic carbon yield, especially with a high ratio of mono-aromatics [179]. However the deactivation rate of catalyst should be seriously concerned. Catalytic pyrolysis of sodium lignosulfonate was studied experimentally by applying HZSM-5 (an aluminosilicate zeolite) as the catalyst [180]. The experimental data from coupling of thermogravimetric analysis and fourier transform infrared spectroscopy (TG-FTIR) indicated that the dexoygenation of high molecular weight compounds contributes on yields of water, CO and CO_2. Compared to the great enthusiasm on catalyst experimental test, the kinetic studies are progressing slowly and the practical scheme representing the connection of yield distribution and catalyst concentration in bed was only introduced by Atutxa *et al*. [181].

2.7 Summaries

Despite extensive works have been introduce on heat transfer, hydrodynamics and thermochemical reactions in fluidized beds, the numerical prediction and representation of physicochemical phenomena still face challenge. According to the studies of previous works:

Over-prediction of heat transfer coefficient in heat exchange between the immersed tube and a fluidized bed has been addressed by the previous models. Performing an accurate prediction numerically needs more works meanwhile the effects of different surface shapes on local hydrodynamics and heat transfer processes should be studied.

Mixing and segregation phenomena of binary mixtures are still not extensively studied. It is not clear whether particles belonging to Geldart group B behave similarly to particles

of Geldart groups A or D in mixing-segregation of binary mixtures. (Referring to Chapter 3 for details of Geldart groups)

Representing biomass fast pyrolysis in a fluidized bed has been studied by TFM. Due to the limitation of Eulerian approaches, considering the intra-particle heat conduction into the Eulerian model faces challenges.

The modelling work on catalytic pyrolysis is absent as the slow development of practical kinetic schemes.

Chapter 3: Methodology

3.1 Introduction

Due to the fluid-like behavior of solid particles during fluidization, fluidized beds have been widely studied for decades. The fluidization mechanism is complicated in some aspects such as flow pattern, heat transfer, particle translation, bubble behavior, *etc*., numerically and experimentally. This chapter describes the characteristics of gas-solid fluidization regimes firstly. Then the numerical approaches available for multiphase flow are introduced together with the corresponding governing equations. A brief description of kinetic schemes is given and the detailed mass transfer pathways are performed by mass balance. Finally the numerical strategies and assumptions adopted in the present work are introduced.

3.2 Fluidization and Fluidized Beds

In a gas-solid fluidized bed, the solid particles are loaded on the bottom gas distributor where the fluidizing gas can be well controlled and injected uniformly. Fluidization is progressed when the solid particles are driven from static state into dynamic state by gas at a specific flow rate. In this condition, motions of particles behave like a fluid. Different stages of fluidization occur up to the varying superficial velocity of fluidizing gas, u_{sf}. The superficial velocity is the ratio of the fluidizing gas flow rate to the cross-sectional area of the bed. The physical properties of solid particles including shape, density and size affect the start points of the different fluidizing regimes.

Figure 3.1 shows the transitional stages by increasing gas velocity. The bed types can be classified as fixed bed (FB), bubbling fluidized bed (BFB), slugging bed (SB), turbulent bed (TB) and circulating fluidized bed (CFB) corresponding to different regimes: fixed bed, bubbling fluidization, slugging fluidization, turbulent fluidization and fast fluidization [182]. Fast fluidized bed and pneumatic bed are two types of CFB. For low or zero velocity the fluidizing gas flows pass through the gaps between particles. The

consequent frictional forces imposed on the particles are smaller than the gravitational force. No particle moves at this stage and the pressure drop within the bed is enlarged with the increasing gas flow rate. The bed with stationary particles is known as a FB.

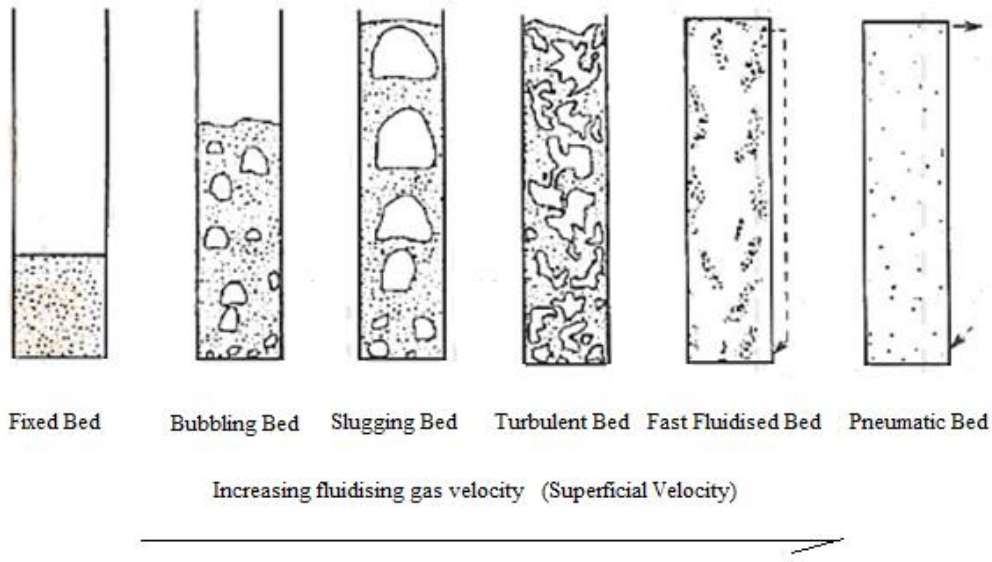

Figure 3.1 Fluidization transitional regimes [182].

The frictional force is a function of slip velocity between gas and solid particles. When it is equal to the gravitational force, the particles are suspended in the bed and intend to move with gas. From this point, the pressure drop of bed remains constant until the gas flow rate is high enough to entrain the particles out of the reactor. The corresponding gas velocity at this point is called as the minimum fluidization velocity, u_{mf}. The critical point of the defluidization curve of the pressure drop versus the superficial velocity is generally used to determine the minimum fluidization velocity as shown in Figure 3.2. When the gas velocity is higher than the minimum fluidization velocity, the homogenous fluidization exists until random bubbles generate nearby the distributor and grow up by collisions and coalescence during climbing up in the bed. The regime with appearance of bubbles is termed as bubbling fluidization and the corresponding velocity, when the bubbles are visible in bed, is called the minimum bubbling velocity, u_{mb}. For large

particles, the minimum bubbling velocity is much close to the minimum fluidization velocity and a tiny lag exists between commencement of fluidization and appearance of bubbles. In other words, the regime enters into bubbling fluidization immediately at the point of minimum fluidization of large particles [183].

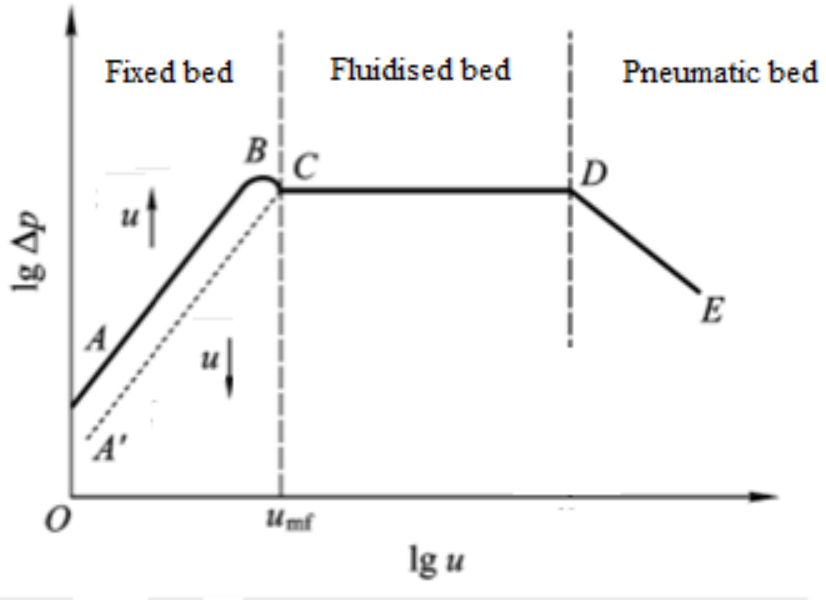

Figure 3.2 Connection between pressure drop and superficial velocity [183].

By increasing gas velocity further, the particles translation in bed vigorously lead to slugging or turbulent fluidization. When the gas superficial velocity is sufficiently rapid, the particles can be entrained out of the reactor and would not fall back to the bed without the help of cyclones. This regime is termed as fast fluidization. In a CFB particle clusters can be observed for relatively low-velocity period. Following the higher gas velocity, a pneumatic transport appears and the holdup of particles in the entrain flow is highly dilute and the particles distribute uniformly.

By employing the data from air fluidization at ambient conditions, the classification system of particles was developed by Geldart [24] as shown in Figure 3.3. Solid particles are categorized into four groups, A, B, C, D depending on the mean particle diameter and the density difference between the fluidizing gas and the solids.

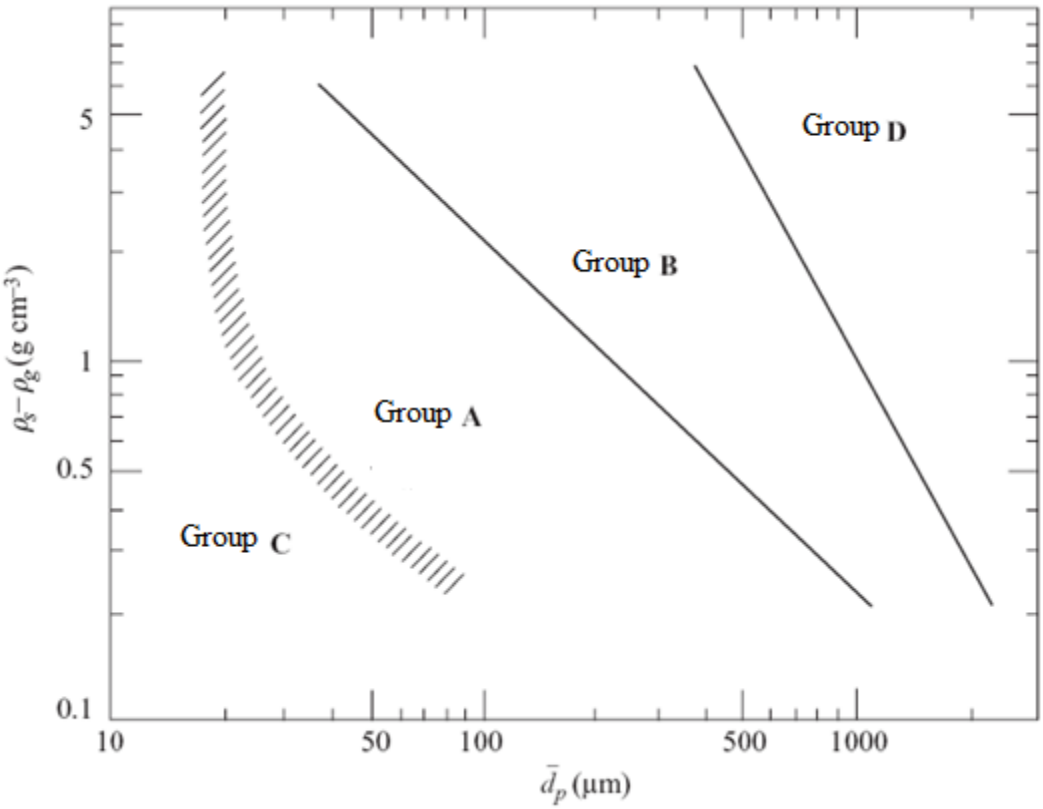

Figure 3.3 The Geldart classification system of particles [24].

Group A (Aerated): The mean size of solid particles is in the range of 20 ~ 100 μm and a density less than 1400 kg/m^3. For group A particles, the homogeneous fluidization occurs visibly during the transition from fixed bed to bubbling bed. Due to the small size or low density, the particles are easily fluidized and circulated which is commonly used for fluid catalytic cracking (FCC) in petroleum refineries.

Group B (Sand-like): The mean particle size is in the range of 40~500 μm and a density 1400 ~ 4000 kg/m^3. For group B particles, an ignorable lag exists between the minimum fluidization point and the bubbling fluidization stage. Sand is the typical particles belong to this group.

Group C (Cohesive): Very fine and cohesive particles (20~30 μm or smaller in size) such as flour. It is hard to fluidize this type of particles because the inter-particle forces are

stronger than the drag forces from the fluidizing gas on the particles. Channelling occurs when subject to fluidization.

Group D (Spoutable): Very large and/or dense particles (*e.g.* roasting coffee beans and drying peas). For group D particles, the high levels of abrasion have to be considered in fluidization. They are usually loaded in shallow beds or in the spouting model.

The minimum fluidization velocity of particles is significant in running of the fluidized beds. According to the Ergun equation [61], the equations to calculate the pressure drop of a fixed bed can be expressed as follows:

$$\frac{\Delta p}{H_{fix}} = (1.75 + \frac{150}{Re_m}) \frac{\rho_g u_{sf}^2}{\phi d_p} (\frac{1-\varepsilon}{\varepsilon^3}) \quad 3.1$$

and

$$Re_m = \frac{\phi d_p \rho_g u_{sf}}{\mu_g} (\frac{1}{1-\varepsilon}) \ , \quad 3.2$$

where Δp and H_{fix} are the pressure drop and the height of the fixed bed, respectively, ρ_g is the density of the fluidizing gas, d_p is the particle size, ϕ is the sphericity, μ_g is the gas viscosity and ε is the voidage of the bed.

When the pressure gradient along the vertical direction is equal to the apparent weight of packing particles per unit volume of the bed, the minimum fluidization takes place [184]. The balance is given as Equation 3.3:

$$\frac{\Delta p}{H_{mf}} = (1 - \varepsilon_{mf})(\rho_s - \rho_g)g, \quad 3.3$$

where H_{mf} and ε_{mf} are the height and voidage of the bed at minimum fluidization, respectively.

At the critical point, the following balance exists by combining the Equations 3.1-3.3:

$$(1.75 + \frac{\mu_g(1-\varepsilon_{mf})150}{\phi d_p \rho_g u_{sf}}) \frac{\rho_g u_{mf}^2}{\phi d_p} (\frac{1-\varepsilon_{mf}}{\varepsilon_{mf}^3}) = (1-\varepsilon_{mf})(\rho_s - \rho_g)g \quad 3.4$$

and the following equation is deduced to calculate the minimum fluidization velocity:

$$\frac{1.75}{\phi \varepsilon_{mf}^3} (Re_{mf})^2 + \frac{150(1-\varepsilon_{mf})}{\phi^2 \varepsilon_{mf}^3} Re_{mf} = Ar \quad 3.5$$

where Ar and Re_{mf} are defined as

$$\frac{d_p^3 \rho_g (\rho_s - \rho_g) g}{\mu_g^2} = Ar \quad 3.6$$

and

$$\frac{d_p \rho_g u_{mf}}{\mu_g} = Re_{mf}. \quad 3.7$$

In Equation 3.4, ε_{mf} and ϕ are required. However it is difficult to determine them and they are always given empirically. The following approximations based on experimental data were proposed by Wen and Yu [185]:

$$\frac{1}{\phi \varepsilon_{mf}^3} \approx 14 \quad 3.8$$

and

$$\frac{1-\varepsilon_{mf}}{\phi^2 \varepsilon_{mf}^3} \approx 11. \quad 3.9$$

Hence the minimum fluidization velocity can be predicted by the simplified semi-empirical equation:

$$Re_{mf} = \frac{d_p \rho_g u_{mf}}{\mu_g} = \sqrt{33.7^2 + 0.0408Ar} - 33.7. \quad 3.10$$

Other correlations were also available and introduced in literature [186-191].

3.3 Mathematical Models

For a fluid flow, prediction of the hydrodynamics is not a profoundly difficult task although some issues are still standing in the way. In studies of the gas-solid multiphase flow, the difficulties come from the presence of solid particles and the complicated instantaneous interactions between the gas and solids. Two classical approaches are available to describe the flow behavior of the particles in multiphase flow: Lagrangian and Eulerian approaches. Due to the application of Eulerian approach in chapters 4-7, only a brief introduction of Lagrangian approach is given.

3.3.1 Lagrangian Model

To obtain the detailed information such as the trajectories and mass & heat transfer in particle-scale, a Lagrangian type model is required which treats the particles individually using Newton's law. The translation and rotation of particle are dominated by drives of different forces imposing on the particle. The force balance equations for particle translation and rotation are introduced as Equations 3.11 and 3.12 [32], respectively.

$$m_p \frac{d\vec{u}_p}{dt} = \vec{F}_{gra} + \vec{F}_{buo} + \vec{F}_{dra} + \sum_{col} \vec{F}, \quad 3.11$$

$$\frac{2}{5} m_p r_p^2 \frac{d\vec{\omega}_p}{dt} = \sum_{col} \vec{F}_{tor}, \quad 3.12$$

Where $\vec{u}_p$ and $\vec{\omega}_p$ are the translational and rotational particle velocity vector, m_p and r_p are the particle mass and radius, $\vec{F}_{gra}$ and $\vec{F}_{buo}$ are gravitational and buoyancy force, $\vec{F}_{dra}$ is the drag force from interactions with fluid, $\vec{F}_{tor}$ is the torque acting on the particle, $\vec{F}$ is the collisional force generated in the particle collisions. The relevant details of collisional force and torque in particle collisions were introduced by van der Hoef *et al*.[30].

The heat exchange between the surrounding and a particle can be described by convective heat transfer equation (Equation 3.13)

$$\frac{\Delta T_p}{\Delta t} = \frac{\Lambda_p \dot{h}}{m_p Cp}(T_g - T_p), \quad 3.13$$

where T_g and T_p are the fluid and particle temperatures, Λ is the particle surface area, $\dot{h}$ is the heat transfer coefficient and Cp is the specific heat capacity.

The intra-particle temperature distribution along the radial direction can be determined by the heat diffusion equation (Equation 3.14) [192]:

$$\frac{\partial(\rho_S Cp T)}{\partial t} = \frac{1}{r^2}\frac{\partial}{\partial r}\left(\lambda r^2 \frac{\partial T}{\partial r}\right) + \dot{S}. \quad 3.14$$

The last term on the right-hand side of Equation 3.14 describes the heat source for internal heat generation such as the reaction heat.

Based on the equations demonstrated above, the details of particles in multiphase flow can be tracked on the micro- and macro- motions by coupling the interactions with gas. As reported by van der Hoef *et al*. [30], the gas-particle interactions can be expressed by empirical correlations for drag force or by boundary conditions at the particle surface. The drawback is that both the two models require intensive computational workloads for the limited amount of particles.

3.3.2 Eulerian Model

The fluid-like behavior of particles in fluidization of multiphase flow has been studied for decades[183, 193]. Although the particles are disperse entities in packing, the gas-fluidized particles show the similar dynamic characteristics with fluid such as

horizontal surface, levels equalization, pressure variation, *etc*., as shown in Figure 3.3. Therefore, The Navier-Stokes (*N*-*S*) equation is supposed to be suitable to represent the fluidized particle motions. The governing equations are given as follows:

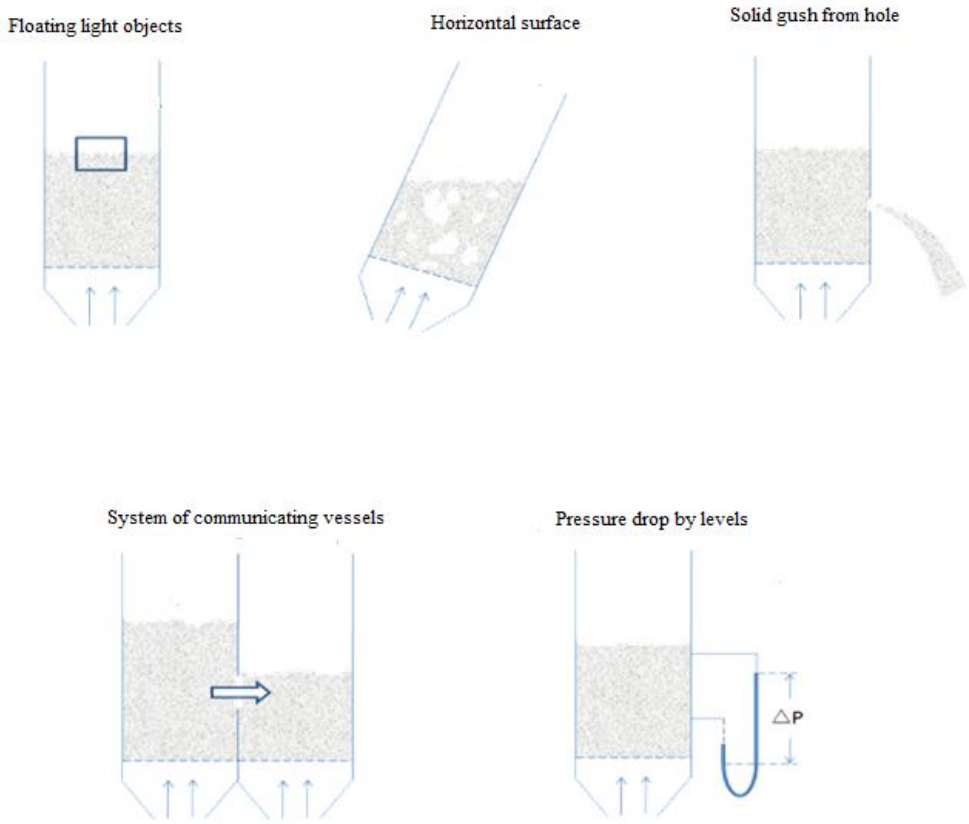

Figure 3.4 Fluid-like behavior of gas-solid fluidization [194].

Mass balance

By Eulerian approaches, both of the gas and solid phases are treated as continuua with individual volume fraction, $\varepsilon_i,\ i = g, s_1, s_2 \cdots$. In a control volume, the sum of the volume fractions of gas and solid phases is equal to 1:

$$\sum \varepsilon_i = 1 \qquad 3.15$$

The continuity equations are shown as follows and the mass exchange rate between phases takes into account by the source term, $\dot{S}_{i,j}$, if the heterogeneous reactions take place.

$$\frac{\partial}{\partial t}(\varepsilon_i \rho_i) + \nabla \cdot (\varepsilon_i \rho_i \vec{u}_i) = \dot{S}_{i,j}, \tag{3.16}$$

where ρ_i is the density of phase i and $\vec{u}_i$ is the velocity.

Momentum balance

The typical *N-S* equations coupling with the interphase interaction force are set up for gas and solid phases. The momentum change rate of the gas or solid phase is determined by all the forces acting on it:

$$\frac{\partial}{\partial t}(\varepsilon_i \rho_i \vec{u}_i) + \nabla \cdot (\varepsilon_i \rho_i \vec{u}_i \vec{u}_i) = -\varepsilon_i \nabla p - (\nabla p_s) + \nabla \cdot \bar{\bar{\tau}}_i + \varepsilon_i \rho_i \vec{g} + \sum \vec{F} + \vec{R}_{j,i}. \tag{3.17}$$

The first term on the right-hand side is the forces by local pressure gradients. ∇p_s, considering the solid pressure gradients, is only present in the momentum conservation equation for solid phases. The fourth term on the right-hand side is the gravitational force.

$\bar{\bar{\tau}}_i$, is the stress-stain tensor

$$\bar{\bar{\tau}}_i = \varepsilon_i \mu_i (\nabla \vec{u}_i + \nabla \vec{u}_i^T) + \varepsilon_i \left(\xi_i - \frac{2}{3}\mu_i\right) \nabla \cdot \vec{u}_i \bar{\bar{I}}, \tag{3.18}$$

where ξ_i and μ_i are the bulk and shear viscosity of phase i, $\bar{\bar{I}}$ is the stress tensor identity matrix.

$\vec{F}$, can be other forces such as the external body force, the lift force, the virtual mass force but not limited to those. The typical external body forces including magnetic forces, electric forces, *etc*., are only considered in specific systems. The lift forces take into account of the effects of velocity gradients. The higher velocity gives rise on lower pressure and lower velocity gives rise to higher pressure as shown in Figure 3.5. Hence the induced pressure difference gives rise to a lift force [195] which is ignorable for small size particles in dense phase. The virtual mass force is due to a relative acceleration of particles through a fluid [196]. If the density of the carrier fluid is much higher than the particles, the virtual mass force has to be taken into account. Compared to the drag and gravitational forces, other forces are ignorable and will not be considered here.

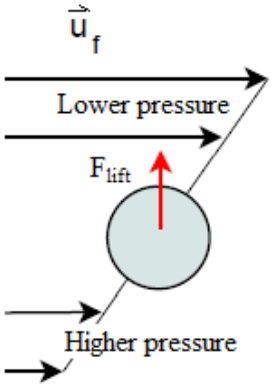

Figure 3.5 The lift force for particle in shear flow [195].

The term, $\vec{R}_{j,i}$, describes the interphase interaction force which derives by friction, pressure, *etc*. Here a simple function of the interphase momentum exchange coefficient and the slip velocity is used:

$$\vec{R}_{j,i} = -\vec{R}_{i,j} = K_{j,i}\left(\vec{u}_j - \vec{u}_i\right). \qquad 3.19$$

For a dilute system with low concentration of solids, Wen and Yu gave the fluid-solid exchange coefficient [62]

$$K_{s,g} = K_{g,s} = \frac{3}{4} C_D \frac{\varepsilon_g \varepsilon_s \rho_g |\vec{u}_s - \vec{u}_g|}{d_s} \varepsilon_g^{-2.65}, \quad 3.20$$

and the drag coefficient is defined as

$$C_D = \frac{24}{\varepsilon_g Re_s} \left[1 + 0.15 \left(\varepsilon_g Re_s\right)^{0.687}\right] \quad 3.21$$

where Re_s is the relative Reynolds number of solids

$$Re_s = \frac{d_s \rho_g |\vec{u}_s - \vec{u}_g|}{\mu_g}. \quad 3.22$$

For a dense system, $K_{s,g}$ between solid and gas phases can be expressed according to Ergun equation [61] as:

$$K_{s,g} = K_{g,s} = 150 \frac{\varepsilon_s^2 \mu_g}{\varepsilon_g d_s^2} + 1.75 \frac{\varepsilon_s \rho_g |\vec{u}_s - \vec{u}_g|}{d_s} \qquad \varepsilon_g \leq 0.8 \qquad 3.23$$

Gidaspow, *et al*. [60] employed the two exchange coefficients together for modelling both the dense and dilute regions in the fluidized beds, which is widely accepted in simulations of fluidization of gas-solid dense beds:

$$K_{s,g} = K_{g,s} = 150 \frac{\varepsilon_s^2 \mu_g}{\varepsilon_g d_s^2} + 1.75 \frac{\varepsilon_s \rho_g |\vec{u}_s - \vec{u}_g|}{d_s} \qquad \text{for } \varepsilon_g \leq 0.8, \qquad 3.24$$

$$K_{s,g} = K_{g,s} = \frac{3}{4} C_D \frac{\varepsilon_g \varepsilon_s \rho_g |\vec{u}_s - \vec{u}_g|}{d_s} \varepsilon_g^{-2.65} \qquad \text{for } \varepsilon_g > 0.8, \qquad 3.25$$

where C_D is given by

$$C_D = \frac{24}{\varepsilon_g Re_s}\left[1 + 0.15\left(\varepsilon_g Re_s\right)^{0.687}\right] \quad 3.26$$

and

$$Re_s = \frac{d_s \rho_g |\vec{u}_s - \vec{u}_g|}{\mu_g}. \quad 3.27$$

Constitutive equations

For granular flows, more equations are required for the closure of the momentum conservation as the unresolved solid pressure, p_s, solids shear viscosity, μ_s and solids bulk viscosity, ξ_s.

Based on the kinetic theory of granular flow, the solid pressure is defined by Lun *et al.* [59] as

$$p_s = \varepsilon_s \rho_s \Theta_s + 2\rho_s(1 + e_{ss})\varepsilon_s^2 g_0 \Theta_s, \quad 3.28$$

where Θ_s is the granular temperature, e_{ss} is the coefficient of restitution and g_0 is the radial distribution function.

Due to the translation and collision, the proposed expression of the shear viscosity is composed of a kinetic term, a collisional term and the optional frictional part:

$$\mu_s = \mu_{s,col} + \mu_{s,kin} + \mu_{s,fri}. \quad 3.29$$

The collisional and kinetic terms of the shear viscosity are defined as [60]:

$$\mu_{s,col} = \frac{4}{5}\varepsilon_s \rho_s d_s g_{0,ss}(1 + e_{ss})\sqrt{\left(\frac{\Theta_s}{\pi}\right)} \quad 3.30$$

and

$$\mu_{s,kin} = \frac{10\rho_s d_s\sqrt{\Theta_s \pi}}{6(1+e_{ss})g_{0,ss}}[1 + \frac{4}{5}g_{0,ss}\varepsilon_s(1+e_{ss})]^2. \quad 3.31$$

A frictional viscosity is taken into account when the volume fraction of dense flow is much close to the maximum packing limit of the particles in a control volume [197]:

$$\mu_{s,fri} = \frac{p_s sin\varphi}{\sqrt{I_{2D}}}, \quad 3.32$$

where the angle of internal friction, φ, is typically given of 30° and I_{2D} is the second invariant of the deviatoric strain rate tensor [35, 198]:

$$I_{2D} = \frac{1}{6}[(D_{11} - D_{22}) + (D_{22} - D_{33}) + (D_{33} - D_{11}) + D_{12}^2 + D_{23}^2 + D_{31}^2]. \quad 3.33$$

D_{ij} are the components of the strain rate tensor $\overline{\overline{\boldsymbol{D}}}$ which is also given [197] as

$$\overline{\overline{\boldsymbol{D}}} = \frac{1}{2}(\nabla\vec{u}_i + \nabla\vec{u}_i^T). \quad 3.33$$

The bulk viscosity is [59]

$$\xi_s = \frac{4}{3}\varepsilon_s\rho_s d_s g_{0,ss}(1+e_{ss})\sqrt{\left(\frac{\Theta_s}{\pi}\right)}. \quad 3.34$$

The coefficient of restitution, e_{ss}, accounts the dynamic energy generation or dissipation during a collision of a pair of particles. The coefficient equals to 1 indicate that the elastic collision occurs.

The radial distribution function, g_0, described as a nondimensional distance between objects is a correction factor to modify the collision probability in dense solid granular phase. The expression for one solid phase was given by Ogawa *et al.* [199]:

$$g_{0,ss} = \left[1 - \left(\frac{\varepsilon_s}{\varepsilon_{s,max}}\right)^{1/3}\right]^{-1}. \tag{3.34}$$

where $\varepsilon_{s,max}$ is the maximum packing limit of solids which may change for different particle sizes or shapes, *etc*.

When two solid phases are present, the following expression suggest by Syamlal *et al*. [198] is available:

$$g_{0,s1s2} = \frac{1}{1-\varepsilon_s} + \frac{3d_{s1}d_{s2}}{(1-\varepsilon_s)^2(d_{s1}+d_{s2})}\left(\frac{\varepsilon_{s1}}{d_{s1}} + \frac{\varepsilon_{s2}}{d_{s2}}\right) \tag{3.35}$$

where $s1$ and $s2$ denote the different solid phases.

Corresponding to the definition of temperature from Brown's motion in molecular scale, granular temperature, Θ_s, is proposed to describe the kinetic energy dissipation of the fluctuating motion of the particles and the detailed introduction is given in kinetic theory of granular flow (KTGF) [60, 188]. The following equation being solved for Θ_s is defined similar to a typical transport equation for temperature:

$$\frac{3}{2}\left[\frac{\partial}{\partial t}(\alpha_s\rho_s\Theta_s) + \nabla\cdot(\alpha_s\rho_s\Theta_s\vec{u}_s)\right] = \left(-p_s\bar{\bar{I}} + \bar{\bar{\tau}}_s\right):\nabla\vec{u}_s + \nabla\cdot\left(\kappa_{\Theta_s}\nabla\Theta_s\right) - \gamma_{\Theta_s} - 3K_{gs}\Theta_s. \tag{3.36}$$

The energy generation related to the solid pressure, p_s, and shear stress, $\bar{\bar{\tau}}_s$, is introduced by the first term on the right-hand side. The energy diffusion by gradient of granular

temperature is represented by the second term. κ_{Θ_s}, the diffusion coefficient can be written by [188]:

$$k_{\Theta_s} = \frac{150 d_s \rho_s \sqrt{\Theta_s \pi}}{384(1+e_{ss}) g_{0,ss}} \left[1 + \frac{6}{5}\varepsilon_s g_{0,ss}(1+e_{ss})\right]^2 + 2\varepsilon_s^2 d_s \rho_s g_{0,ss}(1+e_{ss})\sqrt{\frac{\Theta_s}{\pi}}. \quad 3.37$$

Two additional terms are present on the right-hand side of Equation 3.26 due to collisional dissipation of energy and interphase exchange. The expression of collisional dissipation given by Lun *et al*. [59] is:

$$\gamma_{\Theta_s} = \frac{12(1-e_{ss}^2) g_{0,ss}}{d_s \sqrt{\pi}} \rho_s \varepsilon_s^2 \Theta_s^{\frac{3}{2}}. \quad 3.38$$

While K_{gs} is the interphase exchange coefficient. By incorporation of Equations 3.28-3.38, the momentum conservation of solid phase achieves a closure.

Energy balance

The energy conservation equation can be written as an expression of enthalpy balance as

$$\frac{\partial(\varepsilon_i \rho_i \Psi_i)}{\partial t} + \nabla \cdot \left(\varepsilon_i \rho_i \Psi_i \vec{u}_i\right) = -\varepsilon_i \frac{\partial p_i}{\partial t} + \bar{\bar{\tau}}_i : \nabla \vec{u}_i - \nabla \cdot \vec{q}_i + \vec{Q}_{j,i} + \dot{S}_i \quad 3.39$$

where Ψ_i is the specific enthalpy of phase i. The terms on the right-hand side represent the enthalpy generation derived by pressure (p_i) and shear stress ($\bar{\bar{\tau}}_i$), heat flux ($\vec{q}_i$) and interphase exchange heat ($\vec{Q}_{j,i}$) together with a source term ($\dot{S}_i$) including internal heat source, reaction heat, *et al.* $\vec{Q}_{s,g}$ is given as

$$\vec{Q}_{g,s} = -\vec{Q}_{s,g} = h_{g,s}(T_g - T_s), \quad 3.40$$

where $h_{i,j}$ is the volumetric interphase heat transfer coefficient which can be estimated by following equation

$$h_{gs} = h_{sg} = \frac{6\lambda_g \varepsilon_g \varepsilon_s Nu_s}{d_s^2}, \quad 3.41$$

where λ_g is the thermal conductivity of gas phase. The Nusselt number [84], Nu_s is given by incorporating the relative Reynolds number and Prandtl number:

$$Nu_s = \left(7 - 10\varepsilon_g + 5\varepsilon_g^2\right)\left(1 + 0.7Re_s^{\frac{1}{5}}Pr^{\frac{1}{3}}\right) + (1.33 - 2.4\varepsilon_g + 1.2\varepsilon_g^2)Re_s^{\frac{7}{10}}Pr^{\frac{1}{3}} \quad 3.42$$

and

$$Pr = \frac{Cp_g \mu_g}{\lambda_g} \quad 3.43$$

where Cp is the specific heat capacity and μ_g is the gas viscosity.

3.4 Kinetic Schemes

3.4.1 Biomass Pyrolysis

Based on the studies on cellulose pyrolysis, a three-stage series mechanism proposed by Bradbury *et al.* [20] is demonstrated in Figure 3.6:

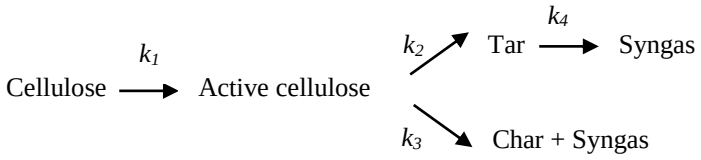

Figure 3.6 cellulose pyrolysis scheme by Bradbury *et al.* [20].

The mechanism is applied to describe biomass pyrolysis by incorporating the degrading schemes of hemicellulose and lignin additionally. Hence the thermal decomposition of biomass consists of three pseudo-components independent degradation. The detailed mechanism as the proposal of Lathouwers and Bellan [27] is given in Figure 3.7:

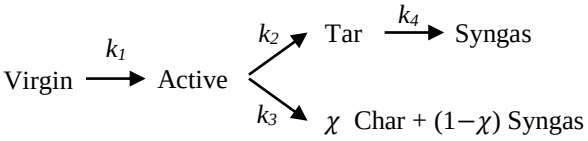

Figure 3.7 pyrolysis scheme of three pseudo-components of biomass [27].

In the multi-component scheme, the virgin presenting each pseudo-component degrades into a corresponding reaction intermediate (active) with a kinetic constant, k_1 and χ is given value based on experimental data. The yields of three end-products, char, tar and syngas are the sum of the productions by the parallel degradation of the three actives, meanwhile the thermal cracking of tar is considered in addition. Lathouwers and Bellan scheme reflects the degradation of different pseudo-components. However the interactions of the three degrading processes cannot be defined here meanwhile the reaction rates of virgin to active are difficult to measure and the presence of actives is also controversial. The mass transfer in the three-component scheme is given below. The kinetic constant k_i is an expression in terms of first order Arrhenius equation in general:

$$k_i = A_i \exp(-E_i/RT) \qquad 3.44$$

where R is the universal gas constant. The values for Pre-exponential factor A_i and Activation energy E_i are given in Table 3.1.

The degrading rate of biomass is calculated by sum of the depletion rate of each component:

$$\frac{dm_{bio}}{dt} = \frac{dm_{cel}}{dt} + \frac{dm_{hem}}{dt} + \frac{dm_{lig}}{dt} = -k_{1,cel}m_{cel} - k_{1,hem}m_{hem} - k_{1,lig}m_{lig}. \qquad 3.45$$

where m_{bio}, m_{cel}, m_{hem} and m_{lig} are the mass of biomass, cellulose, hemicellulose and lignin.

The production of each active:

$$\frac{dm_{act,cel}}{dt} = k_{1,cel}m_{cel} - k_{2,cel}m_{act,cel} - k_{3,i}m_{act,cel}, \quad 3.46$$

$$\frac{dm_{act,hem}}{dt} = k_{1,cel}m_{hem} - k_{2,hem}m_{act,hem} - k_{3,i}m_{act,hem} \quad 3.47$$

and

$$\frac{dm_{act,lig}}{dt} = k_{1,lig}m_{lig} - k_{2,lig}m_{act,lig} - k_{3,i}m_{act,lig}, \quad 3.48$$

where $m_{act,cel}$, $m_{act,hem}$ and $m_{act,lig}$ are the corresponding active productions from cellulose, hemicellulose and lignin.

The productions of char, tar and syngas from cellulose, hemicellulose and lignin are given by

$$\frac{dm_{char}}{dt} = \sum \chi_i k_{3,i}m_{act,i}, \quad 3.49$$

$$\frac{dm_{tar}}{dt} = \sum\left(k_{2,i}m_{act,i} - k_{4,i}m_{tar,i}\right), \quad 3.50$$

and

$$\frac{dm_{syn}}{dt} = \sum\left((1-\chi_i)k_{3,i}m_{act,i} + k_{4,i}m_{tar,i}\right), \quad 3.51$$

where i denotes cellulose, hemicellulose or lignin and χ_i are the given values of 0.35, 0.6 and 0.75.

Table 3.1 Pre-exponential factor and Activation energy for the kinetics [27]

Kinetic constant	$A_i(1/s)$	$E_i(J/kmol)$
$k_{1,cel}$	2.8×10^{19}	2.424×10^{8}
$k_{2,cel}$	3.28×10^{14}	1.965×10^{8}
$k_{3,cel}$	1.30×10^{10}	1.505×10^{8}
$k_{1,hem}$	2.10×10^{16}	1.867×10^{8}
$k_{2,hem}$	8.75×10^{15}	2.024×10^{8}
$k_{3,hem}$	2.60×10^{11}	1.457×10^{8}
$k_{1,lig}$	9.60×10^{8}	1.076×10^{8}
$k_{2,lig}$	1.50×10^{9}	1.438×10^{8}
$k_{3,lig}$	7.70×10^{6}	1.114×10^{8}
k_4	4.28×10^{6}	1.08×10^{8}

3.4.2 Catalytic Pyrolysis

The proposed catalytic pyrolysis scheme of sawdust shown in Figure 3.7 [181] is introduced by improving the one-component mechanism by Shafizadeh and Chin [19].

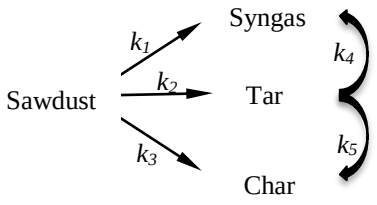

Figure 3.8 The catalytic pyrolysis scheme by Atutxa *et al*. [181].

The corresponding mass transfer among species is given below:

The depletion rate of sawdust by one component scheme:

$$\frac{dm_{saw}}{dt} = -k_1 m_{saw} - k_2 m_{saw} - k_3 m_{saw} \quad 3.52$$

where m_{saw} is the sawdust mass.

The productions of the syngas ($m_{syn,1st}$), tar ($m_{tar,1st}$) and char ($m_{char,1st}$) in sawdust primary pyrolysis (first step):

$$\frac{dm_{syn,1st}}{dt} = k_1 m_{saw}, \quad 3.53$$

$$\frac{dm_{tar,1st}}{dt} = k_2 m_{saw} \quad 3.54$$

and

$$\frac{dm_{char,1st}}{dt} = k_3 m_{saw}. \quad 3.55$$

The yields of syngas ($m_{syn,2nd}$) and char ($m_{char,2nd}$) by tar cracking (second step):

$$\frac{dm_{syn,2nd}}{dt} = k_2 m_{saw} \left\{1 - exp\left[-k_4 \left(\frac{m_{cata}}{\dot{m}_{tar}}\right)\right]\right\} \quad 3.56$$

and

$$\frac{dm_{char,2nd}}{dt} = \frac{k_5 k_2}{1+k_5} m_{saw} exp\left[-k_4 \left(\frac{m_{cata}}{\dot{m}_{tar}}\right)\right], \quad 3.57$$

where m_{cata} is the catalyst mass and $\dot{m}_{tar}$ is the mass flow rate of tar.

Hence the final productions of syngas, tar and char are:

$$\frac{dm_{syn}}{dt} = k_1 m_{saw} + k_2 m_{saw} \left\{1 - exp\left[-k_4 \left(\frac{m_{cata}}{\dot{m}_{tar}}\right)\right]\right\}, \quad 3.58$$

$$\frac{dm_{tar}}{dt} = \frac{1}{1+k_5} k_2 m_{saw} exp\left[-k_4 \left(\frac{m_{cata}}{\dot{m}_{tar}}\right)\right], \quad 3.59$$

and

$$\frac{dm_{char}}{dt} = k_3 m_{saw} + \frac{k_5 k_2}{1+k_5} m_{saw} exp\left[-k_4 \left(\frac{m_{cata}}{\dot{m}_{tar}}\right)\right] \quad 3.60$$

The kinetic constants for the catalytic scheme are given in Table 3.2.

Table 3.2 Pre-exponential factor and activation energy for the kinetics [181]

Kinetic constant	$Value$
$k_1(1/s)$	3.68×10^{-3}
$k_2(1/s)$	2.17×10^{-2}
$k_3(1/s)$	1.25×10^{-3}
$k_4(g/(gs))$	8.58×10^{-5}
k_5	0.157

3.5 Numerical Strategy

Spatial and temporal discretization is significant in simulation via finite volume method (FVM). Hence, the setup of mesh and option of time-step have to be carried out cautiously. Grid independent test needs to be carried out firstly to minimize the influence of mesh on the results in the model predictions. As reported in literature [94, 200], the size for grid independence is strongly related to the particle diameter, a mesh with the grid size smaller than 10 particle diameters shows no substantial difference on predicting the flow structure. A detailed discussion on grid independence has been carried out in Chapter 5 and the grid size smaller than 4 mm is defined throughout the thesis depending on the particle size.

Generally, no-slip boundary conditions for the wall are defined for gas phase in modelling of fluidized beds due to the existence of a boundary layer near the wall. However it is difficult to tell which one is the best from partial-slip and free-slip boundary conditions for solid phase. The no-slip boundary condition was also applied [97]. The different suggestions were given: Chen *et al.* preferred to use the free-slip boundary conditions [96] and Li *et al*. [94] recommended the partial-slip boundary conditions with the specularity

coefficient of 0.005 whilst Lan *et al*. [95] gave the value of 0.05. Due to inconsistency in the definition of boundary conditions for solid phase, both the no-slip and free-slip conditions are applied in different chapters.

Turbulent diffusion is a very important phenomenon in mixing of species and in high velocity fields. The gas-mixing in a fluidized bed was investigated by considering the gas and solid turbulence [93]. However, the gas-solid turbulence is suggested to be ignorable in dense solid beds [201-204]. Meanwhile most of the works employ a basic turbulent model but no approximation analysis. The issues are even the existing turbulent models are suitable for solid motion, the grid size used in simulations of fluidized beds still cannot capture the turbulent phenomena effectively. No turbulent model is implemented in modelling here.

The commercial code ANSYS-FLUENT 12 is used for the resolution of governing and constitutive equations while the reaction schemes are incorporated by UDF. Due to the simple structure of the fluidized bed reactors, a structured meshing method is employed to discretize the computational domain and the convective terms are treated by first order upwind. The relevant details will be given for each simulation in following chapters.

3.6 Assumptions

Because the modelling work cannot set up a model completely matching the reality. Several assumptions or simplifications are given as follows:

Solid particles such as sand, catalyst and biomass samples are all treated as perfect spheres with the identical size individually.

The perfect spherical solids are difficult to collect and the realistic particle size distribution can be controlled in a range up to the sieving precision. The particle

sphericity is always given of an empirical value in practical calculations. The effects of particle shape and size distribution are not considered in the current works.

Shrinkage and porous structure of biomass particles are not studied.

During the chemical reaction, the vapors and gases volatilizing from biomass samples lead to the shrinkage in size and form pores inside particles. As the limitation of E-E model, the relevant phenomena in particle scale are not specified.

Species diversity

The biomass comprised of three pseudo-components is generally accepted. However, for different samples, the decomposition of components is not the same. The interactions among the pseudo-components are not handled clearly. In the simulations, the pseudo-components degrade individually.

Moisture evaporation

Samples are presumed to be perfectly dried in modelling and no moisture evaporation exists during the heating up of cold particles. In experiments, moisture cannot be removed completely by pretreatment.

Chapter 4: Heat Exchange

4.1 Introduction

Bubbling fluidized beds have been widely utilised in the industrial sectors for decades because of their high heating rates, uniform temperature distributions and scale-up potential [18]. Empirical and numerical studies have been carried out but computational multiphase flow models are the preferred method to analyse the interactions between the gas and the solid particles. During fluidization the transition and formation of bubbles in the vicinity of heat exchangers are important factors in understanding the heat transfer between phases. Unfortunately, industrial processes cannot be easily measured, due to the relative small scale or complicated operational conditions, so numerical methods have been considered as a useful tool to display details that cannot be obtained directly from the experiments. Based on the progresses achieved by previous studies and the results from experiments by Di Natale [73], the current work applies the TFM to study the heat transfer in a fluidized bed with different shaped immersed tubes. An extensive study of the influence of tube shapes is not considered numerically yet. The computational results will be validated with the experimental data.

4.2 CFD Model

4.2.1 Mathematical Model

In the current work, the two-fluid model (TFM) and kinetic theory of granular flow (KTGF) are employed to model the gas-solid two-phase flow in the fluidized beds. The governing and constitutive equations are given in Chapter 3. For the momentum exchange between phases the Gidaspow drag function is used to represent the interactions between gas and solid phases and is valid for both dilute and dense particle regions. To consider the interactions between the particles within the solid phase, the bulk viscosity and solid pressure are used to express the normal forces during collisions while the shear viscosity for tangential forces. The probability of collisions is corrected with the radial distribution

function. The energy equation to be solved is in the function of enthalpy balance, and the energy transfer rate between two phases is a function of temperature difference, volume fraction, thermal conductivity of gas, diameter of particles and Nusselt numbers. The interphase heat transfer coefficient is employed which is related to the particle Reynolds numbers and Prandtl numbers. The effective thermal conductivities for the solid and gas phases were taken by Kuipers *et al*. [75]and Patil *et al*. [78] and were used to determine the local instantaneous heat transfer coefficient, $\dot{h}$, as follows:

$$\dot{h} = \frac{\varepsilon_g \lambda_g^{eff} \left|\frac{\partial T_g}{\partial n}\right| + \varepsilon_s \lambda_s^{eff} \left|\frac{\partial T_s}{\partial n}\right|}{T_{wall} - T_{bulk}} \ , \tag{4.1}$$

$$\lambda_g^{eff} = \left(\frac{1-\sqrt{\varepsilon_s}}{\varepsilon_g}\right)\lambda_g \ , \tag{4.2}$$

$$\lambda_s^{eff} = \frac{1}{\sqrt{\varepsilon_s}}\,\lambda_g[\omega A + (1-\omega)\Gamma] \ , \tag{4.3}$$

$$\Gamma = \frac{2}{1-B/A}\left[\frac{A-1}{(1-B/A)^2}\frac{B}{A} ln\left(\frac{A}{B}\right) - \frac{B-1}{1-B/A} - \frac{B+1}{2}\right], \tag{4.4}$$

where $A = \lambda_s / \lambda_g$, $B = 1.25\left(\varepsilon_s/\varepsilon_g\right)^{10/9}$, $\omega = 7.26\, e^{-3}$,

λ_s and λ_g are the thermal conductivities of particles and gas, respectively.

4.2.2 Model Setup

Research on the heat transfer coefficient of surface-bed in fluidized beds was carried out experimentally by Di Natale et al.[73, 205]. In their studies, probes with different shapes were immersed into the fluidized bed to investigate the heat exchange from the surface to the bed. In the present work, 2-dimensional (2-D) numerical geometries are set up according to the relevant geometrical and physical parameters used in the experiments. The height of the reactor was decreased from 1800 mm to 1200 mm in order to reduce the computational time of the simulation. However the bed height remained the same which was 600 mm. Spherical and cylindrical probes were positioned at a height of 300 mm in the experiments. For the 2-D model, the probes are simplified to circle (diameter 28mm)

and square (side length 30mm) heated surfaces in reactor I and reactor II, respectively, as shown in Figure 4.1.

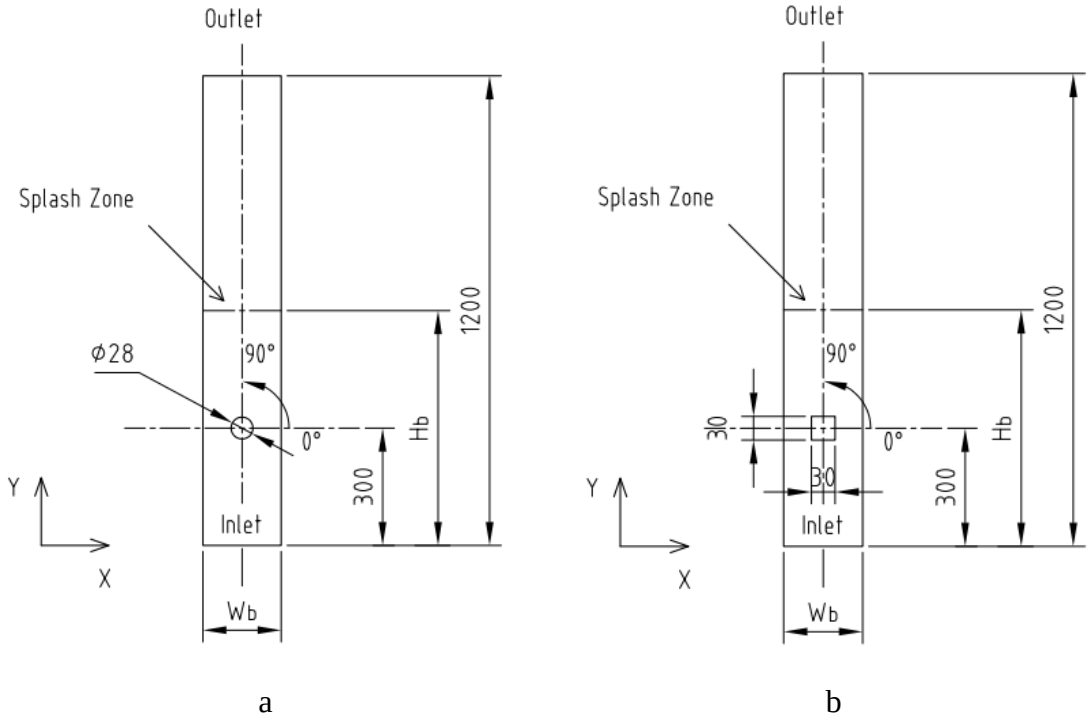

Figure 4.1 Geometries and direction & angular positions for data taken (Unit: mm)

(a) reactor I; (b) reactor II.

Glass beads with a uniform diameter of 0.5 mm were used as the fluidizing bed material which was fluidized by air from the bottom distributor. In the model, the superficial velocity of the fluidizing gas from inlet was set to 0.3 m/s uniformly, about $1.4u_{mf}$, from which bubbles can be obtained in the beds. The heated surfaces were given a constant temperature of 373 K whilst the bed had an initial temperature of 293 K. The reactor walls were defined with an adiabatic boundary condition. No-slip boundary conditions were defined for both gas and solid phases while the solid volume fraction within the bed was set to 0.6 initially. Details of the initial conditions and setting parameters used in the simulation are given in Table 4.1.

Table 4.1 Initial and boundary conditions

Property	Value	Unit
ρ_g	1.225	kg/m^3
ρ_s	2540	kg/m^3
u_{sf}	0.3	m/s
u_{mf}	0.22	m/s
μ_g	1.79e-5	kg/m-s
T_g	293	K
T_s	293	K
T_{tube}	373	K
Cp_g	994	J/kg-k
Cp_s	765	J/kg-k
K_g	0.0252	W/m-k
K_s	0.9	W/m-k
D_s	0.5	mm
$H_{b,ini}$	600	mm
W_b	100	mm
e	0.9	
β	0.6	
Inlet	Velocity inlet	
Outlet	Pressure outlet	
Walls	Adiabatic, No-slip for gas & solid phases	
Tube walls	Constant T=373K, No-slip for gas & solid phase	

For mesh generation, instead of the uniform subcell dimensions used by Syamlal *et al.* [206], the grid refinement technique proposed by Kuipers *et al*. [75] was employed to subdivide the region near the heated surfaces. In general, the division into 7 subcells can be considered to construct grid independence. Previous simulations of surface to bed heat transfer in fluidized beds, with similar particle sizes of 0.05 mm, applied this grid refinement technique in the direction normal to the heated wall [75-78, 207]. Comparable results between simulation and experiment were obtained thus demonstrating grid independence. In the present work, quadrilateral cells were used to mesh the general area of the reactor with a uniform cell size of 2 mm. The sizes of the cells in the near wall region of the heated surface varied from 0.02 mm to 2 mm with an increasing factor of 1.22 from the heated surface. The finest subdivision near the wall is used to obtain the local temperature gradients. The grid sizes are believed to be sufficient to achieve a grid independent solution.

A first-order upwind scheme was used for the discretization while Phase Coupled SIMPLE algorithm was employed for Pressure-Velocity Coupling. The relaxation factors were set with the default values. The time step size was 0.0001 s with fixed time stepping method during the calculation.

4.3 Results and Discussion

4.3.1 Flow Characteristics

Previous studies [75, 77, 80] showed that heat exchange in fluidized beds is a complicated process as the flow characteristics have direct influence on the wall-to-bed heat transfer. In the following section, the effects of the heated tube shapes on the bubbles motion and heat transfer processes are investigated in reactor I and II. Schmidt *et al.* [76, 207] carried out experimental work and they displayed the bubble distribution in the near region of the round tube. Figure 4.2 displays a blanketing effect of the bubbles from the present simulated results at 0.12 s within both reactors. The circle tube compares well with the

published images of a circle submersed tube of Schmidt *et al*. [76, 207]. The similar air bearing zone and detaching bubbles indicates that the expected flow pattern in fluidized beds can be captured successfully by the numerical methods. Meanwhile bubble formation in reactor I appears to travel around the tube faster as the square tube provides more resistance against the upward flowing gases.

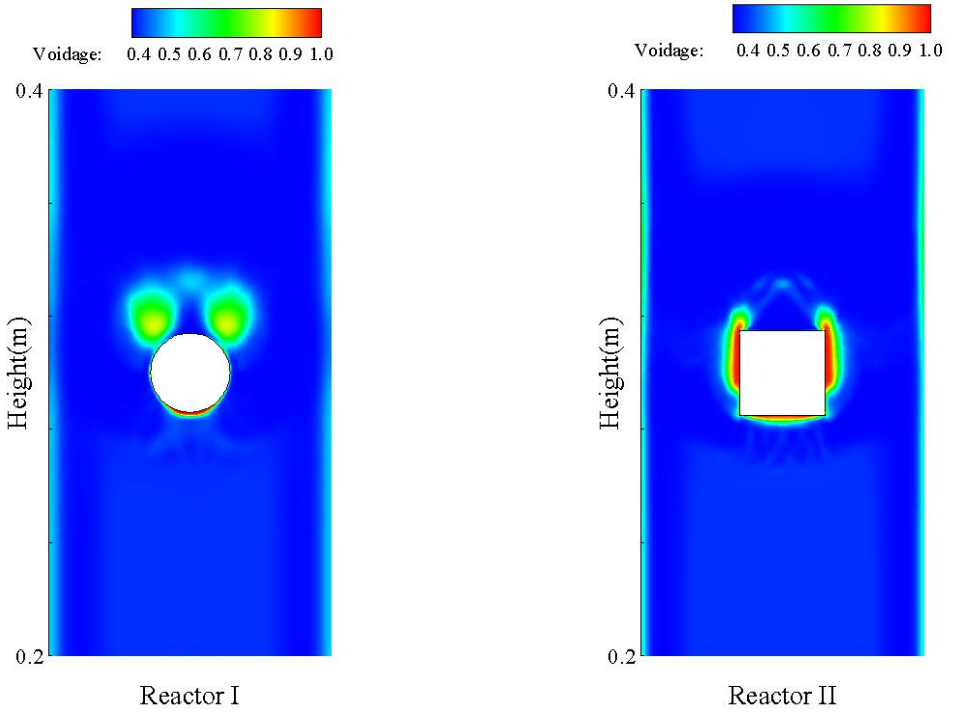

a b

Figure 4.2 Particle volume fraction in (a) reactor I and (b) reactor II at 0.12 s.

Figure 4.3 shows the bed height expansion of reactor I and II, under the same operating parameters and physical properties. As air is introduced at the beginning it disperses through the bed causing the bed height to rise to 0.6 m and 0.7m for reactor I and reactor II, respectively. The bed height then fluctuates for both reactors at a certain bed height. In both reactors, the curves for the bed height against time are performing the similar tendencies. In this process, two stages can be defined based on the activity of solids, a fluidizing and fluidized stage. In the fluidizing stage gas is introduced to the packed particles in bed and disperses whilst moving the particles upward with the flow. Once the

particles obtain momentum from interactions with the gas and exchange momentum by collisions the bed enters the fluidized stage. It is at this fluidized stage that the bed will stay in a relatively stable status, and the height of bed varies according to bubbles coalescence and eruption.

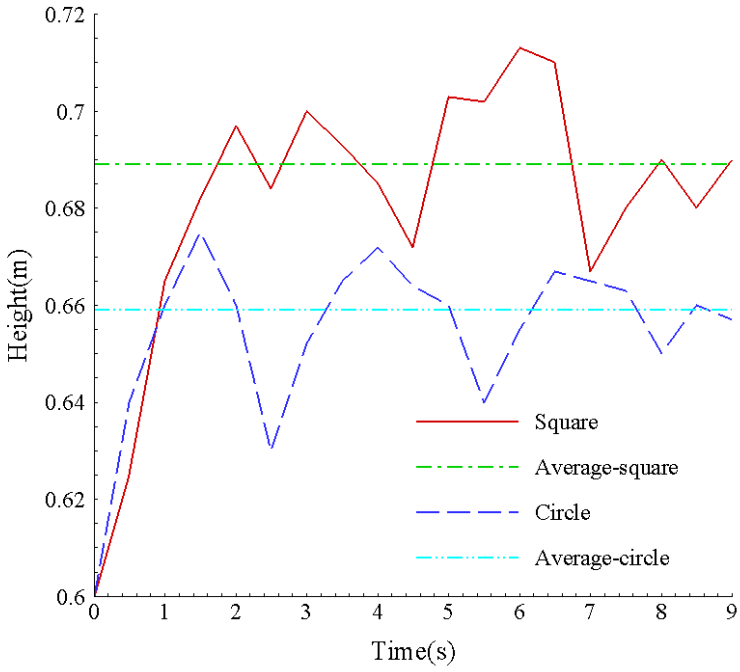

Figure 4.3 The bed expansion in reactor I and reactor II.

Although the curves for reactor I and II in Figure 4.3 show the similar fluctuating tendency, the difference can be addressed obviously. Reactor I appears to reach fluidization faster than reactor II. It takes 1.00 s to reach the average height of the bed in the fluidization stage which is approximately 0.66 m. Reactor II takes almost 2.00s to expand to its average height of around 0.69 m. The difference can be attributed to the effects of the different shapes of the immersed tubes on the particles motion. As the obstacles are located in the centre of reactors, circulation of solids is disrupted partially as particles move around the immersed surfaces.

Figure 4.4 shows the particles in reactor I, move around the circular surface smoothly. Low velocity regions form below the tube due to the flow being restricted by the presence of the tube. The other low-velocity region is present at the top of the tube as the flow separates from the tube and traverses around this region. In reactor II, the horizontal base of square surface is much flatter and occupies almost 30% of the reactor diameter. The low velocity zone beneath the square surface is much larger than that in reactor I as shown in Figure 4.4(b), and similarly for the zone above the tube. This is because the flat base obstructs the flow causing the air to accumulate in the form of larger bubbles below the surface. The velocity is high around the sides of the tubes because the particles and gas tries to avoid the obstruction by assembling together at either side of the tube to continue travelling up in the bed. The tube presence prohibits the development of a fluidized flow structure in the lower region of the bed.

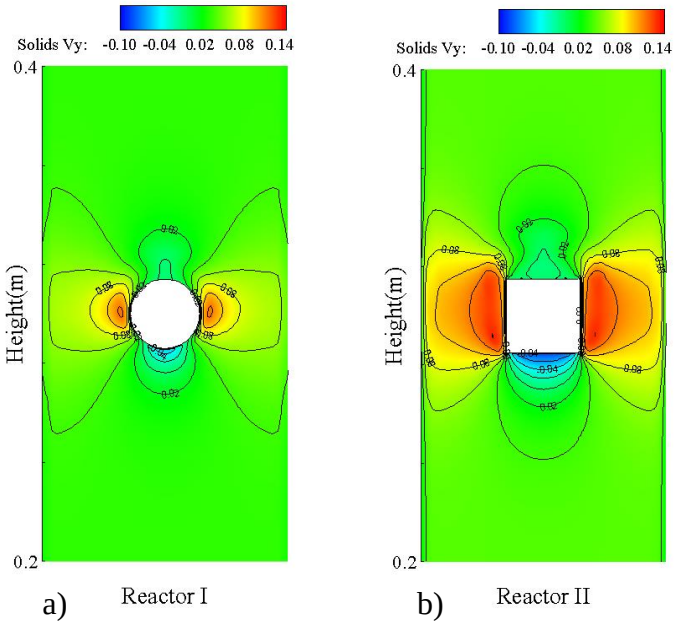

Figure 4.4 Distribution of particles Y velocity around the tubes in a) reactor I and b) reactor II.

Figure 4.5 shows the velocity distribution of the solids at reactor heights 0.15 m and 0.45 m at 0.50 s, 1.00 s, 5.00 s, 7.00 s and 10.00 s. At 0.50 s, the solid particles move almost

with a uniform velocity distribution across the reactor at heights 0.15 m and 0.45 m in reactors I and II. This is because the bed is not yet fluidized. However at 1.00 s, this tendency is only maintained at 0.15m in reactor II which indicates the square surface greatly influences the particle motion in the lower section of reactor II. After 5.00 s, when solid particles are fully fluidized in reactor, all curves for both reactor I and II display a fluctuating velocity distribution, which is due to the bed reaching fluidization and the motion of bubbles through the bed affecting the local particle velocities.

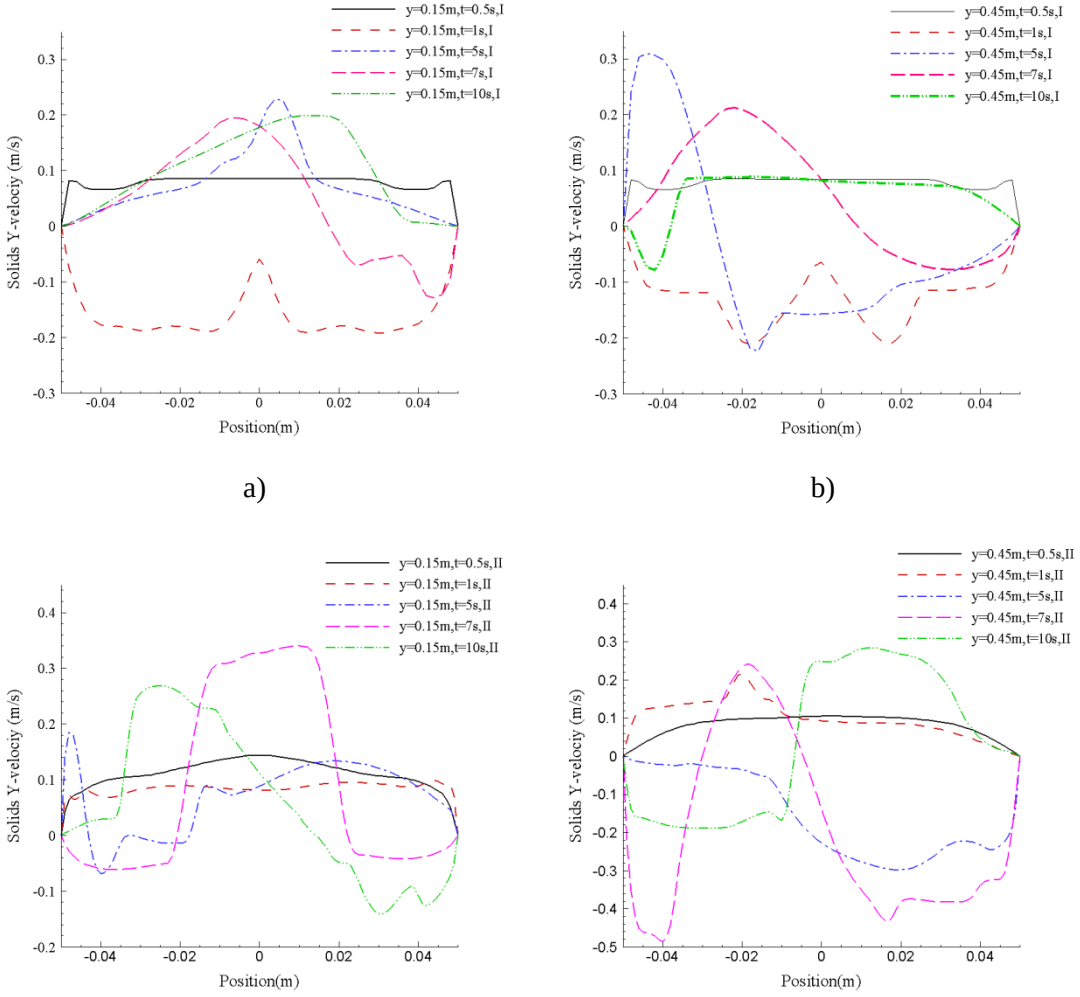

Figure 4.5 Distribution of y-velocity on different levels and time in reactor I (a,b) and II (c,d).

Figure 4.6 compares the solid volume fraction in both reactors after 5.00 s. The bubbles in reactor II are bigger than those in reactor I. Reactor II leads to a dramatic change in the

cross section of the reactor. The ascending bubbles coalesce under the tube to form larger bubbles than those collecting at the base of the circular tube. This leads to larger bubbles moving around the tube which continues to coalesce with height. It is these larger bubbles that are responsible for the larger increase in bed height shown in Figure 4.3.

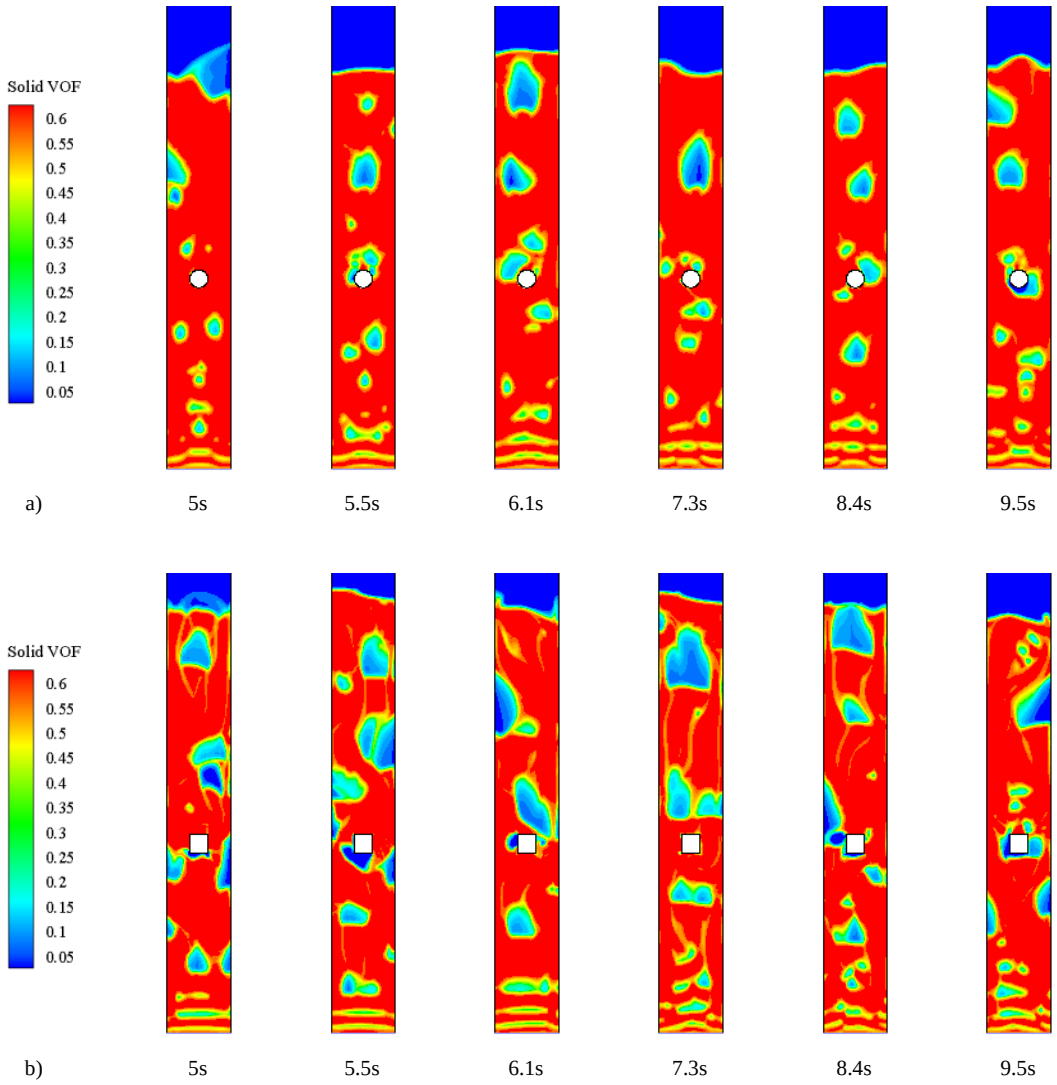

Figure 4.6 Contour plot of volume fraction of sand during fluidization of a) reactor I and b) reactor II.

4.3.2 Heat Transfer from Surface to Bed

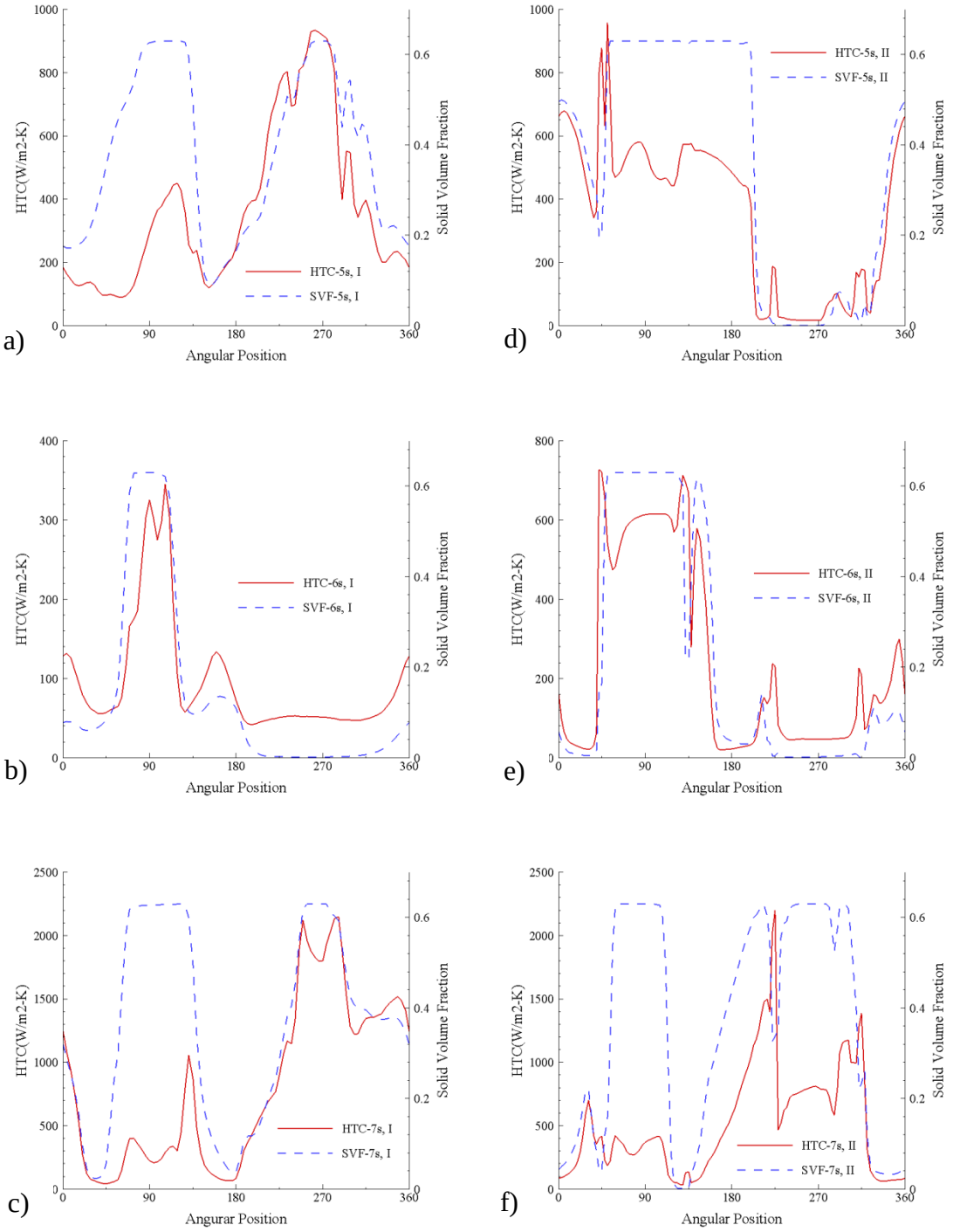

Figure 4.7 Local instantaneous HTC and SVF around the tube surface:

(a,b,c) reactor I; (d,e,f)reactor II.

The studies of Schmidt *et al*. [76, 207] showed that particles adjacent to the tube play the major role in the estimation of heat transfer coefficient. Figure 4.7 shows the distribution of local instantaneous heat transfer coefficients, calculated by Equation 4.1, and local volume fraction of solid phase. In reactor I, air accumulates at the base of the circle tube to form bubbles and detach. Due to the formation and the heterogeneous flow of the bubbles around the tube, the distributions of the voidage and the local heat transfer coefficient vary with time. At 5, 6 and 7 s, the top of the heated surface (45^0 - 135^0) displays a voidage less than 0.4 and an average local heat transfer coefficient about 350 W/m^2K. The magnitude of the local heat transfer changes significantly between the different time intervals with peak values at 5s at approximately 900 W/m^2K and at 7s values of 2200 W/m^2K.

In reactor II, similar trend is observed as that in reactor I, where an increase in volume fraction usually leads to an increase in heat transfer coefficient. It can also be seen that similar volume fractions display different heat transfer coefficients. For example, at 5.00 s in Figure 4.7a, the voidage at the 135^0 and 270^0 are almost the same (about 0.4), but the local heat transfer coefficient at the two positions are 450 W/m^2K and 910 W/m^2K, respectively. Generally, at the top side of heated surface, near 90^0, the voidage keeps in a constant value about 0.4 as the bubbles do not encase the whole heated surface but detach to continue up the bed. This was observed experimentally by Schmidt *et al.* [76] and numerically by Armstrong *et al*. [77]. In particle built up regions the heat transfer coefficient varies only slightly. The transition regions between particle dense and dilute regions show the greatest variation in heat transfer coefficient due to the enhanced mixing of the heated particles and the introduction of cool particles, which was also shown by Armstrong *et al*. [77].

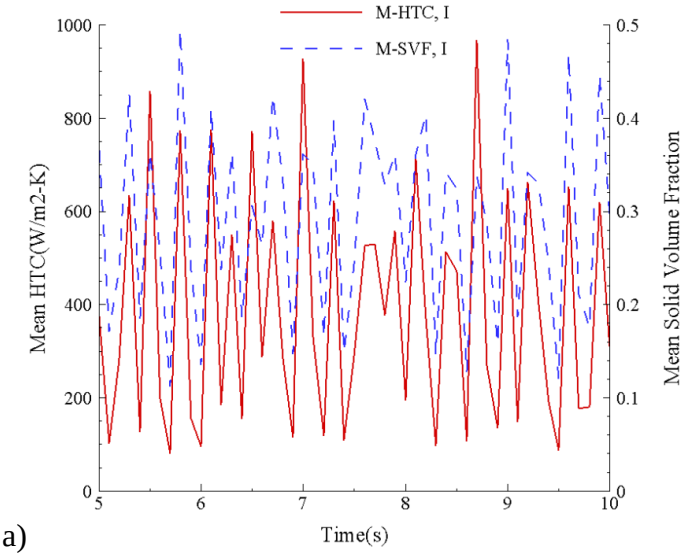

a)

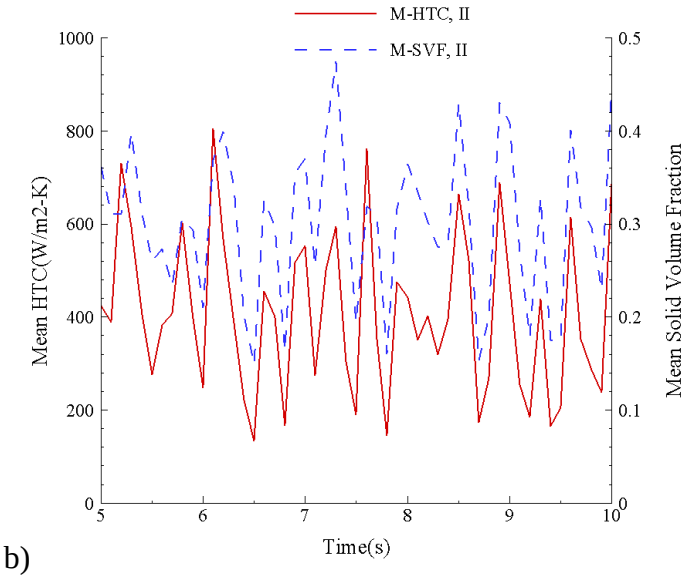

b)

Figure 4.8 M-HTC and M-SVF around the tube surface during fluidization:

(a) reactor I ; (b) reactor II.

Figure 4.8 shows the mean heat transfer coefficients of the heated surface and the mean solid volume fraction around the complete tube (360^0) between 5 and 10 s. Since the variation in tube shape greatly influences the flow dynamics it is clear that this greatly affects the mean volume fraction of solid phase (M-SVF) and subsequently mean heat

transfer coefficient (M-HTC). Reactor I displays a higher fluctuating frequency than reactor II, and the M-HTC follows the similar trend.

In the studies of F. Di Natale [73], the averaged maximum surface-to-bed heat transfer coefficients from experimental work were 260 W/m^{2}K and 230 W/m^{2}K for reactor I and reactor II, respectively. The simulated results, with the same geometries and physical properties, are about 380 W/m^{2}K and 401 W/m^{2}K. This over prediction could be due to the effective thermal conductivity correlations which are using the actual gas volume fraction. In wall-to-bed simulations, a porosity model is used to account for the gas pockets between the particles but a correlation currently does not exist, to the authors' knowledge, for a reactor with submersed tube the bubble dynamics around the tube are very unpredictable.

4.4 Conclusions

In this chapter, two different shaped heated tubes are used to investigate their effects on the hydrodynamics in the bed and the surface-to-bed heat transfer. A square heated tube influences the hydrodynamics more than the circular tube which delays the bed from reaching fluidization. The flatter base of the tube obstructs the flow more which leads to a larger build-up of air below the tube thus forming larger coalescing bubbles and subsequently increasing the bed expansion. The distribution of local instantaneous heat transfer coefficients is regarded to be highly sensitive to the hydrodynamics of the bed. The time-mean values of heat transfer coefficients calculated by the effective thermal conductivity is still over-predicted compared to the experimental work. More detailed models which consider the porosity around a tube would improve the accuracy of the numerical models.

Chapter 5: Mixing and Segregation

5.1 Introduction

The properties of solids greatly influence the fluidization, thermochemical processes and final products through complicated gas-solid and solid-solid interactions. In industrial processes, the bed materials have a broad range of sizes or even different densities (when two or more different bed materials are used). The differentiation of the solid particles could give rise to segregation of solid particles during the mixing in fluidization. A number of expressions of mixing index (M) have been proposed to quantify the degree of mixing for binary mixtures. Lacey [208] introduced a well-known Lacy index based on statistical analysis. Rowen *et al.* [209, 210] proposed a new solid mixing index, $M = X/\bar{X} * 100\%$, where X is the fraction of jetsam (large/ heavy particles) in the top section of the bed or the fraction of flotsam(small/light particles) in the lower half and $\bar{X}$ is the average fraction of jetsam/flotsam for the whole bed. When M is equal to 0, it indicates the state of complete segregation meanwhile $M = 1$ means perfect mixing. The larger M corresponds to the better mixing state. The Rowen's mixing index is used here to quantify the mixing degree.

5.2 CFD Model

Computational Fluid Dynamics (CFD) simulation has become an important tool to improve the performance of fluidized beds for academic and industrial research. The models can reveal dynamic details of multiphase flow interaction inaccessible from experiments. A CFD model based on Eulerian approaches is used here to study the mixing-segregation with binary mixtures in fluidized beds.

5.2.1 Model Setup

Two-Fluid Model (TFM) has been employed to describe the hydrodynamics of fluidized beds together with Kinetics Theory of Granular Flow (KTGF). The gas and solid phases are treated as interpenetrating continuua with individual volume fractions. The

characteristics of particles such as collision and fluctuating motion are expressed by solid viscosity, solid pressure and granular temperature. The interactions between phases are considered as drag coefficient for momentum exchange. The TFM-KTGF method is used to solve interactions between one gas phase and two solid phases (s1 and s2) in the fluidization. According to the continuum assumption of particles in beds, all phases of gas and solids follow the same rules of balance of mass, momentum and energy. Gas-solid interphase interactions are solved with the drag function by Gidaspow *et al.* [60], while solid-solid interactions are treated by the interphase exchange coefficient by Syamlal [211]. Hence the momentum exchange between solid phases is considered in terms of particle size, the radial distribution coefficient, *etc*. The relevant governing and constitutive equations are given in Chapter 3 and Table 5.1.

Table 5.1 Constitutive equations

Solid-Solid Exchange Coefficient

Syamlal model [211] (s1: solid phase 1; s2: solid phase 2)

$$K_{s1,s2} = \frac{3(1+e_{s1,s2})\left(\frac{\pi}{2}+C_{fr,s1,s2}\frac{\pi^2}{8}\right)\rho_{s1}\varepsilon_{s1}\rho_{s2}\varepsilon_{s2}(d_{s1}+d_{s2})^2 g_{0,ls}}{2\pi(\rho_{s1}d_{s1}^3+\rho_{s2}d_{s2}^3)}|\vec{v}_{s1}-\vec{v}_{s2}| \quad 5.1$$

Radial distribution function

Lun *et al.* model [199]

$$g_{0,sisi} = \left[1-\left(\frac{\varepsilon_s}{\varepsilon_{s.max}}\right)^{\frac{1}{3}}\right]^{-1} + \frac{1}{2}d_{si}\left(\frac{\varepsilon_{s1}}{d_{s1}}+\frac{\varepsilon_{s2}}{d_{s2}}\right), \quad i\text{=1 or 2} \quad 5.2$$

$$\varepsilon_s = \varepsilon_{s1}+\varepsilon_{s2} \quad 5.3$$

$$g_{0,s1s2} = \frac{d_l g_{0,s1s1}+d_s g_{0,s2s2}}{d_{s1}+d_{s2}} \quad 5.4$$

Syamlal-O'brien model [198]

$$g_{0,s1s2} = \frac{1}{1-\varepsilon_s} + \frac{3\left(\frac{\varepsilon_{s1}}{d_{s1}}+\frac{\varepsilon_{s2}}{d_{s2}}\right)}{(1-\varepsilon_s)^2(d_{s1}+d_{s2})}d_{s1}d_{s2} \quad 5.5$$

5.2.2 Domain Setup

As shown in Figure 5.1, the 2-D reactor model is set up based on the experiment rig used by Wu *et al.* [124], with the diameter of 300 mm and the height of 1550 mm. Binary materials at different sizes or densities are packed at the height of 360 mm initially in beds with the packing rate of 0.6 and the bed aspect ratio, H_{bed}/D, is equal to 1.2. The effect of bed aspect ratio on mixing-segregation can be neglected here however the effect will become substantial when the ratio is less than 0.8 [124]. In the current study, fluidization of particles at different sizes or densities is simulated to investigate the mixing-segregation behaviour.

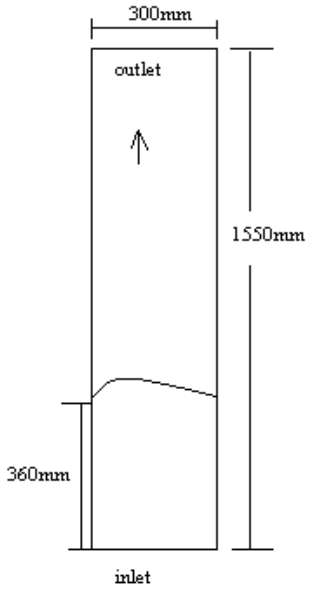

Figure 5.1 Geometry of fluidized bed reactor in 2-D.

Several cases are set up and the details of bed mixtures are given in Tables 5.2-5.4. In Cases m1 to m5, the grid independence is discussed. The domain is meshed in the different grid sizes at 2, 3, 4, 6, 8mm. Cases r1, e1-e4 and v1-v8 are set up to specify the influence from the radial distribution function (g_0), the coefficient of restitution (e_{ss}) and the superficial velocity, where the solids are classified by different densities with equal diameter. The behaviour of particles with different sizes at the same density is investigated in Cases s1-s11, where the mixing is examined by different *e* and gas

superficial velocities. The fluidising gas (air) is injected uniformly from the bottom distributor at a velocity range of 0.1-0.5 m/s, which is several times higher than the minimum fluidization velocities of the small or light solids, namely flotsam.

Table 5.2 Case details for grid independence

Cases	Grid size (mm)	Diameter (mm)	Density (kg/m3)			Superficial velocity (m/s)	Minimum fluidization velocity (m/s) [124]	
			Jetsam	Flotsam	ratio		jetsam	flotsam
m1	2	0.47	2600	1100	2.36:1	0.2	0.13	0.06
m2	3	0.47	2600	1100	2.36:1	0.2	0.13	0.06
m3	4	0.47	2600	1100	2.36:1	0.2	0.13	0.06
m4	6	0.47	2600	1100	2.36:1	0.2	0.13	0.06
m5	8	0.47	2600	1100	2.36:1	0.2	0.13	0.06

Table 5.3 Case details for density difference

Cases	Grid size (mm)	g_0	e	Diameter (mm)	Density(kg/m3)			Superficial velocity (m/s)
					Jetsam	Flotsam	ratio	
e1	3	LM	0.93	0.47	2600	1100	2.36:1	0.2
e2	3	LM	0.95	0.47	2600	1100	2.36:1	0.2
e3	3	LM	0.97	0.47	2600	1100	2.36:1	0.2
e4	3	LM	0.99	0.47	2600	1100	2.36:1	0.2
v1	3	LM	0.9	0.47	2600	1100	2.36:1	0.16
v2	3	LM	0.9	0.47	2600	1100	2.36:1	0.18
v3	3	LM	0.9	0.47	2600	1100	2.36:1	0.20
v4	3	LM	0.9	0.47	2600	1100	2.36:1	0.22
v5	3	LM	0.9	0.47	2600	1100	2.36:1	0.24
v6	3	LM	0.9	0.47	2600	1100	2.36:1	0.26
v7	3	LM	0.9	0.47	2600	1100	2.36:1	0.28
v8	3	LM	0.9	0.47	2600	1100	2.36:1	0.30
r1	3	SM	0.9	0.47	2600	1100	2.36:1	0.20

Table 5.4 Case details for size difference

Cases	Grid size (mm)	*e*	Density (kg/m3)	Diameter (mm)			Superficial velocity (m/s)	Minimum fluidization velocity (m/s) [124]	
				Jetsam	Flotsam	ratio		Jetsam	Flotsam
s1	3	0.9/0.9/0.9	2600	0.7	0.28	2.5:1	0.1	0.145	0.064
s2	3	0.93/0.93/0.93	2600	0.7	0.28	2.5:1	0.1	0.145	0.064
s3	3	0.95/0.95/0.95	2600	0.7	0.28	2.5:1	0.1	0.145	0.064
s4	3	0.97/0.97/0.97	2600	0.7	0.28	2.5:1	0.1	0.145	0.064
s5	3	0.99/0.99/0.99	2600	0.7	0.28	2.5:1	0.1	0.145	0.064
s6	3	0.9/0.99/0.9	2600	0.7	0.28	2.5:1	0.1	0.145	0.064
s7	3	0.99/0.9/0.99	2600	0.7	0.28	2.5:1	0.1	0.145	0.064
s8	3	0.9/0.9/0.9	2600	1.1	0.3	3.14:1	0.1	0.32	0.064
s9	3	0.9/0.9/0.9	2600	1.1	0.3	3.14:1	0.2	0.32	0.064
s10	3	0.9/0.9/0.9	2600	1.1	0.3	3.14:1	0.3	0.32	0.064
s11	3	0.9/0.9/0.9	2600	1.1	0.3	3.14:1	0.4	0.32	0.064

5.2.3 Grid independence

Grid dependent tests were carried out by using grid sized of 2, 3, 4, 6 and 8 mm. Their influences on the hydrodynamics and mixing are examined by two factors: bed height and mixing index. Figure 5.2 shows the curves of bed height and mixing index with different grid sizes. The relevant values are compared in time range of 20 to 50 s when the full fluidization state is achieved. No large variation which can be observed from the curves for bed heights in different cases. The corresponding time-mean bed heights at 0.454, 0.449, 0.445, 0.451 and 0.444 m also indicate the ignorable effect on average distribution of voidage in fluidized beds with the grid sizes in current range. In contrast to the results conducted from bed height comparison, the curves for mixing index show that the mixing-segregation processes are varied clearly until the grid size is smaller than 4 mm. The smallest mixing index is delivered by 6mm mesh and the biggest one from grid size at 8mm. The comparable values of mixing index are given at grid size in range of 2-4 mm. The results obtained from Figure 5.2 indicate that both the hydrodynamics and mixing-segregation phenomena can be well captured with the grid size smaller than 4 mm, which is consistent with the previous finding by Ming *et al.* [212]. By considering grid

independence together with the computational efficiency, the grid sizes less than 4 mm are used throughout this result session.

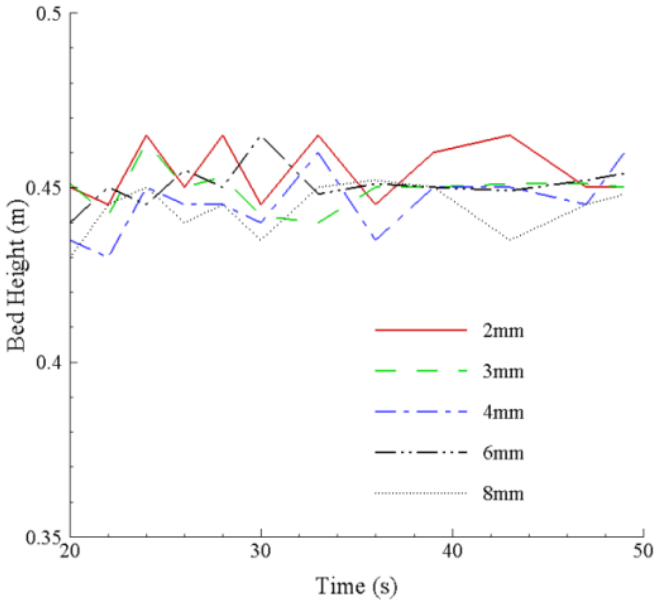

a

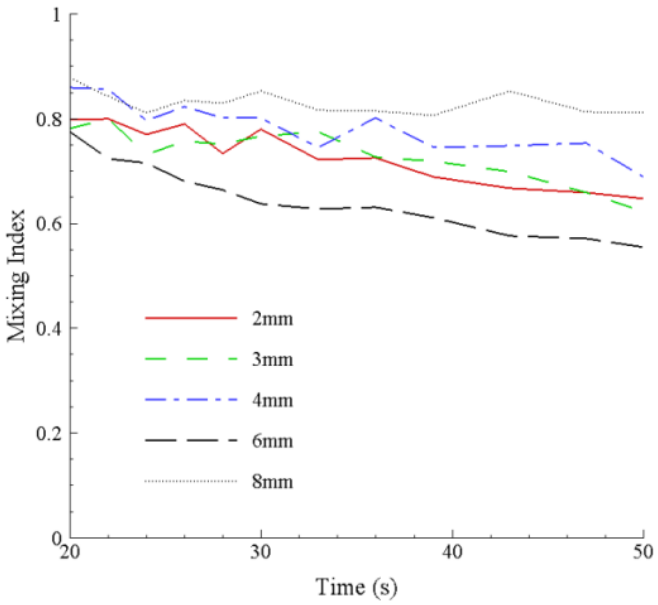

b

Figure 5.2 Volume distribution (a) and mixing index (b) by grid sized in 2,4,6 and 8mm.

5.2.4 Numerical strategy

The flow pattern of multiphase flow was represented by solving the relevant governing and constitutive equations. The method of discretization was executed by the first-order upwind scheme with the SIMPLE algorithm for Pressure-Velocity coupling. The multiphase interactions were considered by the constitutive model for granular phase. No-slip and free-slip boundary conditions were defined for the solid phases in Cases m3 and v3. The relevant results indicated the insignificant influence on the bed height and the mixing process as shown in Figure 5.3. The computational time step size was given by 0.0001s with fixed time stepping method. A brief setting of relevant parameters is given in Table 5.5. In data post-processing, all the values before 20s were abandoned to ignore the effects from the fluidization in start stage.

Table 5.5 Initial parameters and boundary conditions

Property	Value	Unit
ρ_g	1.225	kg/m^3
T_g	293	K
T_{s1}	293	K
T_{s2}	293	K
H_{rea}	1550	mm
W_{rea}	300	mm
$H_{bed,ini}$	360	mm
Inlet	Velocity inlet	
Outlet	Pressure outlet	
Walls	No-slip for gas	

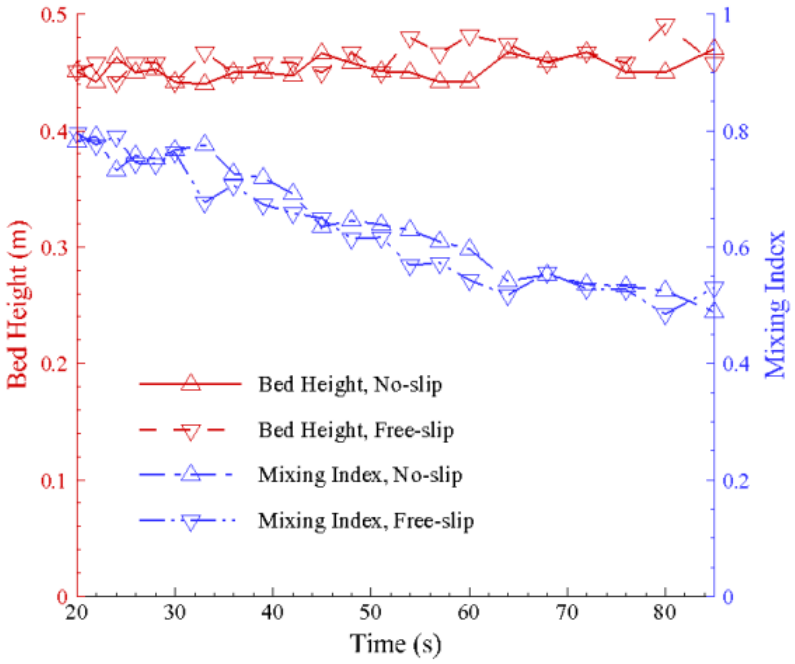

Figure 5.3 Effects of boundary conditions on bed height and mixing index.

5.3 Results and Discussion

The mixing process in a binary bed system during the fluidization is complicated with the simultaneous occurring of segregation. The mixing-segregation is jointly affected by operational conditions and solid properties as discussed below.

5.3.1 Cases of Difference in Density

Effect of coefficient of restitution

The coefficient of restitution represents the consumption or generation of kinetic energy in a collision of a pair of objects. In the elastic collision, it is equal to 1 which defines no energy dissipation. In realistic conditions, the value of the coefficient of restitution is adjusted for different particle types. In the current work, the coefficient of restitution was given in range of 0.9 to 0.99 as displayed in Table 5.3. Figure 5.4(a) shows the curves for the bed heights from 20 to 86s in Cases e1-e4 and v3, which are fluctuating in the same region. The time-mean values for the bed heights correspondingly are close to 0.461 m besides that of Case e4 which is 0.465.

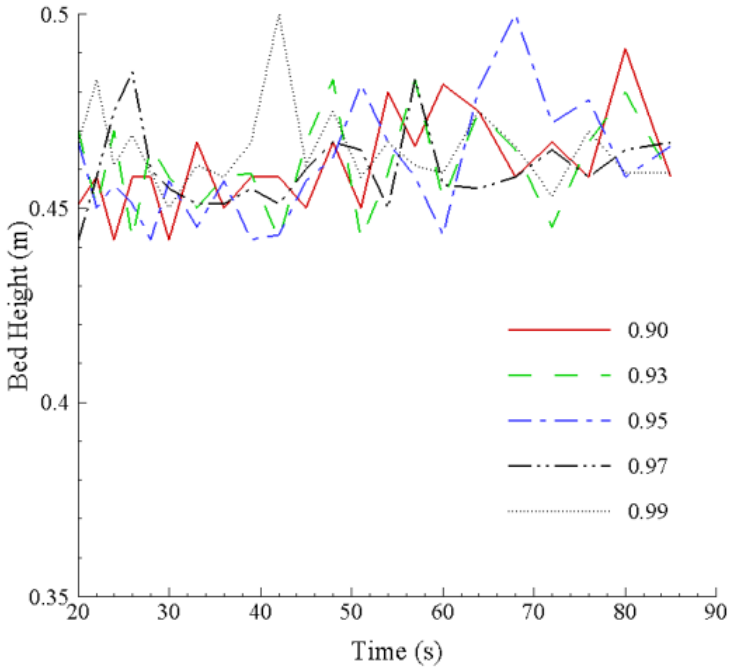

a

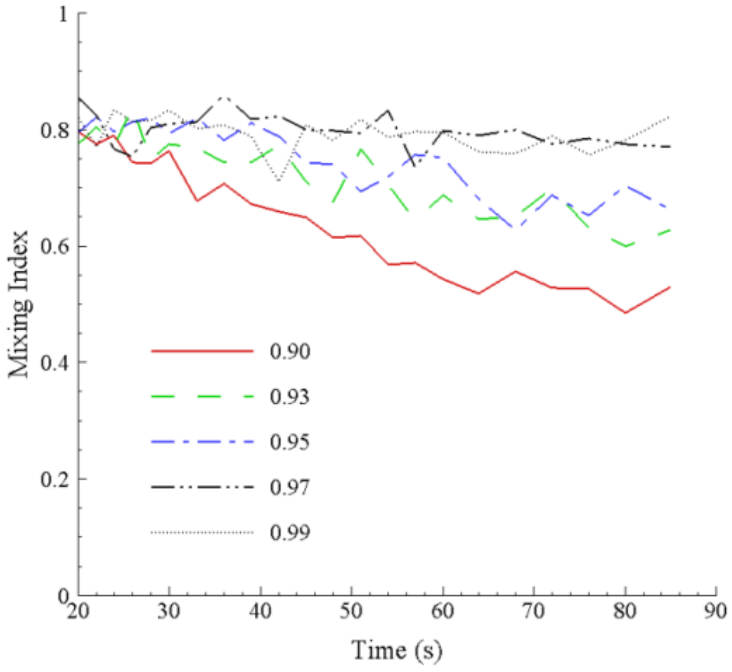

b

Figure 5.4 Effects of coefficient of restitution on bed height (a)and mixing index(b).

The results reveal that the effect of value option can be nearly neglected on predicting the mean voidage distribution when coefficient of restitution is in range of 0.9-0.99. The highest bed expansion in Case e4 can be attributed to the biggest given value of coefficient of restitution which defines the minimal energy dissipation in collisions. The tendency can be supported by Sinclair and Jackson [213] who pointed out the drastic structure changing as *e* is close to 1. In Figure 5.4(b), the mixing index values differ with the increasing coefficient of restitution obviously. Higher mixing index is delivered by the bigger coefficient of restitution which indicates the less energy dissipation leads to a better mixing of binary material. In other words, it can be deduced that the segregation process can be enhanced by more energy consumption in particles collisions.

Effect of radial distribution function

The radial distribution function described as a nondimensional distance between objects is a correction factor to modify the collision probability in dense solid granular phase. A number of formulations listed in literature can be introduced for it [214]. Two radial distribution functions, Lun *et al.* model (Case v3) and Syamlal-O'brien model (Case r1), were employed here and the results were compared in Figure 5.5 After 20 s, the bed heights delivered by applying the two functions distribute in a narrow area. The time-mean height for Syamlal-Obrien model is 0.462 m which is very close to the height of 0.461 m from Lun *et al*. model. Although the mixing index of Lun *et al.* model is much higher than that of Syamlal-Obrien model at 20s, it declines quickly and reaches the same level after 60s. The different tendencies indicate that the balance of mixing-segregation achieves earlier by applying Syamlal-Obrien model however the values of mixing index in stable status are almost the same. According to the comparison of the results from implementation of the two different functions, it concludes that applying different radial distribution functions barely influences the flow pattern in binary materials fluidization. On the other hand, the consistent results from two different functions also give a proof on the model reliability for the present cases.

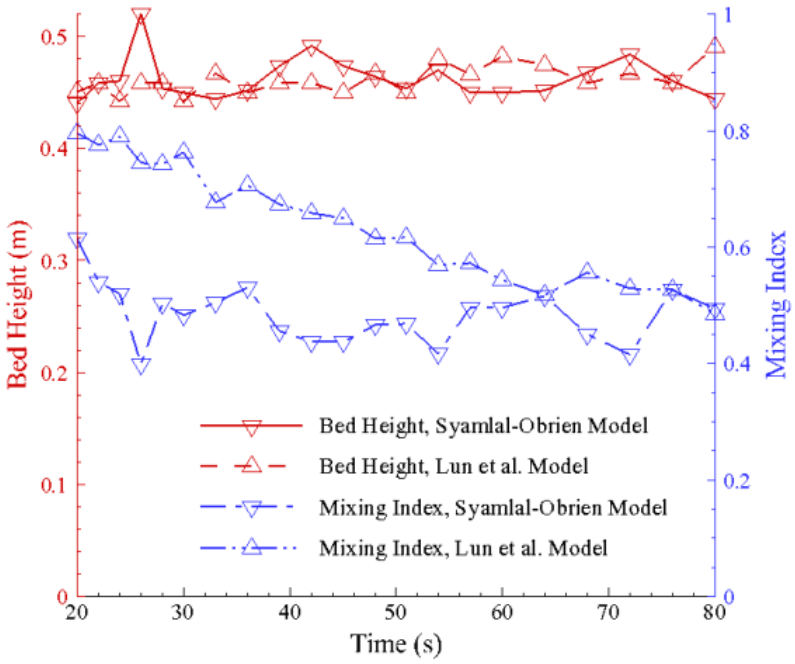

Figure 5.5 Effects of radial distribution function on bed height and mixing index.

Effect of superficial velocity

The superficial velocity governs the fluidization processes of the solid granular phases together with some physical characteristics of particles such as density, size, shape *etc*. In the current work, the gas with superficial velocities in range of 0.16 to 0.3 m/s was injected from the bottom inlet of the reactor to address the influence on hydrodynamics of the fluidized beds. Figure 5.6(a, c) shows the varying tendency of the bed heights and the mixing indexes from 20 to 70s while the time-mean bed heights are given in Figure 5.6(b). In general, the bed heights increase following the gradually enlarged gas velocity which means the bubbles grow up to bigger size. However, the well segregation can only be obtained when the superficial velocity is smaller than 0.24 m/s. When more fluidising gas blows into the reactor, the mixing index stays at the high level around 0.8 which can be considered as the well mixing status.

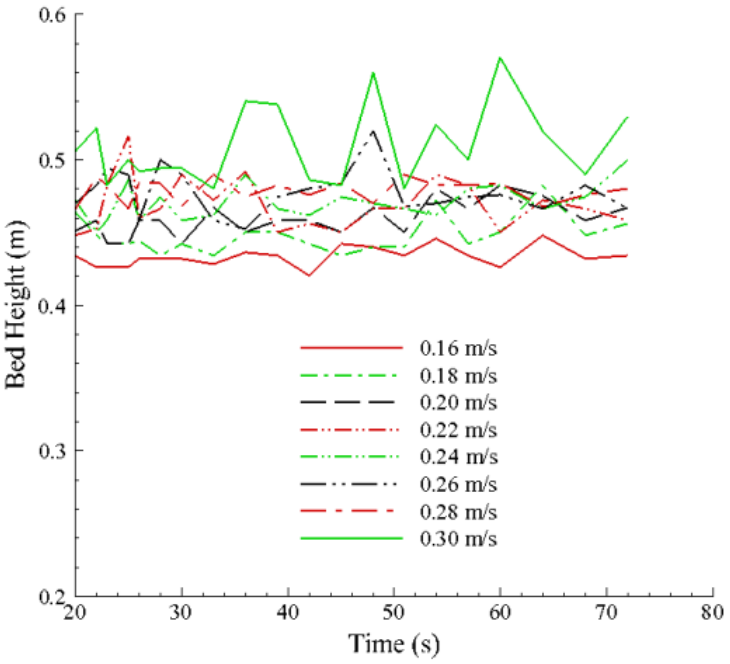
Bed Height (m)
Time (s)
0.16 m/s
0.18 m/s
0.20 m/s
0.22 m/s
0.24 m/s
0.26 m/s
0.28 m/s
0.30 m/s

a

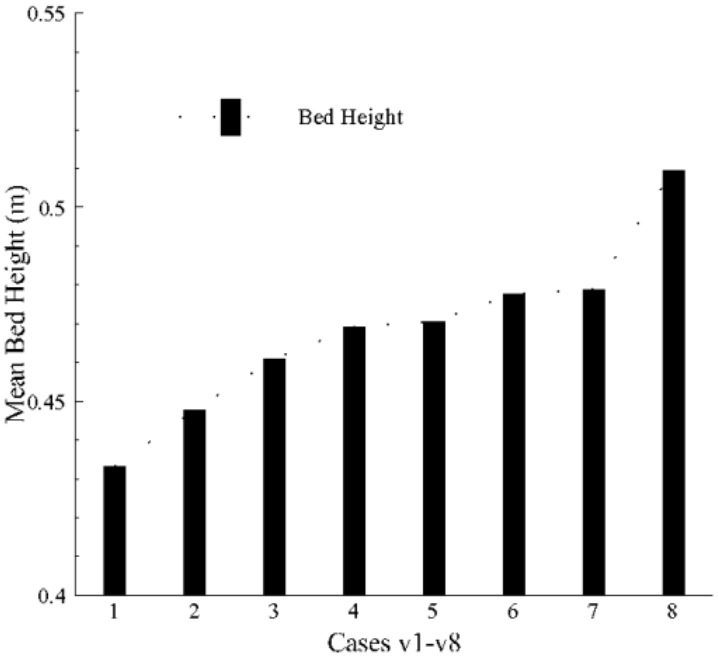
Mean Bed Height (m)
Bed Height
Cases v1-v8

b

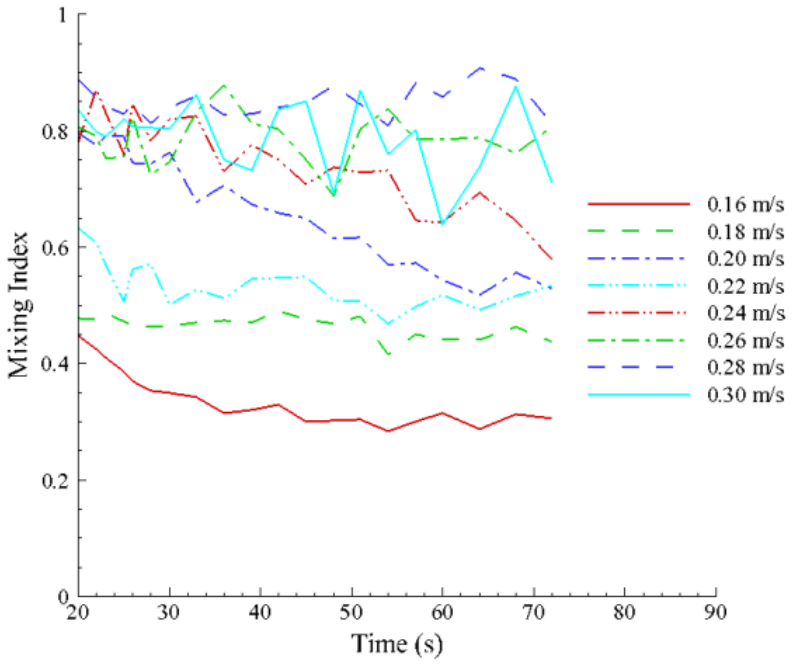

c

Figure 5.6 Effects of superficial velocity on bed height (a,b) and mixing index(c).

The relevant results are able to deduce that the separation of binary materials cannot easily proceed even the bigger bubbles exist during the mixing-segregation processes. In these conditions, the segregation progresses by bubbles cannot prohibit the mixing behaviour during the solid particles' moving. This phenomenon was reported by Kunii and Levenspiel [183] who confirmed that the segregation was only occurring within a certain range of superficial velocity for binary mixtures and was absent at strong bubbling fluidization.

Validation

Kunii and Levenspiel [183] examined the mixing-segregation phenomena of binary materials with different densities in fluidized beds. An ideal pattern of segregation was proposed based on experiments with commercial particles. Although it is not possible to perform a direct comparison quantitatively due to the difference in operating conditions

and composition of mixtures, the simulation results show the similar trend for the jetsam distribution with the idealized segregation pattern in Kunii and Levenspiel's work as shown in Figure 5.7. The low concentration of jetsam in upper region and the rich jetsam layer at bottom can be well matched.

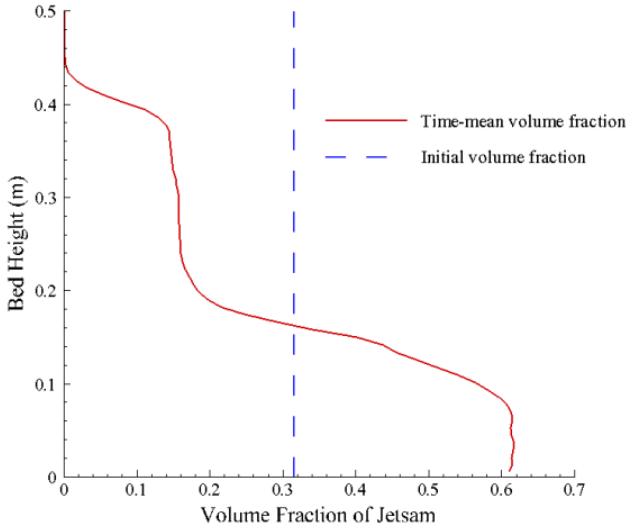

a

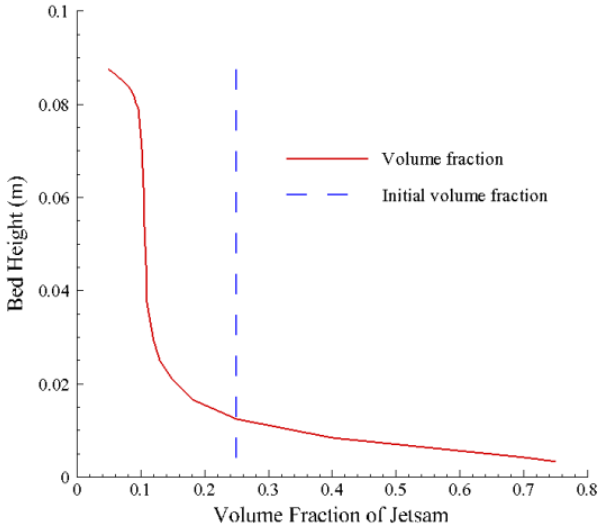

b

Figure 5.7 Comparison of Case v2 (a) with Kunii and Levenspiel parttern (b).

5.3.2 Cases of Difference in Diameter

Effect of coefficient of restitution

The Case studies on the segregation by size difference were based on the experiments by Wu and Baeyens [124] as shown in Table 5.4. Two groups of particles of Geldart group B were introduced into the simulations to investigate the mixing-segregation phenomena.

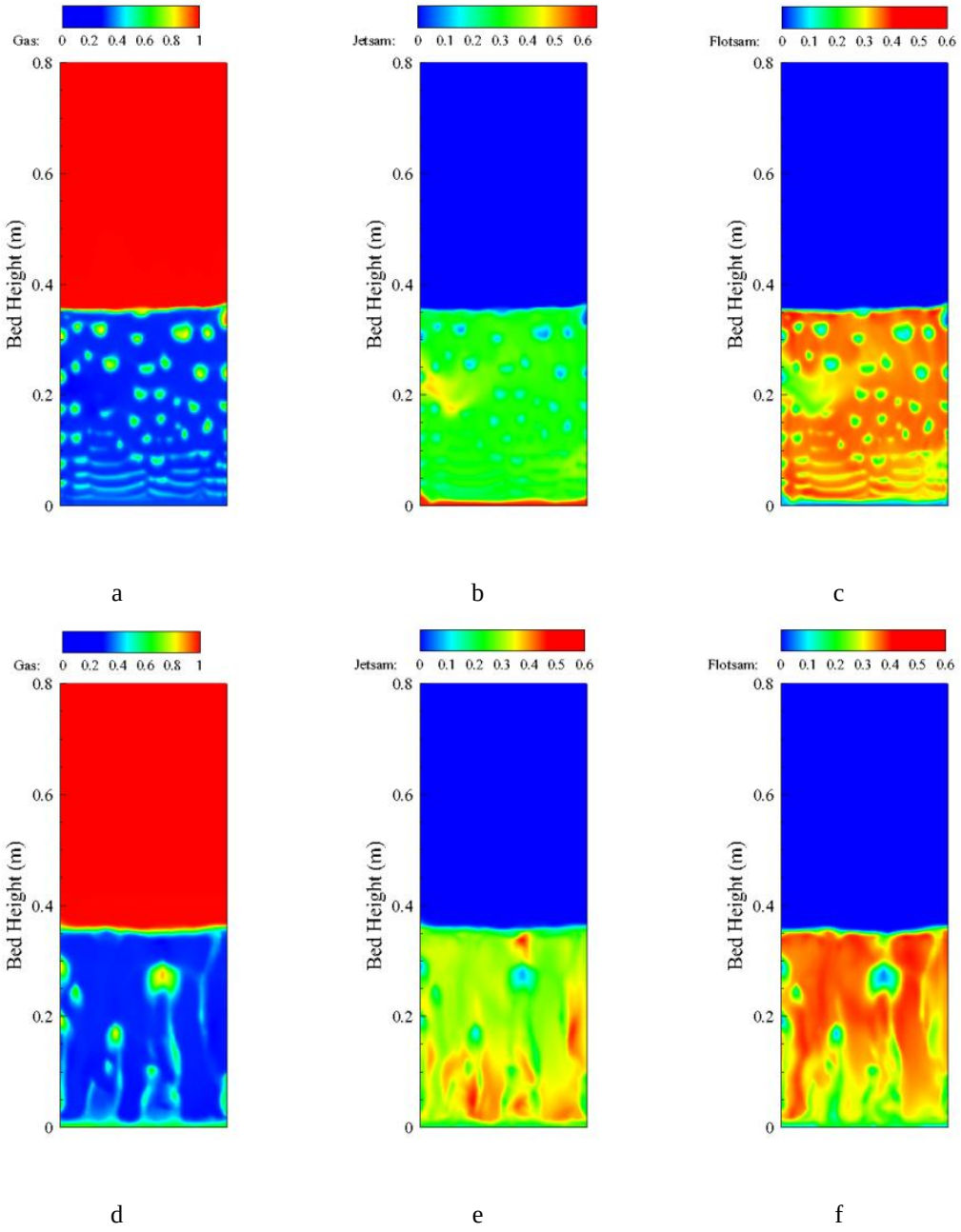

Figure 5.8 Volume distributions of gas (a,d), jetsam(b,e) and flotsam(c,f) with *e* of 0.9 and 0.99.

The volume fraction distributions of gas and solid phases at 50 s in Cases s1 and s5 are demonstrated in Figure 5.8. As the minimum fluidization velocities of jetsam and flotsam are about 0.06 and 0.38 m/s respectively, the gas superficial velocity given at 0.1 m/s is close to the minimum fluidization velocity of the small particles. Small bubbles can be obtained in Figure 5.8(a, d). The flow pattern as shown in Figure 5.8(a) contains more bubbles in amount but smaller size than that in Figure 5.8(d). A thin layer rich in jetsam exists in Figure 8(b) but disappears in Figure 8(e). The well mixing state can be observed in the upper region in Figure 8(b, c). However, Figure 8(e) shows the concentration of jetsam in lower half is bigger than that in upper half while Figure 8(f) gives the opposite distribution of flotsam. The simulations comparison indicates that the local mixing-segregation balance is varied with different coefficients of restitution.

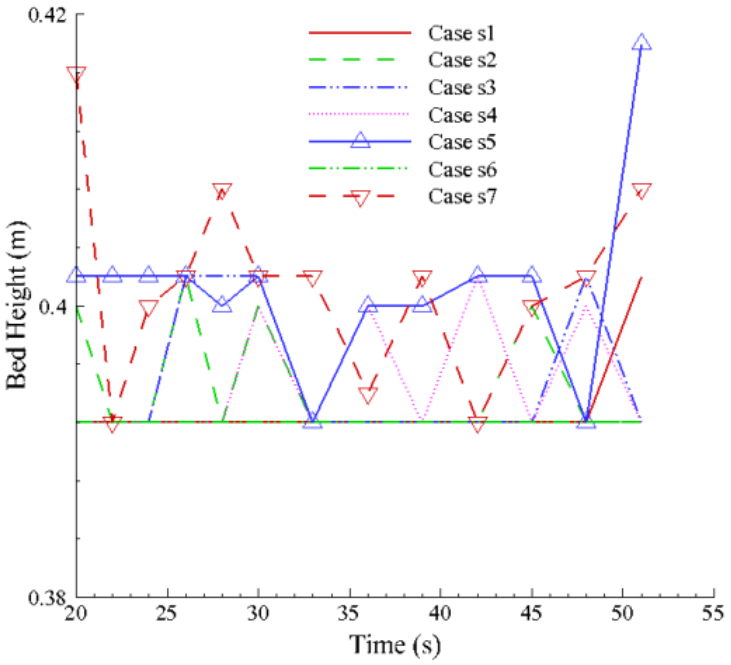

a

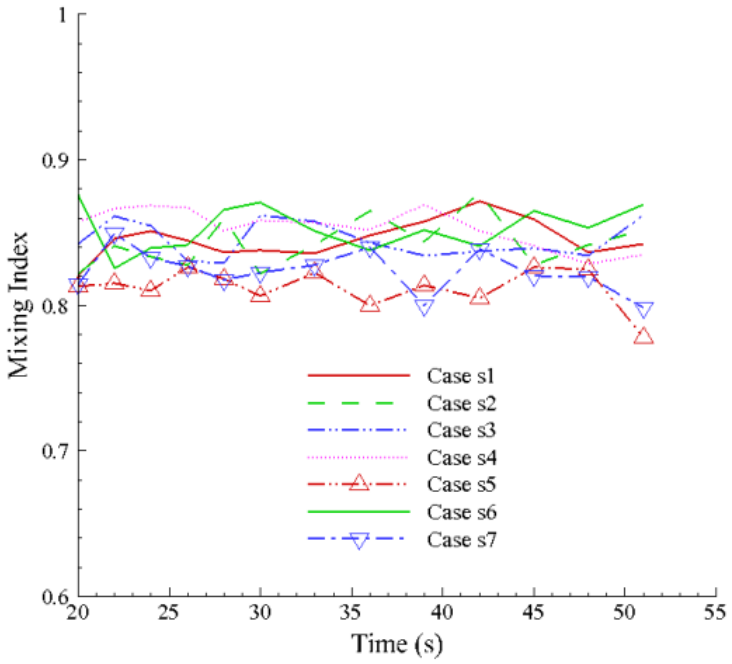

b

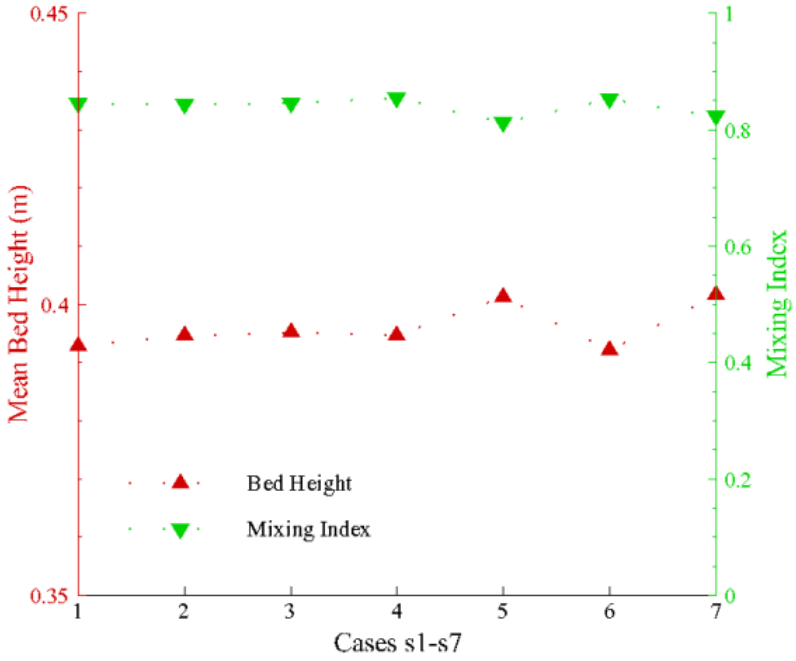

c

Figure 5.9 Effects of *e* on bed height (a,c)and mixing index(b,c).

Figure 5.9 shows the bed heights and values of mixing index from 20 to 51s. With the incremental coefficient of restitution as given in Cases s1-s5, there is a slight increase of bed height in Figure 5.9(a, c) when the value reaches at 0.99. The tendency is quite in consistence with that concluded from cases of density difference. The curves for mixing index show that the mixing index does not vary until the coefficient of restitution is equal to 0.99. The time-mean values are around 0.8 indicating a well mixing state. The relevant results deduce that the flow pattern varies when the coefficient of restitution is close to 1 corresponding to a slight changing of mixing-segregation balance. One more thing which should be noted is that the coefficient of restitution between solid phases given as 0.9 and 0.99 in Cases s6 and s7 did not display any difference on the final results. It indicates that the predicted energy dissipation by collisions of particles from different groups does not behave the same influence on flow pattern as that by collisions of particles in the same group.

Effect of size ratio

A bigger size ratio of jetsam and flotsam of 3.14 in Case s8 than that of 2.5 in Case s1 is applied to find out if the better segregation can be performed in the equilibrium state. Comparison of data of Case s1 and s8 at 30s is demonstrated in Figure 5.10. In contrast to Case s1, a high concentration zone, up to 50%, is visible at upper region of the bed while a thicker layer rich in jetsam exists in Case s8, which indicates a better segregation with the higher size ratio. In Case s8, the larger size of jetsam and comparable size of flotsam leads to a bigger minimum fluidization velocity of the binary mixture than that of Case s1. Thus the difference between the superficial velocity and the minimum fluidization velocity is smaller in Case s8. Considering of the connection between superficial velocity and mixing index, it concludes that the superficial velocity close to the minimum fluidization velocity separates the binary mixture more effectively. On the other hand, high superficial velocity achieves well mixing. The conclusion is in agreement with the experiments [124].

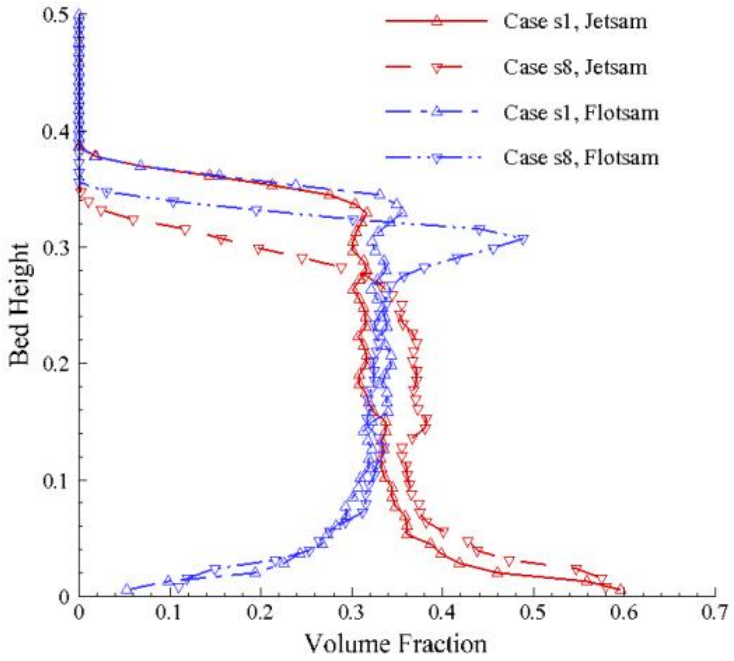

Figure 5.10 Comparion of concentration distributions of jetsam and flotsam in Cases s1 and s8 at 30s.

Effect of superficial velocity

Figure 5.11 shows the volume fraction of flotsam in the beds of Cases s8-s11 at 10, 15, 20 and 25 s. With the increasing superficial velocity, the fluidized beds expend to higher level from 0.354 to 0.476 m at 25s. The well mixing state exists steadily when the superficial velocity is not less than 0.2 m/s and the high concentration zone of flotsam can only be observed at 0.1 m/s. Comparison of results from simulations and experiments is given in Figure 5.12 and the segregation state at low velocity does not match well. Meanwhile the relevant works in literature [134, 215] showed that the segregation of binary mixture with the different size particles in Geldart group D or in groups A and D were well captured. The layers rich in jetsam of their works are much more obvious and thicker than that displays in simulation. It derives that the current model may not represent the segregation phenomena of the binary mixtures, where the particles sized in Geldart groups B and B/D are involved. The relevant correlations and functions need to be optimized to improve the accuracy.

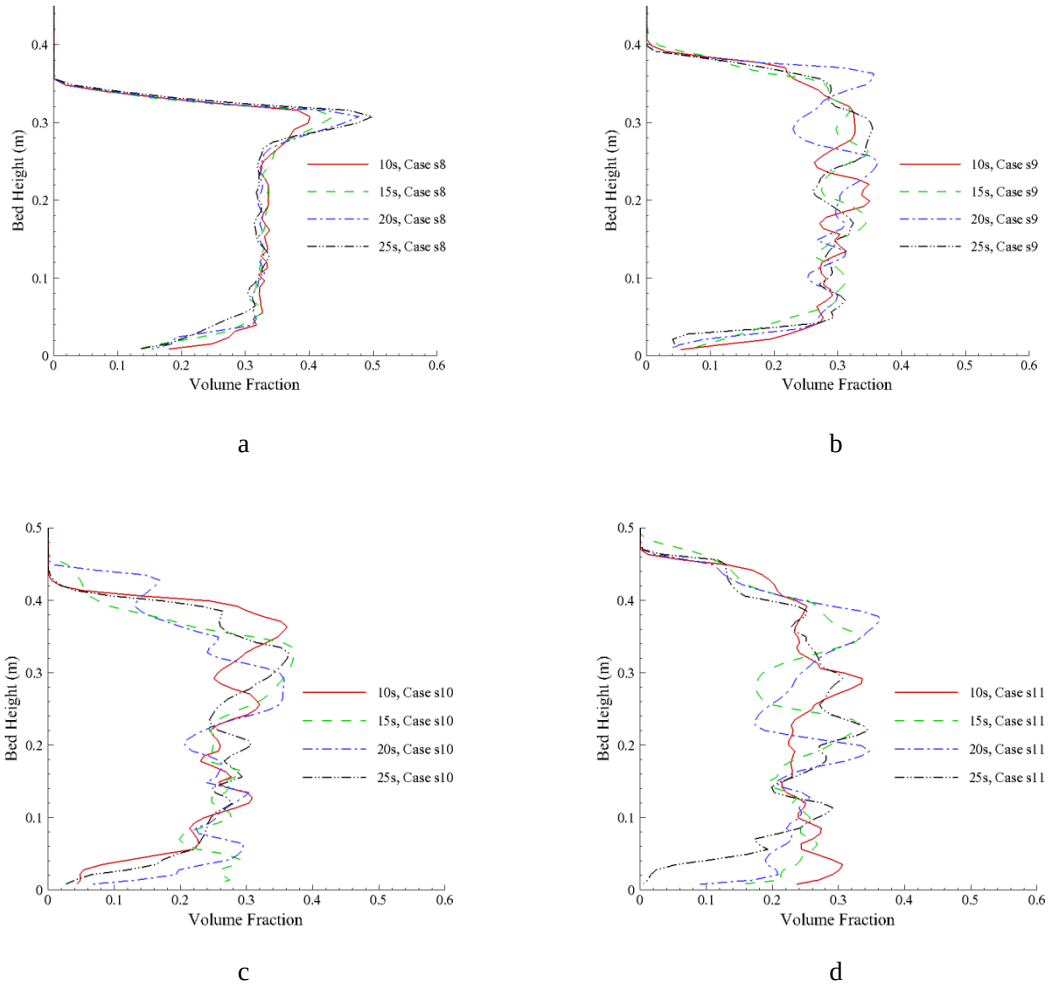

Figure 5.11 Concentration distributions of flotsam in Cases s8 –s11.

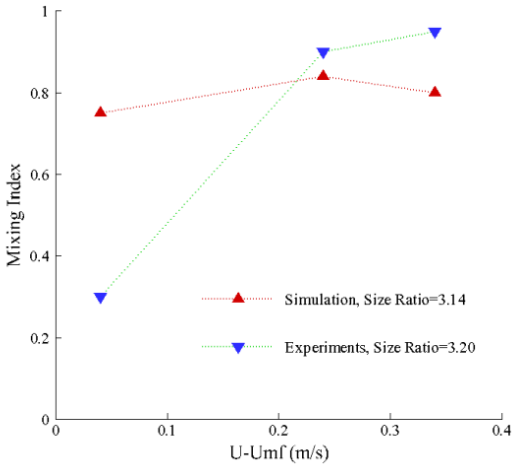

Figure 5.12 Comparison of mixing index of simulations and experiments.

5.4 Conclusions

In this chapter, the modelling work with Eulerian approaches was trying to represent the flow pattern of binary mixture in gas-solid bubbling fluidized beds. Two systems with particles with density difference and with size difference were investigated by a series of simulations and the effects from the functions and coefficients in use were introduced with data comparison such as the difference of the bed height and the mixing index. The relevant results are summarized as follows:

Segregation of binary mixtures with different densities in bubbling fluidized beds can be well captured in simulation; The flow pattern is not sensitive to the coefficient of restitution until it is much close to 1; The option of radial distribution function leads to ignorable changing on bed expansion and mixing-segregation equilibrium; The increasing superficial velocity leads the balance of mixing and segregation into the well mixing state. Although the binary mixtures in size difference separate partially in simulation prediction, the segregation efficiency is much lower than that in realistic conditions. The prediction of gas-solid drag is regarded to be approximate and the segregation proceeds successfully for binary particles of different densities in Geldart group B. The previous model for solid-solid interactions needs to be improved for separation of particles in size difference.

Chapter 6: Fast pyrolysis

6.1 Introduction

Fast pyrolysis of biomass has been studied extensively due to the interests in the primary product, bio-oil. A series of works on pyrolysis mechanism have been reported and the end products are extensive studied and analyzed. The development of modelling of fast pyrolysis is slow because of the limited progresses on kinetics development. The following work is trying to employ the existing approaches to investigate the fast pyrolysis of biomass samples, numerically. Meanwhile the modified reaction constants are introduced into kinetic scheme for biomass fast pyrolysis in which the intra-particle heat penetration can be taken into account. The simulation results are validated with the experimental data.

6.2 Model Setup

6.2.1 Mathematical Model

In the current work, the thermal decomposition of biomass in a gas-solid fluidized bed is represented by Eulerian approaches, numerically. One gas phase and two solid phases are defined in modelling, which are treated as three interpenetrating continua with individual volume fractions. The gas phase is a mixture of N_2, tar and syngas. Meanwhile one of the solid phases, s_1, is a mixture of biomass and char with the initial volume fractions of 1 and 0, respectively. The other solid phase, s_2, is sand. The physical properties of gas and solids are given in Table 6.1.

Table 6.1 Physical properties

Property	Value	Unit
ρ_{bio}	400	kg/m^3
ρ_{cha}	200	kg/m^3
ρ_{san}	2500	kg/m^3
ρ_{syn}	30	g/mol
ρ_{n_2}	28	g/mol
ρ_{tar}	100	g/mol
Cp_{bio}	1500	J/kgK
Cp_{cha}	1100	J/kgK
Cp_{san}	835	J/kgK
Cp_{syn}	1100	J/kgK
Cp_{n_2}	1091.6	J/kgK
Cp_{tar}	2500	J/kgK
μ_{syn}	3e-5	$kg/s\,m$
μ_{tar}	3e-5	$kg/s\,m$
μ_{n_2}	3.58e-5	$kg/s\,m$
λ_{bio}	0.105	$W/m\,K$
λ_{cha}	0.071	$W/m\,K$
λ_{san}	0.35	$W/m\,K$
λ_{syn}	0.02577	$W/m\,K$
λ_{tar}	0.02577	$W/m\,K$
λ_{n_2}	0.0563	$W/m\,K$
d_{bio}	0.4, 0.55,1.8	mm
d_{san}	0.4	mm

Due to the presence of solid phase s1 and solid phase s2, a three-fluid model is constructed which is similar and extended by TFM coupling with KTGF. The governing equations have to be completed with considerations of the interaction between solid phases and the mass and heat transfer among gas and solid phases. The momentum exchange between gas and solid phases is estimated by Gidaspow model [60] meanwhile that between solid phases is considered by Syamlal *et al.* model[211]. The mass transfer in reactions is defined by the mass conservation of chemical species. The subsequent

variations are present in the momentum and energy equations. The heat exchange between sand and biomass is not taken into account. The governing equations are summarized as follows. The constitutive equations were given in Chapters 3 and 5.

Gas phase.

The species mass fraction is solved separately to represent the species mass balance:

$$\frac{\partial}{\partial t}(\varepsilon_g \rho_g Y_i) + \nabla \cdot (\alpha \varepsilon_g \rho_g \vec{u}_g Y_i) = \dot{M}_i, \quad 6.1$$

where Y_i and $\dot{M}_i$ are the local mass fraction and the net production rate of species i, i = 1, 2, …, n, respectively. The density of gas phase, ρ_g, is computed by ideal gas law as

$$\rho_g = \frac{p}{RT \sum_{i=1}^{n} \frac{Y_i}{w_i}}, \quad 6.2$$

where p is the operating pressure, R is the universal gas constant and w_i is the molecular weight of the gas.

The mass conservation of gas phase is written as follows:

$$\frac{\partial}{\partial t}(\varepsilon_g \rho_g) + \nabla \cdot (\varepsilon_g \rho_g \vec{u}_g) = \sum_{m=1}^{2} (S_{sm,g} - S_{g,sm}) \quad 6.3$$

and

$$\sum_{m=1}^{2} (S_{sm,g} - S_{g,sm}) = \sum_{i=1}^{n} \dot{M}_i. \quad 6.4$$

The term on the right-hand side of Equation 6.3 describes the net mass exchange between solid phase and gas phase by heterogeneous reactions.

The momentum conservation equation of gas phase is given with additional terms considering interphase interactions and momentum exchange by mass transfer. $K_{sm,g}$ is the momentum exchange coefficient between gas and solid phases:

$$\frac{\partial}{\partial t}\left(\varepsilon_g \rho_g \vec{u}_g\right) + \nabla \cdot \left(\varepsilon_g \rho_g \vec{u}_g \vec{u}_g\right) = -\varepsilon_g \nabla p + \nabla \cdot \bar{\bar{\tau}}_g + \varepsilon_g \rho_g \vec{g} + \sum_{m=1}^{2} (K_{sm,g}\left(\vec{u}_{sm} - \vec{u}_g\right) + S_{sm,g}\vec{u}_s - S_{g,sm}\vec{u}_g). \quad 6.5$$

Compared to Equation 3.17, the last term on the right-hand side of Equation 6.5 is extended due to the presence of the second solid phase and the mass transfer in reactions.

The enthalpy equation is introduced to represent conservation of energy for gas phase:

$$\frac{\partial}{\partial t}\left(\varepsilon_g \rho_g \Psi_g\right) + \nabla \cdot \left(\varepsilon_g \rho_g \Psi_g \vec{u}_g\right) = -\varepsilon_g \frac{\partial p_g}{\partial t} + \bar{\bar{\tau}}_g : \nabla \vec{u}_g - \nabla \cdot q_g - \Delta \dot{H}_g + \sum_{m=1}^{2} h_{sm,g}(T_{sm} - T_g) \quad 6.6$$

where Ψ_g is the specific enthalpy of gas phase, the heat exchange between solid phase(s1 or s2) and gas phase is considered respectively by the last term on the right-hand side of Equation 6.6, and $\Delta \dot{H}$ is the source term for heat of reaction.

Solid Phase.

The mass balance equations of species in solid phases are given with the similar form with gas phase:

$$\frac{\partial}{\partial t}(\varepsilon_{sm}\rho_{sm}Y_i) + \nabla \cdot (\varepsilon_{sm}\rho_{sm}\vec{u}_{sm}Y_i) = \dot{M}_i, \quad 6.7$$

$$\frac{\partial}{\partial t}(\varepsilon_{sm}\rho_{sm}) + \nabla \cdot (\varepsilon_{sm}\rho_{sm}\vec{u}_{sm}) = S_{g,sm} - S_{sm,g} \quad 6.8$$

and

$$S_{g,sm} - S_{sm,g} = \sum_{i=1}^{n} \dot{M}_i \ , \ m \text{ = 1 or 2.} \quad 6.9$$

The density of solid phase has the following function:

$$\rho_{sm} = \frac{1}{\sum_{i=1}^{n} \frac{Y_i}{\rho_i}}. \qquad 6.10$$

Conservation of momentum is written by introducing the additional terms into Equation 3.17 with considerations of solid-solid phase interactions and chemical reactions:

$$\frac{\partial}{\partial t}(\varepsilon_{sm}\rho_{sm}\vec{u}_{sm}) + \nabla \cdot (\varepsilon_{sm}\rho_{sm}\vec{u}_{sm}\vec{u}_{sm}) = -\varepsilon_{sm}\nabla p + \nabla p_{sm} + \nabla \cdot \bar{\bar{\tau}}_{sm} + \varepsilon_{sm}\rho_{sm}\vec{g} + K_{g,sm}(\vec{u}_g - \vec{u}_{sm}) + \sum_{l=1}^{2} K_{sl,sm}(\vec{u}_{sl} - \vec{u}_{sm}) + S_{g,sm}\vec{u}_g - S_{sm,g}\vec{u}_{sm} \quad , \; m = 1 \text{ or } 2, \qquad 6.11$$

where $K_{sm,sl}$ is the momentum exchange coefficient between solid phases and $K_{sm,sm}$ is equal to 0, the last two terms on the right-hand side describe the contribution of mass transfer in reactions.

Conservation of energy is given by:

$$\frac{\partial}{\partial t}(\varepsilon_{sm}\rho_{sm}\Psi_{sm}) + \nabla \cdot (\varepsilon_{sm}\rho_{sm}\Psi_{sm}\vec{u}_{sm}) = -\varepsilon_{sm}\frac{\partial p_{sm}}{\partial t} + \bar{\bar{\tau}}_{sm} : \nabla \vec{u}_{sm} - \nabla \cdot q_{sm} - \Delta \dot{H}_{sm} + h_{g,sm}(T_g - T_{sm}) \quad , m = 1 \text{ or } 2. \qquad 6.12$$

Ψ_{sm} is the specific enthalpy of solid phase m, $h_{g,sm}$ is the heat exchange between solid and gas.

6.2.2 Numerical Model Setup

Biomass fast pyrolysis is experimentally investigated in a fluidized bed reactor by Liu *et al.* [216]. In the current work, a 2-D geometry is set up numerically with the diameter of 100 mm and the height of 600 mm based on the rig used in experiments. The schematic is

given in Figure 6.1. Sand particles are loaded above the bottom distributor with the bed height of 50 mm and the packing rate of 0.63 initially. Although the real sizes of sand and biomass are distributed in a range, the size distribution is not defined in the numerical model and the uniform size is given to both sand and biomass particles individually. The sand size is 0.4 mm which is categorized into Geldart group B. The biomass size varies from 0.4 to 1.8 mm in different cases. Biomass particles are injected by feeding gas from the side inlet point (inlet 1) at the height of 75 mm. The sand particles are fluidized by fluidizing gas from the bottom distributor (inlet 0). In the simulation work, the hot N_2 is introduced as the feeding and fluidizing gas at the temperature of $500C^o$. However, in experiments corn stalk samples are injected with cold N_2 to prevent the decomposition of biomass in spiral feeder. Hence the consequent effects of cold feeding gas on the temperature fields in the reactors cannot be addressed in simulations. The composition analysis of corn stalk samples is: cellulose of 37.6 wt.%, hemi-cellulose of 21.6 wt.%, lignin of 18.4 wt.% and extractives [216]. In the current simulations, the mass fractions of three pseudo-components used to define the initial composition of biomass are translated to 23.7 wt.%, 27.8, and 48.5 wt.%, approximately because no extractive is defined for biomass.

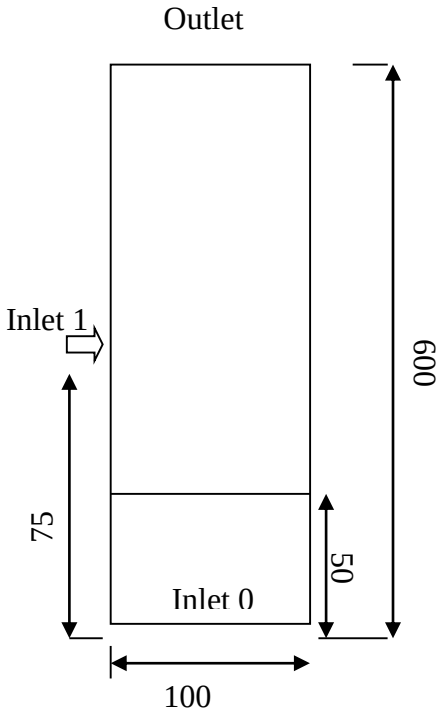

Figure 6.1 Schematic of the fluidised bed reactor in use (Unit: mm).

The governing and constitutive equations are solved by finite volume method (FVM) via ANSYS FLUENT. The reaction scheme is incorporated by user define function (UDF). The constructed mesh is generated for computational domain with the grid size of 3 mm at lower region and bigger size of 5 mm for the upper half. The mesh in use is given in Figure 6.2. No-slip boundary conditions are defined for gas and free slipping for solids on the wall. The SIMPLE algorithm is used for pressure-velocity coupling while first upwind scheme for discretisation of convective terms. The time step size is set to 0.0001s and the convergence criterion is 0.001. The simulation was running for a real time of 40s.

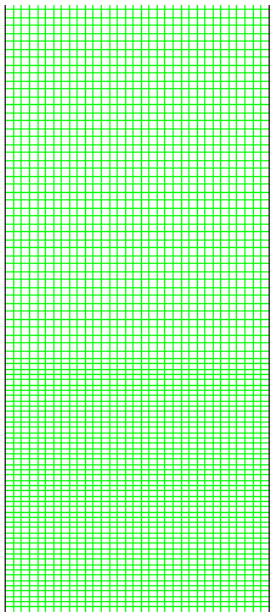

Figure 6.2 Computational domain discretization.

6.2.3 Intra-particle Heat Penetration

Intra-particle heat conduction cannot be ignored if the conductive process affects the temperature distribution and then the chemical reactions. Due to the limitation of Eulerian approaches, tracking the internal phenomena of particles seems to be difficult or impossible. Hence an indirect method by applying the effect of heat penetration on the reacting rate was proposed [168]. The temperature distribution and heat transfer inside particles are not represented directly but the modification on reacting constant is given to show the influence of heat conduction on chemical reactions. The details are given as follows:

$$1/k' = 1/k + 1/k_{hp} \qquad 6.13$$

where k is the reaction constant, k' is the modified reaction constant and k_{hp} is the heat penetration rate. As proposed, the heat penetration rate is a function of heat transfer coefficient, specific surface area and specific heat capacity of particles. The detailed correlation is shown as:

$$k_{hp} = h \Lambda_{ssa}/Cp \quad 6.14$$

k' was introduced and programmed into the modelling to replace the reaction constant to investigate the relation between end-product distribution and intra-particle heat conduction.

6.3 Results and Discussion

6.3.1 Boundary Condition Setting

Different definitions for outlet boundary conditions are given and compared via Cases 1 and 2 in Table 6.2. Generally the pressure-out boundary conditions are given and introduced into multiphase flow modelling. However the mass flow rate of solid phase passing through the outlet boundary cannot be tracked easily. For a setting of no backflow rate of biomass on the outlet, a steep gradient of biomass (char) concentration is present as shown in Figure 6.3, which is not visible by defining the outlet boundary condition as outflow.

Table 6.2 Case details (I)

Case	velocity	d_{bio}	Outlet boundary condition
	m/s	mm	
1	0.8	0.4	Pressure-outlet
2	0.8	0.4	outflow

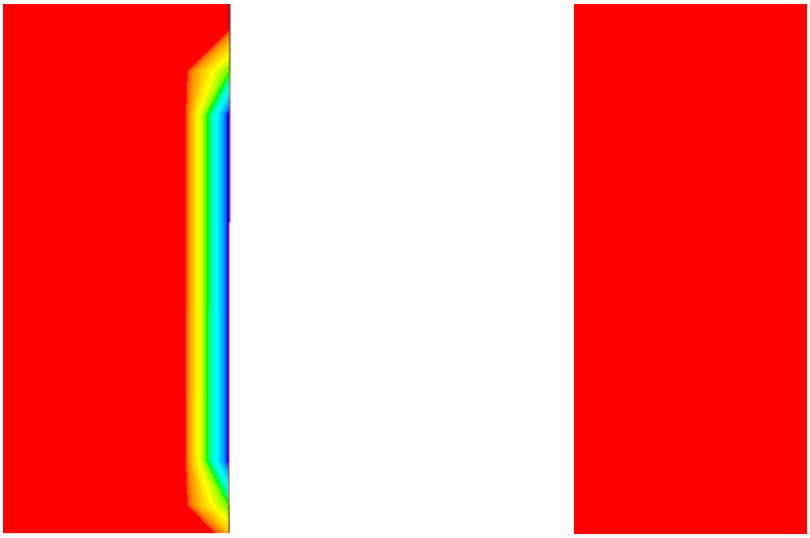

a b

Figure 6.3 Biomass condensation distribution near the outlet for different boundary condations: a. pressure-outlet; b. outflow.

The variation exists due to the different definitions of the two boundary conditions. For pressure-outlet setting, all the variables are fixed to given values. For instance, the pressure on the outlet is equal to the ambient pressure and other variables are set to 0. Based on SIMPLE algorithm, the continuous pressure distribution is calculated and adjusted according to the outlet pressure. However the distributions of other variables such as volume fraction, mass fraction, *etc*., are obtained by the upwind scheme. The high concentration of biomass in the coming flow together with the given value of 0 on the outlet boundary performs the sharp decrease. The definition of outflow boundary condition is different and the normal gradients for variables are 0 except the pressure. Hence, the steep gradients will not be present. The colour contours in Figure 6.3 show that the effects of different conditions are limited in a small area near the outlet. Meanwhile it can be predicted that the hydrodynamics and concentration distributions of species will not be varied significantly due to the application of the upwind scheme.

Figure 6.4 shows the curve of bed heights from 20 to 40s for Cases 1 and 2. The time averaged heights of 0.143 and 0.139 m indicate that the mean voidage of the fluidized bed

in Case 1 is a little bigger than that in Case 2. The hydrodynamics of fluidized bed give a direct influence on the heating up of samples and lead to a different yield distributions. Consequently, a lower ratio of syngas over tar in Case 2 is present in the freeboard region as shown in Figure 6.5, because of the relatively lower ratio at low level. A gradual increase of the syngas to tar ratio by height can be observed in the two cases. The similar tendencies are followed because the secondary cracking of tar into syngas is considered by the kinetics. At the level of 550 mm in the reactors, the time averaged ratio from 20 to 40s for Case 1 is 0.31 while it is 0.3 for Case 2. Considering the ignorable difference on hydrodynamics and the similar fractional yield distribution, both the definitions of outlet boundary conditions are acceptable. The results show good agreement with the prediction above.

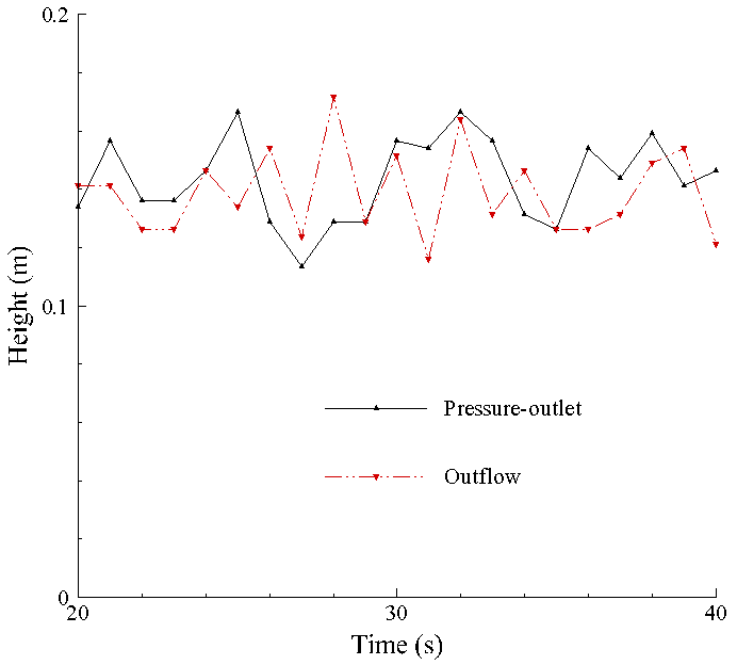

Figure 6.4 Bed heights by time in Cases 1 and 2.

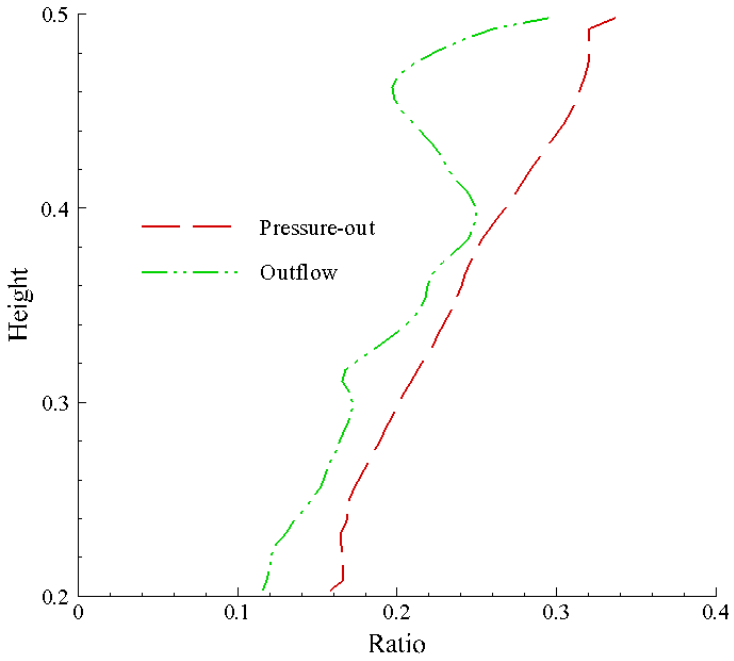

Figure 6.5 Ratio of syngas to tar in freeboard in reactors of Cases 1 and 2.

6.3.2 Effects of Different Superficial Velocities

It is clear that hydrodynamics of the fluidized beds affect the heat exchange efficiency and then the yield distribution as mentioned above. The detailed studies were carried out to investigate the relation between flow pattern and chemical reactions by decreasing the superficial velocity of fluidizing gas from 0.8 m/s in Case 1 to 0.5 and 0.2 m/s in Cases 3 and 4 while the biomass sizes in Cases 1, 3 and 4 are the same: 0.4 mm. A brief introduction is given in Table 6.3.

Table 6.3 Case details (II)

Case	velocity	d_{bio}	Outlet boundary conditions
	m/s	mm	
3	0.5	0.4	Pressure-outlet
4	0.2	0.4	Pressure-outlet

Figure 6.6 shows the flow patterns at 40 s for different superficial velocities. It is no doubt that the bed voidage decreases with reducing fluidizing gas velocity. The smallest bubbles are distinct at the lowest velocity of 0.2 m/s in the bed, which is the classic bubbling fluidization. The bubble size is much larger by increasing the velocity to 0.5 m/s and the fluidization state is transforming to turbulent fluidization at the velocity of 0.8 m/s.

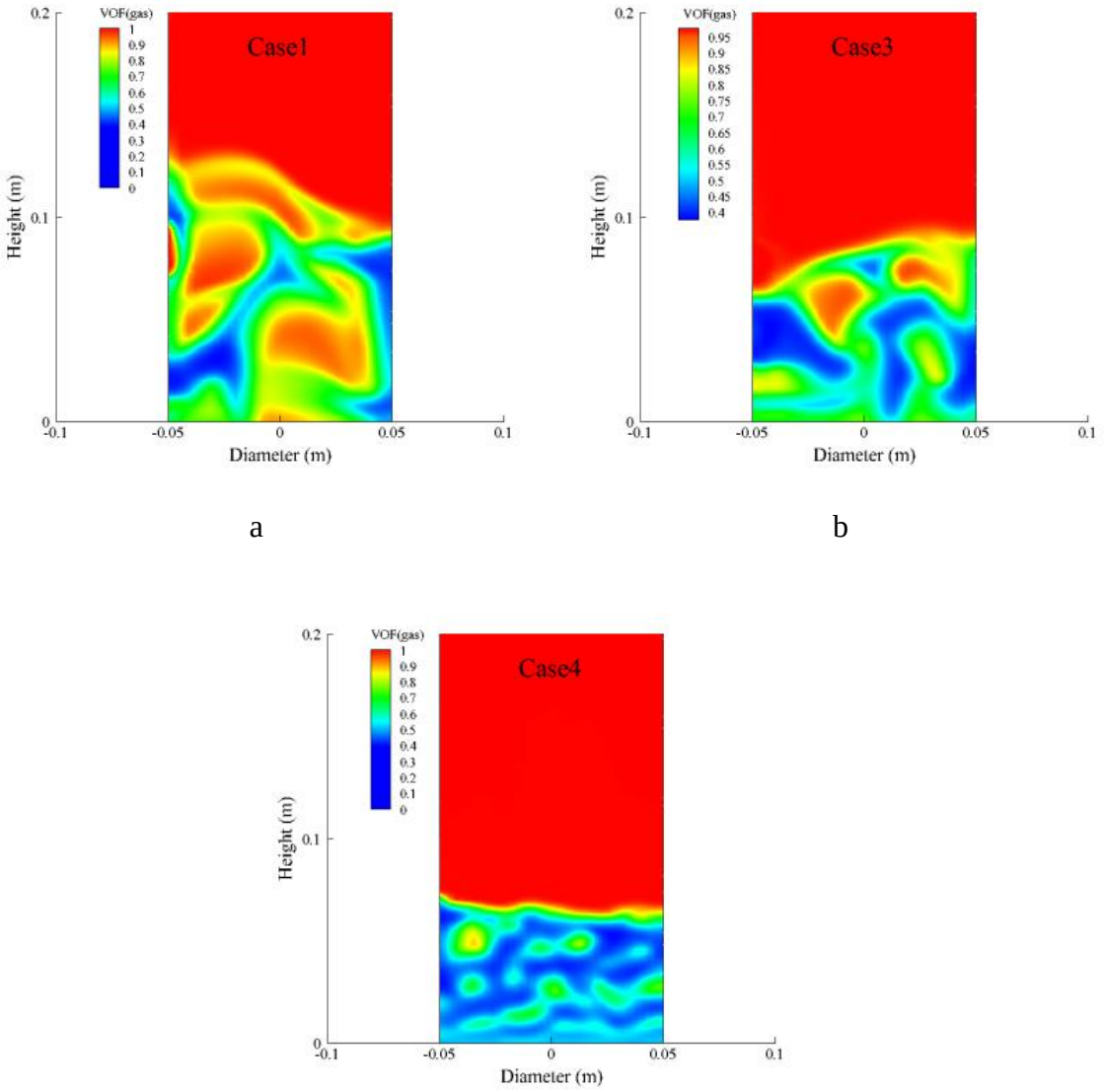

a b

c

Figure 6.6 Flow patterns at different superficial velocities (a: Case 1; b Case 3; c: Case 4).

The by-product, char, has been reported as a catalyst to speed up tar decomposition, although the char-cracking progress is not considered in the current work. Fast removal of the char to reduce the contacting time with tar is supposed to be effective on restraining the secondary cracking in biomass pyrolysis. Therefore, the superficial velocity has to be considered for high heat exchange rate together with the removal efficiency of char particles. Figure 6.7 shows the char volume-fractional distributions of Cases 1, 3 and 4.

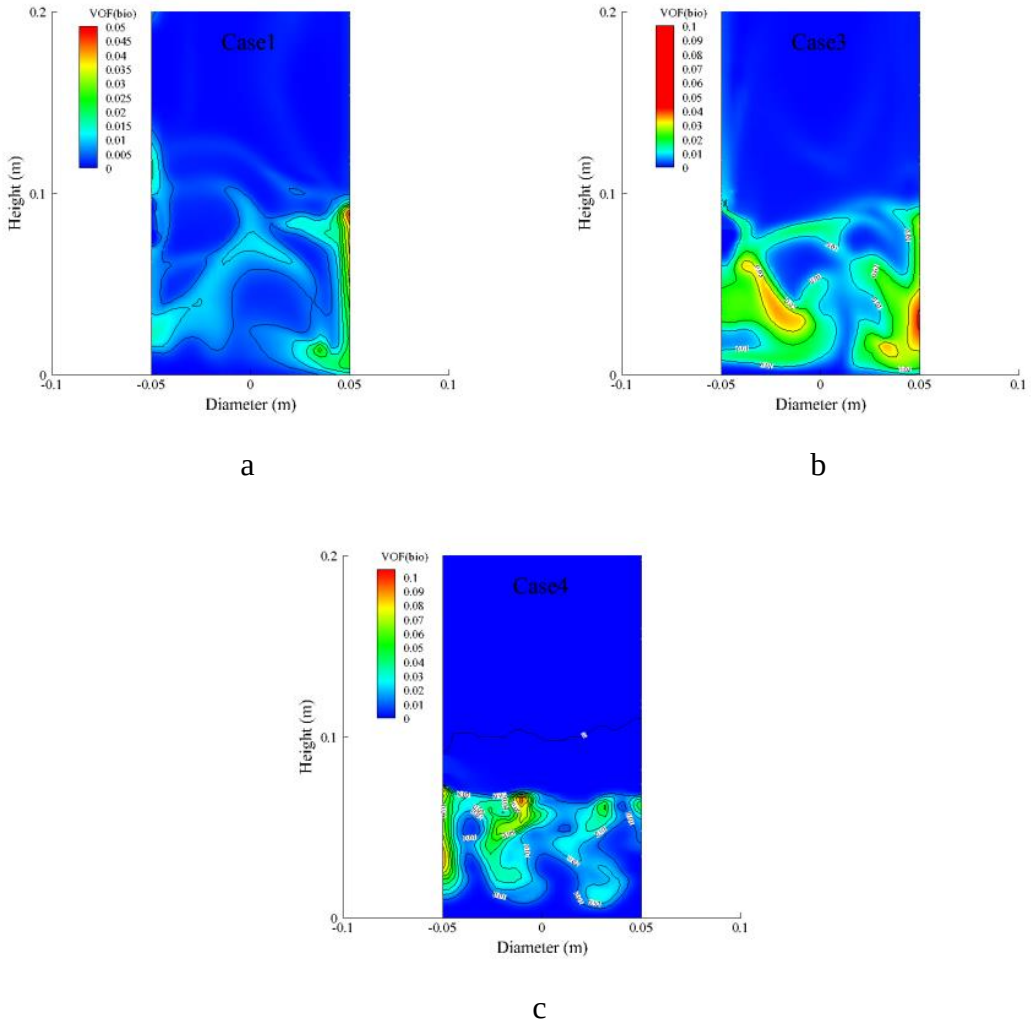

Figure 6.7 Char distributions at different superficial velocities (a: Case 1; b Case 3; c: Case 4).

The colour contours represent the char concentration at 40s when the fluidizing gas is injected with the velocity of 0.8, 0.5 and 0.2 m/s. The simulation results display that no

reacted particle escapes successfully when the superficial velocity is lower than 0.5 m/s. It deduces that the terminal velocity of char particles is between 0.5 and 0.8 m/s. The segregation phenomena are visible in Figure 6.7(c) and the equilibrium of mixing and segregation is broken at higher gas velocity as shown in Figure 6.7(b). The full entrained behaviour occurs corresponding to the lowest instant remaining of char particles in beds.

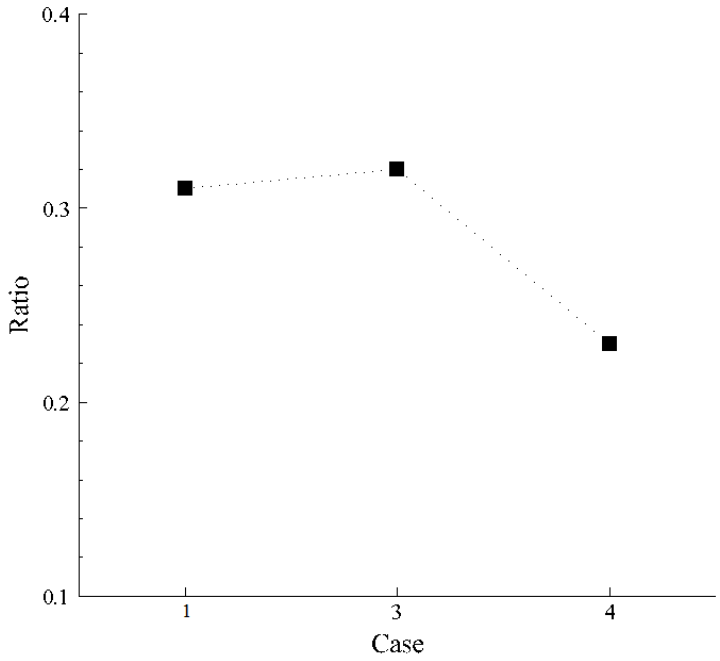

Figure 6.8 Ratio of syngas to tar in Cases 1, 3 and 4.

Figure 6.8 gives the yield ratios of syngas and tar of Cases 1, 3 and 4. According to the simulation results, the yield ratios of syngas to tar are close when the gas velocity is bigger than 0.5 m/s. However, a smaller syngas-tar ratio is performed at lower fluidization intensity– in Case 4. The results prove that the hydrodynamics have significant connection with the frictional yields of end-products again.

6.3.3 Intra-particle Heat Transfer

The heat penetration inside particles cannot be studied directly due to the limitation of Eulerian approaches. In the current work, different size samples are injected into the

reactor and the effects of intra-particle heat penetration are discussed. Three cases are compared in the following section. The modified reaction constants introduced in section 6.2.3 was programed and incorporated into the first step of the kinetics in Cases 5. As the decomposition of the pseudo-components into actives are quick or instant processes, the heat conduction effects applied on the first step may be seriously underestimated. Case 6 was set up by modifying the kinetics on the second step, from actives into syngas, char and tar. To test the sensitivity of kinetics modification, studies on Cases 7 and 8 with a larger biomass size of 0.55 mm than that of 0.4 mm in Cases 5 and 6 were also carried out and the details are given in Table 6.4. In Case 7, the first-step reaction constants are modified by consideration of intra-particle heat penetration whilst the modifications on the second step in Case 8.

Table 6.4 Case details (III)

Case	velocity	d_{bio}	Kinetics modification
	m/s	mm	
5	0.8	0.4	First step
6	0.8	0.4	Second step
7	0.8	0.55	First step
8	0.8	0.55	Second step

Figure 6.9 shows the fractional yields of the end products in Cases 2, 5 and 6. No intra-particle heat conduction is considered in Case 2 but the same biomass size of 0.4 mm was used in Cases 2, 5 and 6. By applying the introduced model into first step degrading, a slight decrease of tar production can be observed corresponding with more syngas produced. The results indicate that the kinetics modification is behaving positively. In Case 6, a visible increase of char yield is achieved by consuming a considerable amount of tar and few syngas. In comparison of Cases 7 and 8, the different modifications on first or second step show limited difference as shown in Figure 6.10. By summarizing

the results of Cases 2, 5-8, more consumption of tar to char is given if the modified reaction constant is introduced into the second step of biomass fast pyrolysis meanwhile the syngas production varies slightly in all cases.

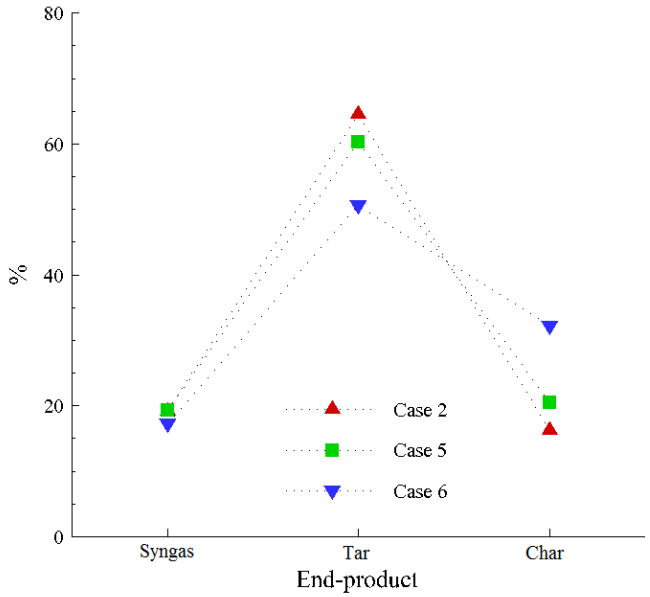

Figure 6.9 Fractional yields of syngas, tar and char in Cases 2, 5 and 6.

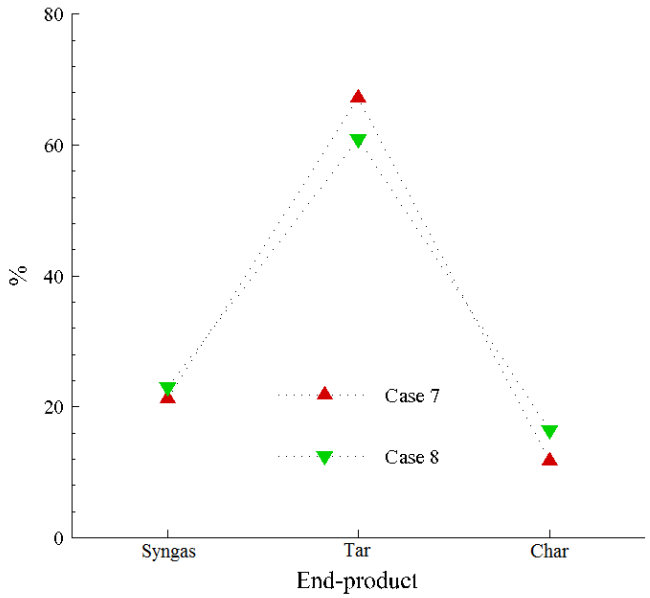

Figure 6.10 Fractional yields of syngas, tar and char in Cases7 and 8.

6.3.4 Validation

Table 6.5 Case details (IV)

Case	velocity	d_{bio}	Kinetics modification
	m/s	mm	
9	0.8	1.8	First step
10	0.8	1.8	Second step

The modelling of particle pyrolysis is carried out by using the larger particle size of 1.8 mm in Cases 9 and 10 while the first-step modification is given in Case 9 and the second step modification for Case 10. In Cases 9 and 10, the terminal velocity of biomass particles is much bigger than the superficial velocity in use, the production of char cannot be calculated directly. The ratio of syngas to tar is compared in Figure 6.11.

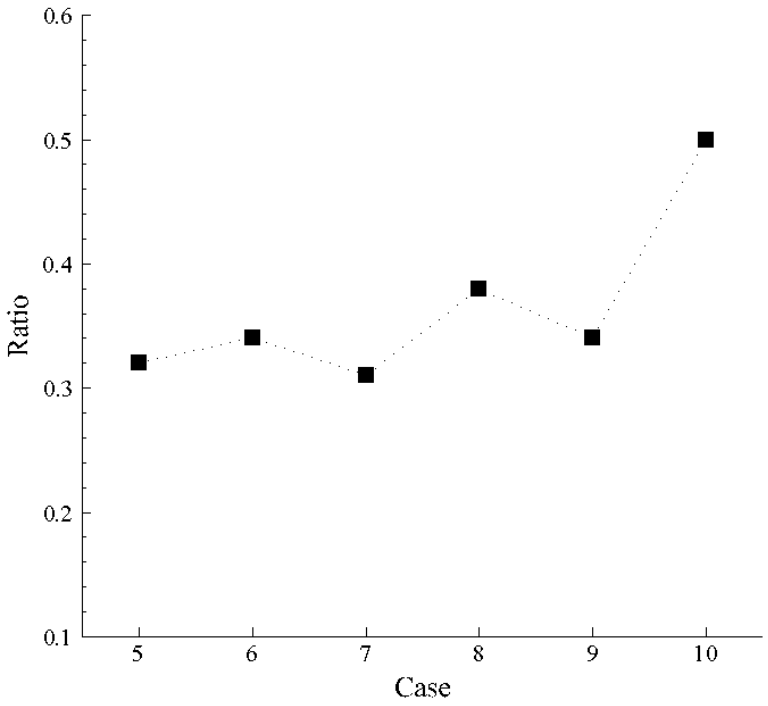

Figure 6.11 Ratios of syngas to tar in Cases 5-10.

By considering the effect of heat penetration on the first step, no obvious difference on the ratio of syngas to tar is performed in Case 5 and 7 with biomass particles at size of 0.4 and 0.55 mm, respectively. A higher ratio is given when the samples of 1.8 mm degrade in Case 9. On the other hand, if the reaction constants of the second step were modified, ratio of syngas to tar varies obviously with the increasing biomass size from 0.4 to 1.8 mm in Cases 6, 8 and 10.

Table 6.6 Fractional yields of corn stalk decomposition[216]

Particle size/mm	Yields of products			
	Bio-oil/wt.%	Char/wt.%	Syngas/wt.%	Ratio of syngas to tar
<0.45	41.67	13.33	45	1.08
0.45~0.6	39.58	14.58	45.84	1.16
1.6~2.0	33.33	18.33	48.34	1.45

Comparing the experimental data [216] given in Table 6.6 with simulation results in Figure 6.11, the considerable deviation of ratio of syngas to tar can be observed which can be attributed to the reasons following:

Gas superficial velocity: The gas flow rate used in experimental work is not introduced whilst three velocities with the given values of 0.2, 0.5 and 0.8 m/s are applied in simulations. The effects of gas superficial velocity on frictional yields of products are discussed in section 6.3.2;

Reacting temperature: Cold gas is used for biomass feeding in experiments. The low temperature zone forming near the feeding point (inlet 1) leads to different degrading rates and eventually to different yields of end-products;

Apparent biomass composition: As introduced in section 6.2.2, extractives (about 20wt.%) exist in samples used in experiments that are not present in simulations and the corresponding contributions on final yields cannot be addressed;

Kinetic scheme: The interactions between pseudo-components in degrading are not introduced in the kinetic scheme while the activation energy and pre-exponential factors are given empirically in simulations.

Bio-oil collection: In simulations, the results were obtained from the outlets of fluidized bed reactors. However one cyclone and one or several condensers were present in experiments for char removal and bio-oil collection before the experimental data collection. The yields of end-products are significantly related to the thermal cracking of tar and the condensation efficiency of the condenser in these additional processes.

Because of the reasons mentioned above, only a qualitative comparison between simulation results and experimental data can be carried out. As illustrated from experimental data, the ratio of syngas to tar is enlarged with the increasing biomass particle size which can also be obtained from the simulation results as shown in Figure 6.11. Meanwhile the case studies in simulations indicated that the modification on the second-step reaction constant behaves more sensitive if large size particles are considered.

6.4 Conclusions

In this chapter, the fast pyrolysis of biomass is modelled by Eulerian approaches. The hydrodynamics of fluidized beds at different superficial velocities are investigated with the corresponding effects on the final frictional yields of end products. The consideration of heat conduction internal particles are described and incorporated into the fast pyrolysis model. The sensitivity of the correlations is discussed by the case studies with different sizes of particles. The simulation results show that the definition of boundary conditions

shows ignorable effects on simulation results; the suitable superficial velocity has to be given by considering the char removal and the yields of tar; the modification of kinetics shows more sensitivity on the second step than on the first step. Meanwhile the incorporation of correlation for internal particle conduction delivers the similar trend with experiments, qualitatively.

Chapter 7: Catalytic Pyrolysis

7.1 Introduction

Utilization of bio-oil drives the development of biomass pyrolysis techniques significantly. Due to the disadvantage of bio-oil, upgrading of the quality is necessary to satisfy the industrial requirement. Catalytic cracking of bio-oil into petroleum-like fuels is a hot topic in recent studies. Based on the development of catalyst technology, numerical approaches are employed to aid the application of catalyst into biomass pyrolysis. The kinetic studies of catalytic cracking are directly derived from the catalyst with specific activity and selectivity. The reaction mechanism is much more complicated with the presence of catalyst than that controlled simply by temperature. The pyrolysis of sawdust in a reactor with an in *situ* catalyst has been studied empirically by Atutxa *et al*. [181]. A reaction scheme is proposed based on the relation between the fractional distribution of the yields and the space time defined as the ratio of catalyst mass to liquid flow rate. The present work attempts to set up a valid numerical model using the proposed kinetics to investigate the catalytic pyrolysis of biomass in bubbling fluidized beds. The similar work is not reported in literature yet.

7.2 Numerical Model

7.2.1 Mathematical Model

The two-fluid model (TFM) coupled with kinetic theory of granular flows (KTGF) has been widely used in two-phase flow simulations[149, 164]. Both the solid and gas phase are treated as interpenetrating continua with individual volume fractions. Solids viscosity, solids pressure, granular temperature, *etc*., derived from KTGF are used to express the motion of solids. In the present work, three fluid phases are present in the bed: one gas phase and two solid phases (s1, s2). The gas phase is a mixture of N_2, tar and syngas. One of the solid phases (s1) is a mixture of biomass and char while the other phase (s2) is pure catalyst. The TFM is extended to simulate multiphase flow by adding the interactions between solid phases. The governing equations and the related constitutive equations are the same with

those in Chapter 6. The heat exchange between solid phases taken into account by particle collisions is investigated in this work.

7.2.2 Kinetics

In the reaction kinetics, tar produced from primary reaction decomposes into syngas and char which is termed as thermal cracking. For the online upgrading of tar, Atutxa et al.[181] introduced a catalytic cracking mechanism to replace the thermal cracking one due to the presence of a catalyst. Meanwhile, the primary reaction is not supposed to be affected by catalytic behaviour. The space time, ζ, defined as the ratio of catalyst mass to tar flow rate, $Wm_{cata}/\dot{m}_{tar}$, is considered to control the catalytic cracking progress. The scheme and reaction constants for catalytic pyrolysis are given in Chapter 3.

7.2.3 Interphase Collisional Heat Exchange

Table 7.1 Heat transfer coefficient between solid phases

Heat transfer coefficient	
$h_{s1,s2} = f(n_{s1}, n_{s2}) * \Gamma$	7.1
$h_{s1,s2} = h_{s2,s1}$	7.2
Collision frequency	
$f(n_{s1}, n_{s2}) = n_{s1} n_{s2} (r_{p,s1} + r_{p,s2})^2 \sqrt{8\pi(\Theta_{s1} + \Theta_{s2})}$	7.3
$\Gamma = \frac{5.36(m/E)^{3/5}(ru_{sli})^{7/10}}{(\rho_{s1} c_{ps1} \lambda_{s1})^{-1/2} + (\rho_{s2} c_{ps2} \lambda_{s2})^{-1/2}}$	7.4
$r = \frac{r_{p,s1} r_{p,s2}}{r_{p,s1} + r_{p,s2}}$	7.5
$m = \frac{m_{p,s1} m_{p,s2}}{m_{p,s1} + m_{p,s2}}$	7.6
$E = \frac{4/3}{(1-\gamma_{s1}^2)/G_{s1} + (1-\gamma_{s2}^2)/G_{s2}}$	7.7

A correlation for heat exchange via single collision was given in the function of particle mass (m_p), radius (r_p), slip velocity (u_{sli}), elastic modulus (G) and poission ratios γ by Sun and Chen [217]. Chang *et al*. [86, 218]combined the direct conduction in a single collision

with collision frequency to estimate the heat exchange between two solid classes. The collision frequency is the function of the number concentration (n), radius (r_p) and granular temperature (Θ). In the current work, the heat convection between sawdust and fluidized bed is studied by coupling with the collisional heat exchange. The correlations for collisional heat transfer are given in Table 7.1.

7.2.4 Geometry and Numerical Strategy

In the present work, the decomposition of biomass and upgrading of bio-oil take place in a fluidized bed reactor while a conical spouted bed reactor was used by Atutxa *et al.* [181]. The 2-D geometry of the reactor is set up with the diameter of 40 mm and the height of 350 mm. Catalyst particles are packed as bed material with the bed height at 800 mm and an initial packing fraction of 0.6. The packed particles are fluidized for 5 s by fluidizing gas from the bottom distributor (inlet0) to the full fluidization state. Then sawdust particles are fed for 2 s from the side injection point (inlet1) by feeding gas. Nitrogen is used as the fluidizing and feeding gas.

The mesh in the computing domain is generated using a grid size of 1 mm, which is sufficient to capture the bed hydrodynamics with grid independence. The velocity-inlet condition is set to the bottom and side injection with velocities of 0.14 and 0.2 $\mathrm{m/s}$ respectively. No-slip boundary conditions are given for all phases. The governing and constitutive equations are solved by finite volume method (FVM). The SIMPLE algorithm is used for pressure-velocity coupling while first upwind scheme for discretisation of convective terms. The time step size is set to 0.0001s and the convergence criterion is 0.001. The simulation was running for the real time of 100s. The operating conditions and solid properties are given in Table 7.2. Cases I-III are set up with the details in Table 7.3.

Table 7.2 Operation condition and solid properties

Property	Value	Unit	Comment
ρ_{cata}	1210	kg/m^3	Catalyst
ρ_{bio}	700	kg/m^3	Sawdust
ρ_{cha}	1100	kg/m^3	Char
w_g	28	g/mol	Molecular weight
w_{sg}	37	g/mol	Molecular weight
w_{tar}	100	g/mol	Molecular weight
u_{sf}	0.14	m/s	Velocity at inlet0
u_{fd}	0.2	m/s	Velocity at inlet1
VF_{bio}	0.08		Volume fraction of sawdust in feeding
T_g	773	K	N_2 temperature
T_{cata}	773	K	Catalyst temperature
T_{bio}	700	K	Sawdust temperature
μ_g	3.7e-5	$kg/(ms)$	Viscosity of N_2
μ_{sg}	3e-5	$kg/(ms)$	Viscosity of gas
μ_{tar}	3e-5	$kg/(ms)$	Viscosity of tar
Cp_{cata}	900	$J/(kgK)$	Specific heat capacity of catalyst
Cp_{bio}	1500	$J/(kgK)$	Specific heat capacity of sawdust
Cp_{cha}	1100	$J/(kgK)$	Specific heat capacity of char
λ_{cata}	0.35	$W/(mK)$	Thermal conductivity of catalyst
λ_{bio}	0.06	$W/(mK)$	Thermal conductivity of sawdust
λ_{cha}	0.071	$W/(mK)$	Thermal conductivity of char
d_{cata}	0.400	mm	Diameter of catalyst
d_{bio}	0.400	mm	Diameter of sawdust
G_{cata}	65	GPa	Elastic modulus
G_{bio}	11	GPa	Elastic modulus
γ_{cata}	0.25		Poisson ratios
γ_{bio}	0.33		Poisson ratios
H_{rec}	0.350	m	Height of reactor
W_{rec}	0.040	m	Width of reactor
H_{bed}	0.080	m	Height of initial bed
H_{fd}	0.040	m	Height of inlet1
d_{fd}	0.004	m	Diameter of inlet1

Table 7.3 Cases setup

Case	Feeding rate (VOF)	Collisional heat exchange
I	0.08	No
II	0.04	No
III	0.08	Yes

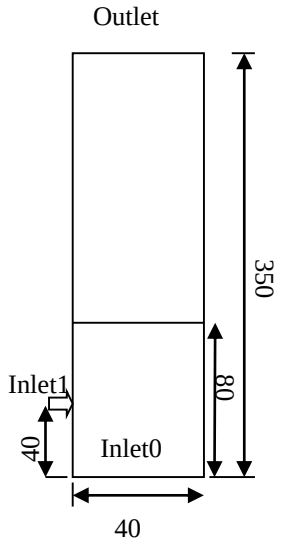

Figure 7.1 Geometry of fluidized bed reactor in 2D (Unit: mm).

7.3 Results and Discussion

7.3.1 Comparison of Different Feeding Rates of Sawdust

Comparison of flow characteristics

Figure 7.2 shows the volume fraction distribution of sawdust in fluidized beds of Cases I and II at 6 to 10 s. Although the feeding rate of sawdust in Case II is half of that in Case I, The high concentration zone can be observed at 6 and 7 s in both Cases whilst the relatively uniform distribution is displayed at 8 and 10 s. The accumulation of sawdust near the sawdust feeding point (Inlet 1) before 7 s is mainly caused by the higher horizontal feeding rate than the dispersion rate with bubbles. After suspending the sawdust feeding, sawdust particles in high concentration zones are transported fast in fluidized beds. The maximum volume fraction of sawdust in beds of Cases I and II decreases quickly from 0.42 to less than

0.05 and 0.04 in one second respectively and the well mixing state is achieved. Due to the efficient and quick circulation of particles in fluidized beds, the formation of cold spots by the accumulation of cold particles can be eliminated in a short time, which is beneficial to maintain the uniform temperature distribution in fluidized beds.

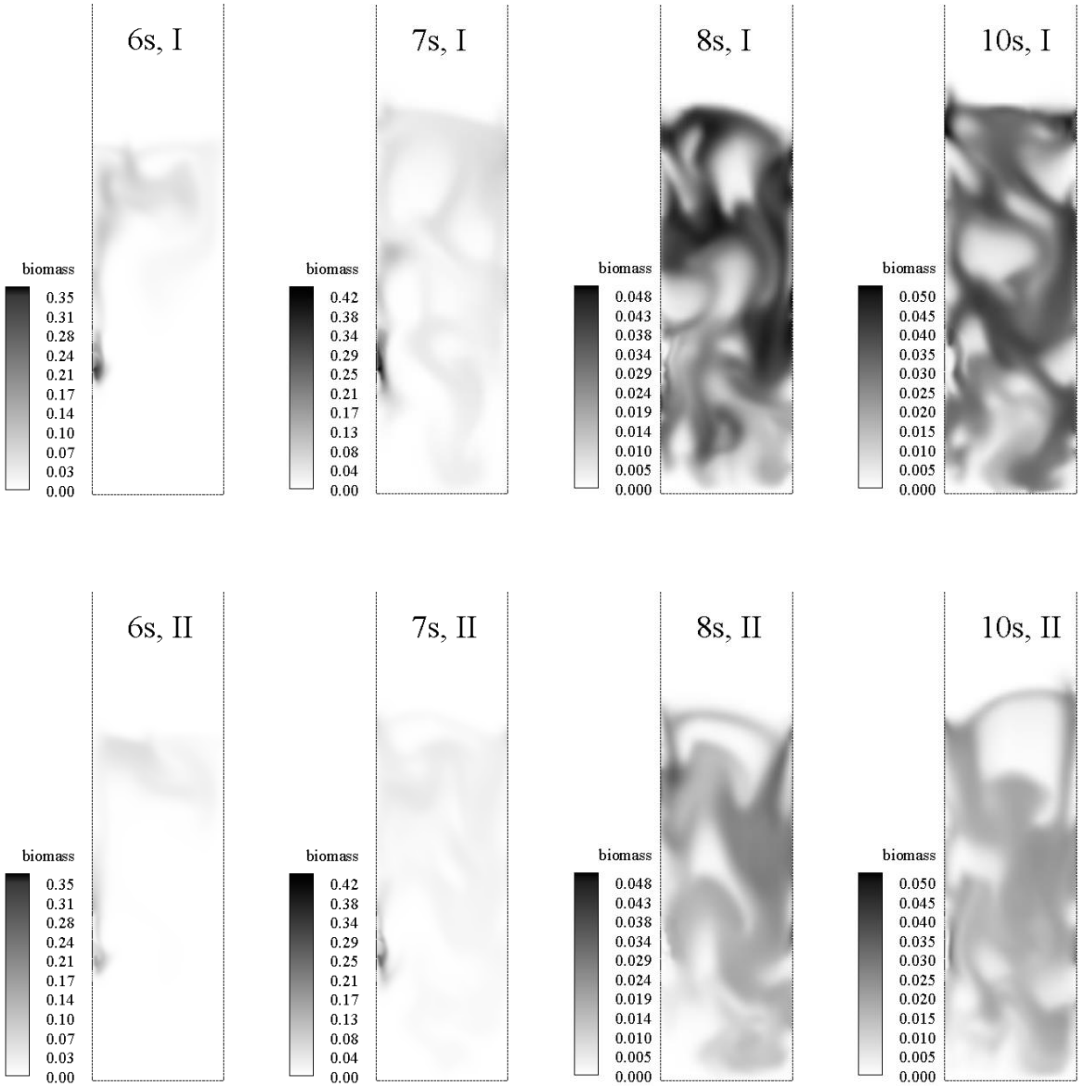

Figure 7.2 Contours of sawdust volume fraction at different time for Cases I and II.

The volumetric flow rates at the Outlet of the fluidized beds in Cases I and II are plotted from 5 to 40 s in Figure 7.3. As the commencement of the side injection from Inlet 1, both the flow rates in two cases increase quickly from the initial value of 0.006 to the peak of 0.011 and 0.008 m^3/s with different sawdust feeding rates at 7 s respectively. The peak value is associated with the maximum mass of sawdust present in beds, where the gas production is the highest from primary reactions of biomass pyrolysis. With the depletion of sawdust, the gas flow rates drop gradually from 7 s. The similar trends are shown for the two cases.

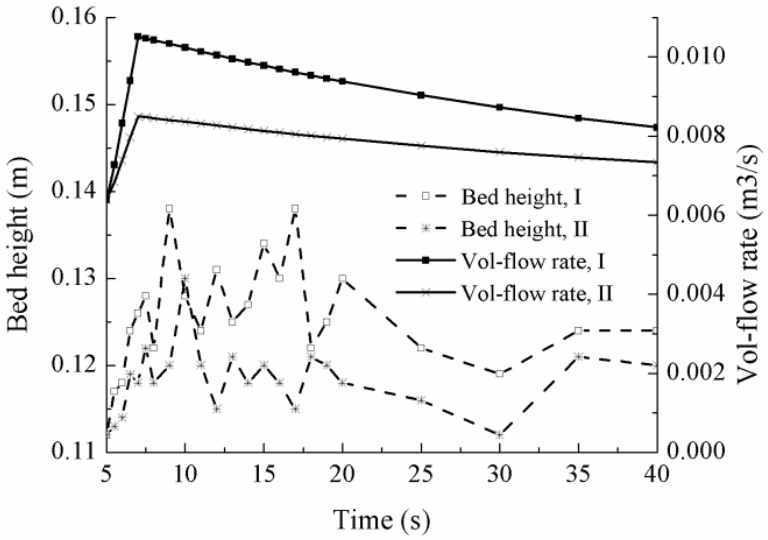

Figure 7.3 Bed height and volumetric flow rate at the reactor outlet by time for Cases I and II.

The heights of the fluidized beds in Cases I and II are also given in Figure 7.3. The sharp growth of bed heights in both cases is performed from 5 s due to the increasing of gas volumetric flow rates. The bigger bed expansion in Case I is because of the presence of higher gas flow rate. In general, the decreasing tendency of bed height can be obtained in time-scale in both cases, which is consistent with the reducing gas flow rate in beds. The gas flow rate is considered as one of the most significant factors for the hydrodynamics of the bubbling fluidized beds. The direct influence is the varying bed height at different flow rates. In the present cases, the gas flow rates in the beds are varied steeply with the additional gas products from pyrolysis of sawdust together with feeding gas injections. Although the

sawdust flow rate decreases to half in Case II, the effects on gas flow rate and bed height are still obvious. The results indicate that the hydrodynamics of fluidized beds can be directly varied by the heterogeneous reactions with gas products. Thus it is difficult to predict the flow pattern in such reacting reactors. A carefully calculated feeding rate is expected to minimize the effects of reactions on fluidized beds.

Yield distribution

Figure 7.4 (a) shows the mass fraction of tar and syngas (gas) in the gas flow at the reactor's Outlets. The steep increasing of flow rates of tar and syngas is noticeable in several seconds in both cases as more and more sawdust samples are present by feeding. The peak points of the curves appear at 10s, which is several seconds later than the suspending time of sawdust feeding. The lagging is caused by the transporting time of gas in reactors. After 10 s, both the flow rates of tar and syngas decrease gradually with time progresses. Especially, the flow rates of tar reduce faster than that of syngas. It can be attributed to the catalytic cracking of tar. As the increasing ratio of catalyst mass to sawdust concentration during depletion of sawdust, the higher ratio enhances the tar cracking with more by-products syngas and char. In Case I, the ratio of mass fraction of tar to syngas is less than 1 after 35 s, which means that the producing rate of syngas becomes higher than that of tar. From the experimental data in Figure 7.4(b), the turning point can be observed at 50 s, when the growth of tar yields is turning to be slower than that of syngas. The results indicate a qualitative consistence between simulation results and experiment data.

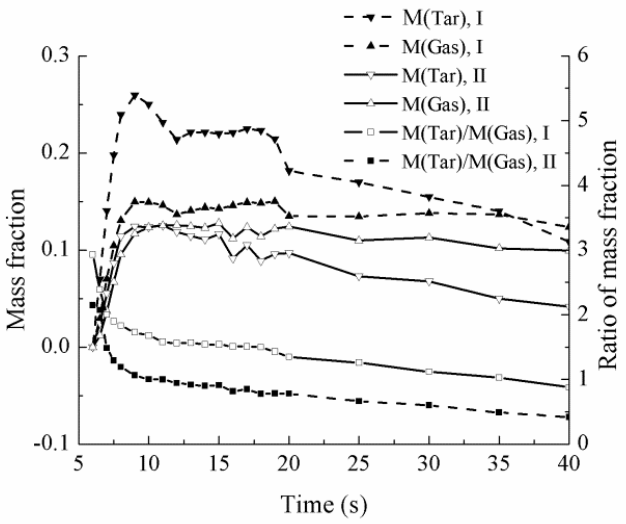

a

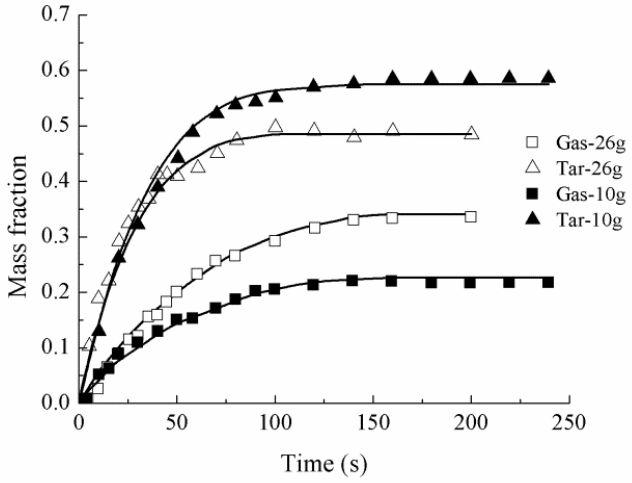

b

Figure 7.4 (a) Mass fraction of tar and syngas and the ratio at outlets in Cases I and II

(b) Evolution of yields of tar and gas by time in experiments [181].

As shown in Figure 7.4(b), the experimental data [181] showed that larger amount of catalyst loaded in reactor (from 10 g to 26 g) leads to higher gas production and lower tar yields. In Case II, less sawdust is fed into reactor, where the mean space time (ratio of catalyst mass to tar flow rate) is bigger than that in Case I. Hence the higher catalytic cracking rate of tar results in lower ratio of mass fraction of tar to syngas and an earlier coming of turning point at 10 s as shown in Figure 7.4 (a). Compared to Case I, the yield

fraction of tar in Case II is less whilst that of syngas is bigger eventually. From the experimental data and simulation results, it is able to deduce that the syngas fraction is increased by consuming more tar with larger space time

7.3.2 Heat Exchange from Bed to Sawdust

In pyrolysis process of biomass, the heating rate is a very important factor for the final product yield distributions. The short heating up period to a certain temperature such as 770 K can give the maximum production of bio-oil [18]. In Case III, heat conduction between catalyst and sawdust phases is introduced together with the heat convection. Higher collision frequency and bigger impact velocity in the upper section of reactor induce a larger heat transfer coefficient between solid phases as shown in Figure 7.5. Compared the data in Figures 7.5(c) and 7.6, the heat transfer coefficients of convection are three orders of magnitude higher than the heat transfer coefficients of conduction. Figure 8 also proves that the heating up processes of cold sawdust particles are not significantly influenced by solid-solid conduction. It can be concluded that the contribution of conduction between catalyst and sawdust phases is negligible in the current case.

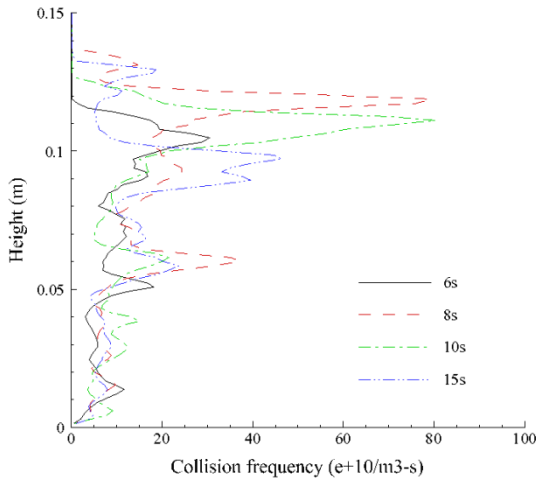

a

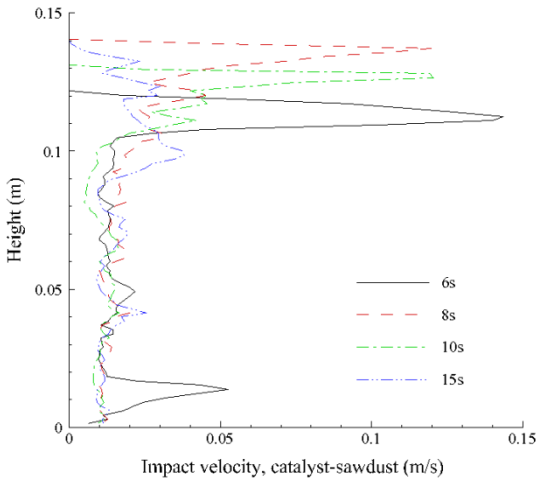

b

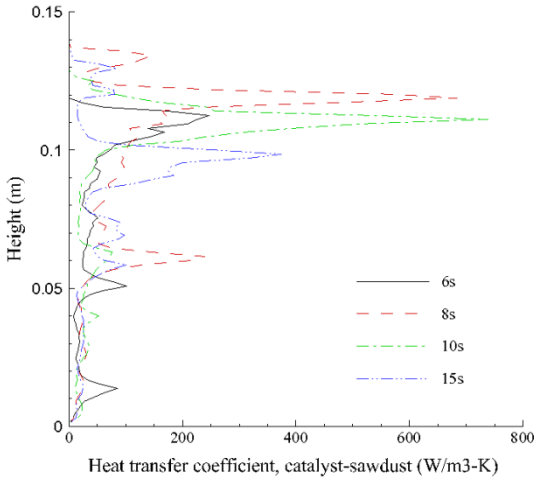

c

Figure 7.5 (a) Average collision frequency with height between solid phases in Case II;

(b) Average impact velocity with height between solid phases in Case II;

(c) Average heat transfer coefficient with height between solid phases in Case II.

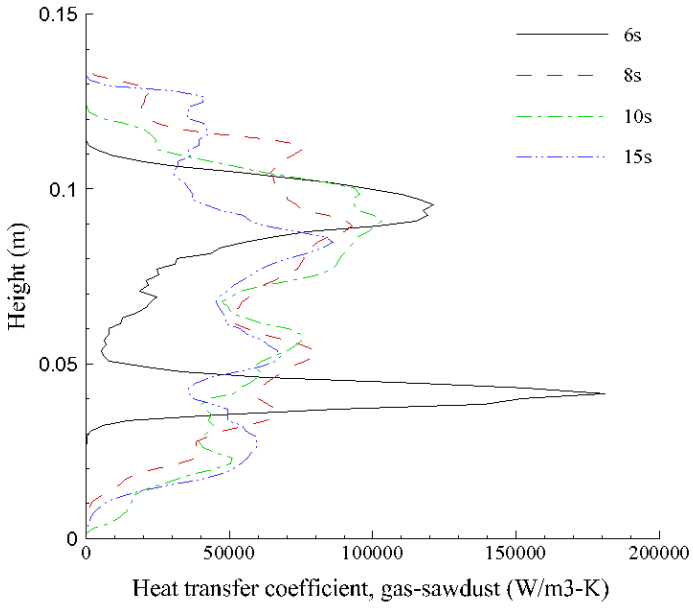

Figure 7.6 Average heat transfer coefficient with height between solid phases in Case II.

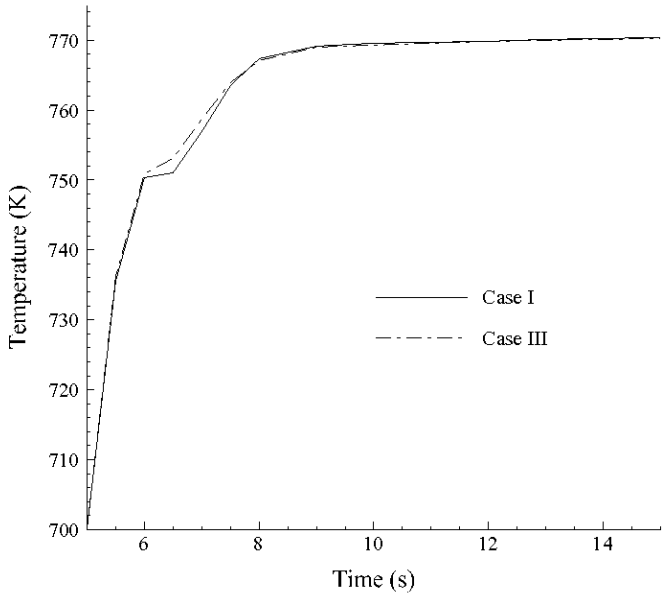

Figure 7.7 Average-temperature evolution of sawdust with time for Cases I and III.

7.4 Conclusions

In this chapter, the numerical simulation is carried out to represent the catalytic pyrolysis of sawdust in fluidized beds. Based on the reaction scheme of sawdust pyrolysis, the results obtained from simulations are qualitatively in agreement with experimental work. The results can be concluded as follows:

The heterogeneous reactions taking place in reacting reactors can influence the hydrodynamics of fluidized bed. The bed height of fluidized bed is varied significantly as chemical reactions take place and a large amount of gas produced. The mass flow rate of biomass needs to be carefully considered to minimize the effects and achieve the predictable influence on the flow pattern of reacting beds;

In the upgrading reaction, the local ratio of catalyst mass to tar flow rate (space time) dominates the catalytic cracking progress. An appropriate space time can balance the quality and production of tar, because large space time causes over cracking of tar into syngas and

char which eventually results in a low tar yield. Changing of hydrodynamics can give direct effects on mass distribution and velocity field which varies the space time correspondingly;

The simulation results prove the negligible contribution on heating up of cold sawdust particles via direct heat exchange from the catalyst, as the heat transfer between solid phases is much smaller than that between gas and solid phases.

Chapter 8: Conclusions

8.1 Overall Conclusions

The conclusions derived throughout the thesis are summarized in this chapter. The main purpose of the project is constructing a numerical model to represent the thermo-chemical processes in biomass pyrolysis. The study was started from the heat transfer and hydrodynamics of multiphase flow. The fast pyrolysis and catalytic pyrolysis are then investigated by incorporating the kinetic schemes into the model of cold fluidised beds. Finally, reacting multiphase flow in fluidized beds are studied in detail.

Heat exchange in the fluidised beds is one of the challenging topics in multiphase flow studies. Although displaying the steady temperature field is not difficult by a measurement device, the instantaneous heat transfer is not easy or impossible to capture. In Chapter 4, heat transfer from a hot tube surface to a multiphase flow is investigated. An optimized model is introduced by using the effective thermal conductivities of gas and solid to improve the accuracy of heat transfer coefficients in prediction. Two simulations are carried out by using tubes with different shapes. The square tube influences the hydrodynamics more than the circular tube and reaches the minimum fluidization point later. A larger build-up of air below the flatter base of the tube forms larger coalescing bubbles and a subsequent increase of bed expansion. The simulation results indicate that the distribution of local instantaneous heat transfer coefficients is sensitive to the hydrodynamics of the beds and varies significantly with the local flow pattern in the fluidisation. The time-mean values of heat transfer coefficients calculated by the effective thermal conductivity are over-predicted compared with the experimental work. More detailed models which consider the porosity between the packed particles around a tube would improve the accuracy of the numerical models.

Hydrodynamics of fluidised beds describes the gas and solids interactions and solids circulation in the fluidised beds. Gas and solids distribution affects the heating up of immersed objects and the reactions related to heat exchange. The flow pattern of binary mixtures in gas-solid bubbling fluidized beds is represented in Chapter 5 with Eulerian approaches. Two systems with particles with density difference and size difference were studied. In this work, the grid independence is tested with different grid size which can reduce the error in modelling. The simulations show that the radial distribution function shows negligible influence on the prediction of mixing and segregation equilibrium however the flow pattern are sensitive to the coefficient of restitution close to 1. Bed height and mixing index are employed to qualify the flow pattern changing. The relevant results indicate that solids with different densities segregate easily in bubbling fluidized beds with low superficial velocity which can be well captured in simulations. Although the binary mixtures with size difference separate partially in the simulation, the segregation efficiency is much lower than that in realistic conditions. The model for segregation of particles with different sizes needs to be improved. The general consistence can be obtained that the increasing superficial velocity rebuilds the balance of mixing and segregation into well mixing state.

Based on the studies of heat transfer and hydrodynamics of multiphase flow in the fluidised beds, the fast pyrolysis of biomass is modelled with similar approaches. The effects of different superficial velocities on hydrodynamics of fluidized beds and the chemical reactions are discussed. Rapid char removal from the beds is necessary to prevent tar cracking in contacts of pyrolytic vapours and char. The lower level intensity of fluidisation leads to higher tar yields but the char particles may not be separated out effectively as shown in simulations. The other contribution of this work is incorporating an empirical correlation into the kinetic scheme to describe the effects of heat conduction internal particles on chemical reactions. Generally, the internal conduction is negligible for particles in Geldart group B. Therefore, consideration of heat conduction needs to be

carried out for larger particles as introduced in this work. The sensitivity of the employed correlation is discussed by incorporating into modelling the fast pyrolysis of particles of different sizes. The simulation results reveal that the modification of kinetics on the second step shows more sensitivity than that on the first step. Meanwhile the implementation of the correlation for internal particle conduction delivers a similar trend to experiments qualitatively. The outflow boundary condition is recommended to define the outlet where the solids leave through.

The modelling of reacting multiphase flow in a fluidized bed is also carried out to represent the catalytic pyrolysis of sawdust samples. Although the binary mixture of sand and catalyst is not loaded but a pure catalyst bed, different feeding rates of sawdust samples are introduced into modelling to investigate the connection between space time and final frictional yield distributions. By incorporating the kinetics for catalytic pyrolysis, the simulation results show that heterogeneous reactions influence the flow pattern of fluidized bed by the amount of gas production. Mass flow rate has to be defined cautiously to achieve the predictable results. The qualitative consistence between simulations and experiments gives a proof that the introduced kinetics can describe the catalytic pyrolysis of sawdust modestly. The relation of space time and end-product distribution can be addressed. The contribution on heating up of cold sawdust particles via direct heat exchange from the catalyst is proved to be ignorable by a case study, as the heat transfer between solid phases is much smaller than that between gas and solid phases.

8.2 Future Work

As reported in previous chapters, numerical studies of fast pyrolysis or catalytic pyrolysis are still in the early stage. Compared to extensive experimental studies, limited numerical works have been conducted. Recently, pyrolysis systems in large scale have been built by several companies. In this context, the new challenge is that large-scale simulations require high computational intensity. Hence optimization of numerical approaches and methods needs to be carried out for industrial scale problems. For instance, improving the

drag functions for multiphase flow in dilute regime can loosen limitation of the grid size by particle diameters.

To improve the present work, several aspects can be pursued as follows:

Optimizing the model for heat transfer

As introduced above, the implementation of effective thermal conductivity can improve the accuracy in predicting the heat transfer coefficients. However the simulation results show that the predicted heat transfer coefficient is still not well matched the values from the experiments. New or improved models or correlations need to be introduced to reduce the error.

Optimizing the drag functions

Representing the bubbling frequency and size numerically is still a challenge at present. Meanwhile the simulation results from the present study show that the segregation of different sized solids in Geldart group B is difficult to be captured. The problem is regarded to derive from the models for the consideration of solid-solid interactions. More accurate solid-solid drag functions need to be introduced and tested.

Optimizing the reaction description

In the current work, the phenomena of shrinkage fragmentation and porous structure during reaction are not studied, which can be considered later. Furthermore the moisture evaporation from inner particles and size distribution of samples can also be address by empirical correlations similar to the internal conduction description.

Validation of turbulence model

The studies in literature always employ the existing turbulence models into multiphase flow however the validation is rarely discussed. More work need to be finished on checking the existing model or developing a new one.

Bibliography

[1] Zhang Q, Chang J, Wang T, Xu Y. Review of biomass pyrolysis oil properties and upgrading research. Energy Conversion and Management. 2007;48:87-92.

[2] David AL, Robert CB, James E, Johannes L. Review of the pyrolysis platform for coproducing bio-oil and biochar. Biofuels, Bioproducts & Biorefining. 2009;3:547-62.

[3] Bridgwater AV. Renewable fuels and chemicals by thermal processing of biomass. Chemical Engineering Journal. 2003;91:87-102.

[4] Maniatis K. Progress in Biomass Gasification: An Overview. In: Bridgwater AV, editor. Progress in Thermochemical Biomass Conversion. Oxford, UK: Blackwell Science Ltd; 2008.

[5] Maschio G, Koufopanos C, Lucchesi A. Pyrolysis, a promising route for biomass utilization. Bioresource technology. 1992;42:219-31.

[6] Bridgwater AV. Review of fast pyrolysis of biomass and product upgrading. Biomass and Bioenergy. 2012;38:68-94.

[7] Demirbas A, Arin G. An overview of biomass pyrolysis. Energy Source. 2002;24:471-82.

[8] Bridgwater AV, Peacocke GVC. Fast pyrolysis processes for bomass. Renewable & Sustainable Energy Reviews. 2000;4:1-73.

[9] Peng WM, Wu QY. Production of Fuels from Biomass Pyrolysis. New Energy Source. 2000;22:39-44.

[10] Oasmaa A, Czernik S. Fuel Oil Quality of Biomass Pyrolysis Oils-state of the Art for the End-users. Energy Fuels. 1999;13:914-21.

[11] Michio I, Maria S, Hogan E. Emulsification of pyrolysis derived bio-oil in diesel fuel. Biomass and Bioenergy. 2003;24:221-31.

[12] Bridgwater AV. Production of high grad fuels and chemicals from catalytic pryolysis of biomass. Catalytic Today. 1996;29:285-95.

[13] Uzun BB, Sarioğlu N. Rapid and catalytic pyrolysis of corn stalks. Fuel Processing Technology. 2009;90:705-16.

[14] Zhang H, Xiao R, Huang H, Xiao G. Comparison of non-catalytic and catalytic fast pyrolysis of corncob in a fluidized bed reactor. Bioresource technology. 2009;100:1428-34.

[15] Williams PT, Nugranad N. Comparison of Products from the Pyrolysis and Catalyst Pyrolysis of Rice Husks. Energy. 2000;25:493-513.

[16] Ragnar W. Gasification of biomass: comparison of fixed bd and fluidized bed gasifier. Biomass and Bioenergy. 2000;18:489-97.

[17] Diblasi C. Modeling chemical and physical processes of wood and biomass pyrolysis. Progress in Energy and Combustion Science. 2008;34:47-90.

[18] Bridgwater AV, Meier D, Radlein D. An Overview of Fast Pyrolysis of Biomass. Organic Geochemistry. 1999;30:1479-93.

[19] Shafizadeh F, Chin Peter P S. Thermal deterioration of wood. Wood Technology:Chemical Aspects: Amercian Chemical Society; 1977. p. 57-81.

[20] Bradbury AGW, Sakai Y, Shafizadeh F. A kinetic model for pyrolysis of cellulose. Journal of Applied Polymer Science. 1979;23:3271-80.

[21] Branca C, Di Blasi C. Kinetics of the isothermal degradation of wood in the temperature range 528–708 K. J Anal Appl Pyrol 2003;67:207-19.

[22] Maschio G, Lucchesi A, Koufopanos C. Study of kinetic and transfer phenomena in the pyrolysis of biomass particles. In: Bridgwater AV, editor. Advances in thermochemical biomass conversion. London: Blackie Academic & Professional; 1994. p. 746-59.

[23] Miller RS, Bellan J. A generalized biomass pyrolysis model based on superimposed cellulose, hemicellulose and lignin kinetics. Combust Sci Technol 1996;126:97-137.

[24] Geldart D. Types of gas fluidization. Powder technol. 1973;7:285-92.

[25] Shen DK, Gu S, Jin B, Fang MX. Thermal degradation mechanisms of wood under inert and oxidative environments using DAEM methods. Bioresource technology. 2011;102:2047-52.

[26] Zhou H, Long Y, Meng A, Li Q, Zhang Y. The pyrolysis simulation of five biomass species by hemi-cellulose, cellulose and lignin based on thermogravimetric curves. Thermochimica Acta. 2013;566:36-43.

[27] Lathouwers D, Bellan J. Modeling of dense gas–solid reactive mixtures applied to biomass pyrolysis in a fluidized bed. Int J Multiphase Flow. 2001;27:2155-87.

[28] Maggi R, Delmon B. Comparison Between Slow and Fast Pyrolysis Oils From Biomass. Fuel. 1994;73:671-7.

[29] Onay O, Kockar OM. Slow, Fast and Flash Pyrolysis of Rapeseed. Renewable Energy. 2003;28.

[30] van der Hoef MA, van Sint Annaland M, Deen NG, Kuipers JAM. Numerical Simulation of Dense Gas-Solid Fluidized Beds: A Multiscale Modeling Strategy. Annual Review of Fluid Mechanics. 2008;40:47-70.

[31] Van der Hoef MA, Van Sint Annaland M, Kuipers JAM. Computional fluid dynamics for dense gas-solid fluidized beds: a multi-scale modelling stradgy. China Particuology. 2005;3:69-77.

[32] Bruchmuller J, van Wachem BGM, Gu S, Luo KH, Brown RC. Modeling the Thermochemical Degrading of Biomass Inside a Fast Pyrolysis Fluidized Bed Reactor. J AIChE. 2012;58:3030-42.

[33] Lu HL, Shen ZH, Ding J, Min, Li X, Liu HP. Numerical simulation of bubble and particles motions in a bubbling fluidized bed using direct simulation Monte-Carlo method. Powder Technology. 2006;169:159-71.

[34] Min J, Drake JB, Heindel TJ, Fox RO. Experimental validation of CFD simulations of a lab-scale fluidized-bed reactor with and without side-gas injection. AIChE Journal. 2009:NA-NA.

[35] van Wachem BGM, Schouten JC, van den Bleek CM, Krishna R, Sinclair JL. Comparative analysis of CFD models of dense gas solid systems. AIChE Journal. 2001;47:1035-51.

[36] Wang J, Liu Y. EMMS-based Eulerian simulation on the hydrodynamics of a bubbling fluidized bed with FCC particles. Powder Technology. 2010;197:241-6.

[37] Wang J, van der Hoef MA, Kuipers JAM. Coarse grid simulation of bed expansion characteristics of industrial-scale gas–solid bubbling fluidized beds. Chemical Engineering Science. 2010;65:2125-31.

[38] Ye M, Wang J, van der Hoef MA, Kuipers JAM. Two-fluid modeling of Geldart A particles in gas-fluidized beds. Particuology. 2008;6:540-8.

[39] Yu L, Lu J, Zhang X, Zhang S. Numerical simulation of the bubbling fluidized bed coal gasification by the kinetic theory of granular flow (KTGF). Fuel. 2007;86:722-34.

[40] Zhang K, Wu G, Brandani S, Chen H, Yang Y. CFD simulation of dynamic characteristics in liquid–solid fluidized beds. Powder Technology. 2012;227:104-10.

[41] Zhang MH, Chu KW, Wei F, Yu AB. A CFD–DEM study of the cluster behavior in riser and downer reactors. Powder Technology. 2008;184:151-65.

[42] Zhou H, Flamant G, Gauthier D. DEM-LES of coal combustion in a bubbling fluidized bed. Part I: gas-particle turbulent flow structure. Chemical Engineering Science. 2004;59:4193-203.

[43] Zhu HP, Zhou ZY, Yang RY, Yu AB. Discrete particle simulation of particulate systems: Theoretical developments. Chemical Engineering Science. 2007;62:3378-96.

[44] Cundall PA, Strack ODL. A discrete numercial model for granular assemblies. Geotechnique. 1979;21:47-65.

[45] Tsuji Y, Kawaguchi T, Tanaka T. Discrete particle simulation of two-dimentional fluidized bed. Powder technol. 1993;77:79-87.

[46] Hoomans BPB, Kuipers JAM, Briels WJ, Van Swaaij WPM. Discrete particle simulation of bubble and slug formation in a two-dementional gas-fluidised bed: a hard-sphere approach. chemical Engineering Science. 1996;51:99-118.

[47] Deen NG, Van Sint Annaland M, Van der Hoef MA, Kuipers JAM. Review of discrete particle modeling of fluidised beds. Chemcial Engineering Science. 2007;62:28-44.

[48] Luding S. Introduction to discrete element methods. European Journal of Environmental and Civil Engineering. 2008;12:785-826.

[49] S. L, Goldshtein A. Collisional cooling with multi-paticle interactions. Granular Matter. 2003;5:159-63.

[50] Lu H, Wang S, Zhao Y, Liu Y, Gidaspow D, Ding J. Prediction of particle motion in a two-dimensional bubbling fluidized bed using discrete hard-sphere model. Chemical Engineering Science. 2005;60:3217-31.

[51] Limtrakul S, Chalermwattanatai A, Unggurawirote K, Tsuji Y, Kawaguchi T, Tanthapanichakoon W. Discrete particle simulation of solids motion in a gas-solid fluidized bed. Chemical Engineering Science. 2003;58:915-21.

[52] Wang XS, Rhodes MJ. Determination of particle residence time at the wall of gas fluidized beds by discrete element method simulation. Chemical Engineering Science. 2003;58:387-95.

[53] De Jong JF, Dang TYN, Van Sint Annaland M, Kuipers JAM. Comparison of a discrete particle model and a tow-fluid model to experiments of a fluidized bed with flat membranes. Power Technology. 2012;230:93-105.

[54] Oevermann M, Gerber S, Behrendt F. Euler-Lagrange/DEM simulation of wood gasification in a bubbling fluidized bed reactor. Particuology. 2009;7:307-16.

[55] Zhou H, Flamant G, Gauthier D, Flitris Y. Simulation of coal combustion in a bubbling fluidized bed by distinct element method. Trans Inst Chem Eng. 2003;81:1144-9.

[56] Anderson TB, Jackson R. Fluid mechanicial description of fluidised beds: equations of motion Ind Eng Chem Fundam. 1967;6:527-39.

[57] Chapman S, Cowling TG. The mathematical theory of non-uniform gases. 3d ed. Cambridge: Cambridge University Press; 1970.

[58] Ding J, Gidaspow D. A bubbling fluidization model using kinetic theory of granular flow. J AIChE. 1990;36:523-38.

[59] Lun CKK, Savage SB, Jeffrey DJ, Chepurniy N. Kinetic theories for granular flow: inelastic particles in couette flow and slightly inelastic particles in a general flow field. J Fluid Mech. 1984;140:223-56.

[60] Gidaspow D, Bezburuah R, Ding J. Hydrodynamics of circulating fluidized beds: Kinetic theory approach. the 7th Fluidization Conference1992.

[61] Ergun S. Fluid flow through packed columns. ChemEngProgr. 1952;48:89-94.

[62] Wen CY, Yu YH. Mechanics of fluidization. CEP Symposium Series1966. p. 100-11.

[63] Syamlal M, O'Brien TJ. Derivation of a drag coefficient from velocity-voidage correlation. Morgantown, Virginia: US dept of Energy, Office of Fossil Energy, National Energy Technology Lab; 1987.

[64] Arastoopour H, Pakdel P, Adewumi M. Hydrodynamic analysis of dilute gas-solids flow in a vertical pipe. Powder technol. 1990;62:163-70.

[65] Ramesh PLN, Raajenthiren M. A review of some existing drag models describing the interaction between the solid gaseous phases in CFB. international Journal of Engineering Science and Technology. 2010;2:1047-51.

[66] Boemer A, Qi H, Renz U, Vasquez S, Boysan F. Eulerian computation of fluidised bed hydrodynamics: a comparison of physical models. The 13th International conference on fluidized bed combustion. Orlando,USA1995. p. 775-86.

[67] Chiesa M, Mathiesen V, Melleim JA, Halvorsen B. Numercial simulation of paticulate flow by the Eulerian-Lagrangian and the Eulerian-Eulerian approach with application to a fluidized bed. Computers & Chemical Engineering. 2005;29:291-304.

[68] Botterill JSM. Fluid-bed Heat Transfer. New York: Academic Press; 1975.

[69] Yates JG. Fundamentals of fluidised bed chemical precesses. London: Butterworths; 1983.

[70] Parmar MS, Hayhurst AN. The heat transfer coefficient for a freely moving sphere in a bubbling fluidised bed. Chemical Engineering Science. 2002;57:3458-94.

[71] Collier AP, Hayhurst AN, Richardson JL. The heat transfer coefficient between a particle and a bed(packed or fluidised) of much larger particles. Chemical Engineering Science. 2004;59:4613-20.

[72] Di Natale F, Lancia A, Nigro R. A single particle model for surface-to-bed heat transfer in fluidized beds. Powder Technology. 2008;187:68-78.

[73] Di Natale F, Lancia A, Nigro R. Surface-to-bed heat transfer in fluidised beds: Effect of surface shape. Powder Technology. 2007;174:75-81.

[74] Mickley HS, Fairbanks DF. Mechanism of heat transfer to fluidized beds. J AIChE 1955;3:374-84.

[75] Kuipers JAM, Prints W, van Swaaij WPM. Numercial calculation of wall-to-bed heat-transfer-coefficients in gas-fluidized beds. J AIChE. 1992;38:1079-91.

[76] Schmidt A, Renz U. Eulerian computation of heat transfer in fluidized beds. Chemical Engineering Science 1999;54:5515-22.

[77] Armstrong LM, Gu S, Luo KH. The influence of multiple tubes on the tube-to-bed heat transfer in a fluidized bed. International Journal of Multiphase Flow. 2010;36:916-29.

[78] Patil DJ, Smit J, van Sint Annaland M, Kuipers JAM. Wall-to-bed heat transfer in gas-solid bubbling fluidized bed. J AIChE 2006;52:58-74.

[79] Armstrong LM, Gu S, Luo KH. Study of wall-to-bed heat transfer in a bubbling fliudized bed using the kinetic theory of granular flow. Int J of heat and mass transfer. 2010;53:4949-59.

[80] Yusuf R, Halvorsen B, Melaaen MC. Eulerian-Eulerian simulation of heat transfer between a gas-solid fluidized bed and an immersed tube-bank with horizontal tubes. Chemical Engineering Science. 2011;66:1550-64.

[81] Littman H, Barile RG, Pulsifer AH. Gas-particle heat transfer coefficients in packed beds at low Reynolds numbers. I&EC Fundamentals. 1968;7:554-61.

[82] Gunn DJ, De Souza JFC. Heat transfer and axial dispersion in packed beds. Chem Eng Sci. 1974;29:1363-71.

[83] Kunii D, Suzuki M. Particle to fluid heat and mass transfer in packed beds of fine particles. Int J Heat Mass transfer. 1967;10:845-52.

[84] Gunn DJ. Transfer of heat or mass to particles in fixed and fluidized beds. Int J Heat Mass transfer. 1978;21:467-76.

[85] Chang J, Wang G, Gao J, Zhang K, Chen H, Yang Y. CFD modeling of particle–particle heat transfer in dense gas-solid fluidized beds of binary mixture. Powder Technology. 2012;217:50-60.

[86] Chang J, Yang S, Zhang K. A particle-to-particle heat transfer model for dense gas–solid fluidized bed of binary mixture. Chemical Engineering Research and Design. 2011;89:894-903.

[87] Di Maio FP, Di Renzo A, Trevisan D. Comparison of heat transfer models in DEM-CFD simulations of fluidized beds with an immersed probe. Powder Technology. 2009;193:257-65.

[88] Botterill JSM, Williams JR. The mechanism of heat transfer to gas fluidized beds Trans Inst Chem Eng. 1963;41:217-31.

[89] Yang S, Luo K, Fang M, Fan J. Discrete element simulation of the hydrodynamics in a 3D spouted bed: Influence of tube configuration. Powder Technology. 2013;243:85-95.

[90] Luo K, Fang M, Yang S, Zhang K, Fan J. LES–DEM investigation of an internally circulating fluidized bed: Effects of gas and solid properties. Chemical Engineering Journal. 2013;228:583-95.

[91] Ku X, Li T, Løvås T. Influence of drag force correlations on periodic fluidization behavior in Eulerian–Lagrangian simulation of a bubbling fluidized bed. Chemical Engineering Science. 2013;95:94-106.

[92] Benyahia S, Syamlal M, O'Brien TJ. Evaluation of boundary conditions used to model dilute, turbulent gas/solids flows in a pipe. Powder Technology. 2005;156:62-72.

[93] Li T, Zhang Y, Grace JR, Bi X. Numerical investigation of gas mixing in gas-solid fluidized beds. AIChE Journal. 2010:NA-NA.

[94] Li T, Grace J, Bi X. Study of wall boundary condition in numerical simulations of bubbling fluidized beds. Powder Technology. 2010;203:447-57.

[95] Lan X, Xu C, Gao J, Al-Dahhan M. Influence of solid-phase wall boundary condition on CFD simulation of spouted beds. Chemical Engineering Science. 2012;69:419-30.

[96] Chen X, Shi D, Gao X, Luo Z. A fundamental CFD study of the gas–solid flow field in fluidized bed polymerization reactors. Powder Technology. 2011;205:276-88.

[97] Zhang H, Shao S, Xiao R, Pan QW, Chen R, Jubing Z. Nmuerical study on the hydrodynamics of a self-heating biomass fast pyrolysis reactor. Energy&fuels. 2011;25:4077-84.

[98] Li Y, Che D, Liu Y. CFD simulation of hydrodynamic characteristics in a multiple-spouted bed. Chemical Engineering Science. 2012;80:365-79.

[99] Zhang K, Pei P, Brandani S, Chen H, Yang Y. CFD simulation of flow pattern and jet penetration depth in gas-fluidized beds with single and double jets. Chemical Engineering Science. 2012;68:108-19.

[100] He Y, Zhan W, Zhao Y, Lu H, Schlaberg I. Prediction on immersed tubes erosion using two-fluid model in a bubbling fluidized bed. Chemical Engineering Science. 2009;64:3072-82.

[101] van Wachem BGM, Schouten JC, Krishna R, van den Bleek CM. Validation of the eulerian simulated dynamic behavior of gas solid fluidised beds. Chem Eng Sci. 1999;54:2141-9.

[102] Pain CC, Mansoorzadeh S, Gomes JLM, de Oliveira CRE. A numerical investigation of bubbling gas solid fluidized bed dynamics in 2D geometries. Powder technol. 2002;128:56-77.

[103] Lu H, Wang S, Zheng J, Gidaspow D, Ding J, Li X. Numerical simulation of flow behavior of agglomerates in gas–cohesive particles fluidized beds using agglomerates-based approach. Chemical Engineering Science. 2010;65:1462-73.

[104] Wang S, Liu G, Lu H, Xu P, Yang Y, Gidaspow D. A cluster structure-dependent drag coefficient model applied to risers. Powder Technology. 2012;225:176-89.

[105] Wang S, Lu H, Gao J, Lu H, Liu G, Xu P, et al. CFD simulation of gas–solid flow with a cluster structure-dependent drag coefficient model in circulating fluidized beds. Applied Mathematical Modelling. 2013;37:8179-202.

[106] Wang S, Lu H, Liu G, Sheng Z, Xu P, Gidaspow D. Modeling of cluster structure-dependent drag with Eulerian approach for circulating fluidized beds. Powder Technology. 2011;208:98-110.

[107] Hong K, Wang W, Zhou Q, Wang J, Li J. An EMMS-based multi-fluid model (EFM) for heterogeneous gas–solid riser flows: Part I. Formulation of structure-dependent conservation equations. Chemical Engineering Science. 2012;75:376-89.

[108] Wang J, Zhou Q, Hong K, Wang W, Li J. An EMMS-based multi-fluid model (EFM) for heterogeneous gas–solid riser flows: Part II. An alternative formulation from dominant mechanisms. Chemical Engineering Science. 2012;75:349-58.

[109] Shi Z, Wang W, Li J. A bubble-based EMMS model for gas–solid bubbling fluidization. Chemical Engineering Science. 2011;66:5541-55.

[110] Gao X, Wu C, Cheng Y-w, Wang L-j, Li X. Experimental and numerical investigation of solid behavior in a gas–solid turbulent fluidized bed. Powder Technology. 2012;228:1-13.

[111] Li J, Luo Z, Lan X, Xu C, Gao J. Numerical simulation of the turbulent gas–solid flow and reaction in a polydisperse FCC riser reactor. Powder Technology. 2013;237:569-80.

[112] Yan W, Li J, Luo Z. A CFD-PBM coupled model with polymerization kinetics for multizone circulating polymerization reactors. Powder Technology. 2012;231:77-87.

[113] Yan W, Luo Z, Guo A. Coupling of CFD with PBM for a pilot-plant tubular loop polymerization reactor. Chemical Engineering Science. 2011;66:5148-63.

[114] Chen X, Luo Z, Yan W, Lu Y, Ng IS. Three-dimensional CFD-PBM coupled model of the temperature fields in fluidized-bed polymerization reactors. AIChE Journal. 2011;57:3351-66.

[115] Yan W, Luo Z, Lu Y, Chen X. A CFD-PBM-PMLM integrated model for the gas-solid flow fields in fluidized bed polymerization reactors. AIChE Journal. 2012;58:1717-32.

[116] Peirano E, Delloume V, Leckner B. Two- or three-dimensional simulations of turbulent gas-solid flows applied to fluidization. Chemical Engineering Science. 2001;56:4787-99.

[117] Xie N, Battaglia F, Pannala S. Effects of using two- versus three-dimentional computational modelling of fluidized beds. Powder Technoloy. 2008;182:1-13.

[118] Papadikis K, Bridgwater AV, Gu S. CFD modelling of the fast pyrolysis of biomass in fluidised bed reactors, Part A: Eulerian computation of momentum transport in bubbling fluidised beds. Chemical Engineering Science. 2008;63:4218-27.

[119] Zhang HY, Xiao R, Wang DH, Zhong ZP, Song M, Pan QW, et al. Catalytic fast pyrolysis of biomass in a fluidized bed with fresh and spent fluidized bed catalytic cracking catalysts. Energy & Fuels. 2009;23:6199-206.

[120] Rasul MG, Rudolph V, Carsky M. Segregation potential in binary gas fluidized beds. Powder Technology. 1999;103:175-81.

[121] Peng Z, Elham D, Yusif AA, Behdad M. Mixing and segregation of solid mixtures in bubbling fliudized beds under conditions pertinent to fuel reactor of a chemical looping system. Powder technol. 2013;235:823-37.

[122] Yusif AA, Elham D, Behdad M. Mixing and segregation of binary oxygen carrier mixutres in a cold flow model of a chemical looping combustor. Chem Eng Sci. 2013;223:772-84.

[123] Oliveira TJP, Cardoso CR, Ataide AH. Bubbling fluidization of biomass and sand binary mixtures: minimum fluidization velocity and particle segregation. chemical Engineering and Processing: Process Intensification. 2013;72:113-21.

[124] Wu SY, Baeyens J. Segregation by size difference in gas fluidized beds. Powder Technology. 1998;98:139-50.

[125] Lu H, He Y, Gidaspow D, Yang L, Qin Y. Size segregation of binary mixture of solids in bubbling fluidized beds. Powder Technology. 2003;134:86-97.

[126] Lu H, Zhao Y, Ding J, Gidaspow D, Li W. Investigation of mixing/segregation of mixture particles in gas–solid fluidized beds. Chemical Engineering Science. 2007;62:301-17.

[127] Chao Z, Wang Y, Jakobsen JP, Fernandino M, Jakobsen HA. Investigation of the particle–particle drag in a dense binary fluidized bed. Powder Technology. 2012;224:311-22.

[128] Cooper S, Coronella CJ. CFD simulations of particle mixing in a binary fluidized bed. Powder Technology. 2005;151:27-36.

[129] Feng YQ, Xu BH, Zhang SJ, Yu AB. Discrete particle simulation of gas fluidization of particle mixtures. J AIChE. 2004;50:1713-28.

[130] Feng YQ, Yu AB. Discrete particle simulation of size segregation of particle mixtures in a gas fluidized bed. China Particuology. 2006;4:122-6.

[131] Makkawi YT, Wright PC. The voidage function and effective drag force for fluidized beds. Chemical Engineering Science. 2003;58:2035-51.

[132] Das M, Banerjee M, Saha RK. Segregation and mixing effects in the riser of a circulating fluidized bed. Powder Technology. 2007;178:179-86.

[133] Das M, Meikap B, Saha R. Characteristics of axial and radial segregation of single and mixed particle system based on terminal settling velocity in the riser of a circulating fluidized bed. Chemical Engineering Journal. 2008;145:32-43.

[134] Gao JS, Lan XY, Fan YP, Chang J, Wang G, Lu CX, et al. Hydrodynamics of gas–solid fluidized bed of disparately sized binary particles. Chemical Engineering Science. 2009;64:4302-16.

[135] Lan X, Yan W, Xu C, Gao J, Luo Z-H. Hydrodynamics of gas–solid turbulent fluidized bed of polydisperse binary particles. Powder Technology. 2014;262:106-23.

[136] Palappan KG, Sai PST. Studies on segregation of binary mixture of solids in continuous fast fluidized bed. Chemical Engineering Journal. 2008;139:330-8.

[137] Ren B, Shao Y, Zhong W, Jin B, Yuan Z, Lu Y. Investigation of mixing behaviors in a spouted bed with different density particles using discrete element method. Powder Technology. 2012;222:85-94.

[138] Wang Z, Cheng Z, Yuan W, Cai J, Zhang L, Zhang F, et al. An experimental and kinetic modeling study of cyclohexane pyrolysis at low pressure. Combustion and Flame. 2012;159:2243-53.

[139] Zhang Y, Cai J, Zhao L, Yang J, Jin H, Cheng Z, et al. An experimental and kinetic modeling study of three butene isomers pyrolysis at low pressure. Combustion and Flame. 2012;159:905-17.

[140] Li Y, Zhang L, Wang Z, Ye L, Cai J, Cheng Z, et al. Experimental and kinetic modeling study of tetralin pyrolysis at low pressure. Proceedings of the Combustion Institute. 2013;34:1739-48.

[141] Cai J, Zhang L, Yang J, Li Y, Zhao L, Qi F. Experimental and kinetic modeling study of tert-butanol combustion at low pressure. Energy. 2012;43:94-102.

[142] Wang F, Xu Y, Ren J, Li Y. Experimental investigation and modeling of steam cracking of Fischer–Tropsch naphtha for light olefins. Chemical Engineering and Processing: Process Intensification. 2010;49:51-8.

[143] Che D, Li S, Yang W, Jia J, Zheng N. Application of Numerical Simulation on Biomass Gasification. Energy Procedia. 2012;17:49-54.

[144] Boateng AA, Mtui PL. CFD modeling of space-time evolution of fast pyrolysis products in a bench-scale fluidized-bed reactor. Applied Thermal Engineering. 2012;33-34:190-8.

[145] Hu S, Jess A, Xu M. Kinetic study of Chinese biomass slow pyrolysis: Comparison of different kinetic models. Fuel. 2007;86:2778-88.

[146] Li Z, Zhao W, Meng B, Liu C, Zhu Q, Zhao G. Kinetic study of corn straw pyrolysis: comparison of two different three-pseudocomponent models. Bioresource technology. 2008;99:7616-22.

[147] Wang S, Guo X, Liang T, Zhou Y, Luo Z. Mechanism research on cellulose pyrolysis by Py-GC/MS and subsequent density functional theory studies. Bioresource technology. 2012;104:722-8.

[148] Xie J, Zhong W, Jin B, Shao Y, Huang Y. Eulerian–Lagrangian method for three-dimensional simulation of fluidized bed coal gasification. Advanced Powder Technology. 2013;24:382-92.

[149] Gerber S, Behrendt F, Oevermann M. An Eulerian Modeling Approach of Wood Gasification in a Bubbling Fluidized Bed Reactor Using Char as Bed Material. Fuel. 2010;89:2903-17.

[150] Wang X, Jin B, Zhong W. Three-dimensional simulation of fluidized bed coal gasification. Chemical Engineering and Processing: Process Intensification. 2009;48:695-705.

[151] Ahmed II, Gupta AK. Kinetics of woodchips char gasification with steam and carbon dioxide. Applied Energy. 2011;88:1613-9.

[152] Larfeldt J, Leckner B, Melaaen MC. Modelling and measurements of the pyrolysis of large wood particles. Fuel. 2000;79:1637-43.

[153] Babu BV, Chaurasia AS. Modeling for pyrolysis of solid particle: kinetics and heat transfer effects. Energy Conversion and Management. 2003;44:2251-75.

[154] Janse AMC, Westerhout RWJ, Prins W. Modelling of flash pyrolysis of a single wood particle. Chemcial Engineering and Processing. 2000;39:239-52.

[155] Gómez-Barea A, Leckner B. Modeling of biomass gasification in fluidized bed. Progress in Energy and Combustion Science. 2010;36:444-509.

[156] Chen Y, Wang X, He R. Modeling changes of fractal pore structures in coal pyrolysis. Fuel. 2011;90:499-504.

[157] Lam K, Oyedun AO, Cheung K, Lee K, Hui C. Modelling pyrolysis with dynamic heating. Chemical Engineering Science. 2011;66:6505-14.

[158] Lathouwers D, Bellan J. Modeling of dense gas–solid reactive mixtures applied to biomass pyrolysis in a fluidized bed. International Journal of Multiphase Flow. 2001;27:2155-87.

[159] Papadikis K, Gu S, Bridgwater AV. 3D simulation of the effects of sphericity on char entrainment in fluidized beds. Fuel Processing Technology. 2010;91:749-58.

[160] Papadikis K, Gu S, Bridgwater AV. CFD modelling of the fast pyrolysis of biomass in fluidised bed reactors: Modelling the impact of biomass shrinkage Chemical Engneering Journal. 2009;149:417-27.

[161] Papadikis K, Gu S, Bridgwater AV. Computational modelling of the impact of particle size to the heat transfer coefficient between biomass particles and a fluidised bed Fuel Processing Technology. 2010;91:68-79.

[162] Papadikis K, Gu S, Bridgwater AV, Gerhauser H. Application of CFD to model fast pyrolysis of biomass. Fuel Processing Technology. 2009;90:504-12.

[163] Xue Q, Heindel TJ, Fox RO. A CFD model for biomass fast pyrolysis in fluidized-bed reactors. Chemical Engineering Science. 2011;66:2440-52.

[164] Xue Q, Dalluge D, Heindel TJ, Fox RO, Brown RC. Experimental validation and CFD modeling study of biomass fast pyrolysis in fluidized-bed reactors. Fuel. 2012;97:757-69.

[165] Mellin P, Zhang Q, Kantarelis E, Yang W. An Euler-Euler approach to modelling biomass fast pyrolysis in fludized-bed reactors-Focusing on the gas phase. Applied Thermal Engineering. 2013;58:344-53.

[166] Mellin P, Kantarelis E, Yang W. Computational fluid dynamics modeling of biomass fast pyrolysis in a fluidized bed reactor, using a comprehensive chemistry scheme. Fuel. 2014;117:704-15.

[167] Henrik T, Bo L. Thermal conductivity of wood—models for different stages of combustion. biomass and bioenergy. 2002;23:47-54.

[168] Van de Velden M, Baeyens J, Boukis I. Modeling CFB biomass pyrolysis reactors. Biomass and Bioenergy. 2008;32:128-39.

[169] Huber GW, Iborra S, Corma A. Synthesis of Transportation Fuels From Biomass: Chemistry, Catalyst and Engineering. Chemical Reviews. 2006;106:4044-98.

[170] Nilsen MH, Antonakou E, Bouzga A, Lappas A, Mathisen K, Stocker M. Investigation of The Effect of Metal Sites in Me-Al-MCM-41(Me=Fe,Cu or Zn) on the Catalytic Behaviour During the Pryolysis of Wooden Based Biomass. Microporous and Mesoporous Materials. 2007;105:189-203.

[171] Xu Y, Wang TJ, Ma LL, Chen GY. Upgrading of Fast Pyrolysis Liquid Fuel from Biomass over Ru/r-Al2O3 Catalyst. Energy Conversion and Management. 2012;55:172-7.

[172] Xu Y, Wang TJ, Ma LL, Zhang Q, W. L. Upgrading of the Liquid Fuel from Fast Pyrolysis of Biomass over MoNi/r-Al2O3 Catalysts. Applied Energy. 2010;87:2886-91.

[173] Twaiq FA, Zabidi NAM, Mohamd AR, Bhatia S. Catalytic Conversion of Palm Oil over Mesoporous Aluminosilicate MCM-41 for the Production of Liquid Hydrocarbon Fuels. Fuel. 2003;84:105-20.

[174] Zhang H, Xiao R, Jin B, Shen D, Chen R, Xiao G. Catalytic fast pyrolysis of straw biomass in an internally interconnected fluidized bed to produce aromatics and olefins: effect of different catalysts. Bioresource technology. 2013;137:82-7.

[175] Zhang H, Xiao R, Pan Q, Song Q, Huang H. Hydrodynamics of a Novel Biomass Autothermal Fast Pyrolysis Reactor: Flow Pattern and Pressure Drop. Chemical Engineering & Technology. 2009;32:27-37.

[176] Zhang HY, Xiao R, Wang DH, Cho J, He GY, Shao S. Hydrodynamics of a novel biomass autothermal fast pyrolysis reactor: solid circulation rate and gas bypassing. Chem Eng Sci. 2012;181-182:685-93.

[177] Zhang Y, Wang Y, Cai L, Yao C, Gao S, Li C-Z, et al. Dual bed pyrolysis gasification of coal: Process analysis and pilot test. Fuel. 2013;112:624-34.

[178] Kern S, Pfeifer C, Hofbauer H. Gasification of lignite in a dual fluidized bed gasifier — Influence of bed material particle size and the amount of steam. Fuel Processing Technology. 2013;111:1-13.

[179] Li X, Zhang H, Li J, Su L, Zuo J, Komarneni S, et al. Improving the aromatic production in catalytic fast pyrolysis of cellulose by co-feeding low-density polyethylene. Applied Catalysis A: General. 2013;455:114-21.

[180] Li B, Lv W, Zhang Q, Wang T, Ma L. Pyrolysis and catalytic pyrolysis of industrial lignins by TG-FTIR: Kinetics and products. Journal of Analytical and Applied Pyrolysis. 2014;108:295-300.

[181] Atutxa A, Roberto A, Gayubo AG, Martin O, Javier B. Kinetic Description of the Catalytic Pyrolysis of Biomass in a Conical Spouted Bed Reactor. Energy &Fuels. 2005;19:765-74.

[182] Vivek R. Computational Flow Modeling for Chemical Reactor Engineering: Academic Press; 2001.

[183] Kunii D, Levenspiel O. Fluidization Engineering: Elsevier; 1991.

[184] Ergun S, Orning AA. Fluid flow through randomly packed columns and fluidized beds. Industrial and Engineering Chemistry. 1949;41:1179-84.

[185] Wen CY, Yu YH. A generalized method for predicting the minimum fluidization velocity. J AIChE. 1966;12:610-2.

[186] Babu SP, Shah B, Talwalkar A. Fluidization correlations for coal gasification materials-minimum fluidization velocity and fluidized bed expansion. AIChE Symposium Series1978. p. 176-86.

[187] Chitester DC, Kornosky RM, Fan LS, Danko JP. Characteristics of fluidization at high pressure. Chem Eng Sci 1984;39:253.

[188] Gidaspow D. Multiphase flow and fluidization, continuum and kinetic theory descriptions: Academic Press, Inc.; 1994.

[189] Grace JR. Fluidised bed hydrodynamics. Handbook of Multiphase Systems. New York: McGraw-Hill; 1982.

[190] Richardson JF. Incipient fluidization and particulate systems. In: Davidson JF, Harrison D, editors. Fluidization. London: Academic Press; 1971. p. 25-64.

[191] Saxena SC, Vogel GL. The measurement of incipient fluidization in a bed of coarse dolomite at temperature and pressure. Transactions of the Institution of Chemical Engineers 1977;55:184.

[192] Bruchmuller J. Modelling the degradation of particles in fluidised beds: Southampton University; 2011.

[193] Gibilaro LG. Fluidization-dynamics: Butterworth-Herinemann; 2001.

[194] Ariyarathna DGASU. Recommendation of a model for simulation & analysis of the influence of particle size distribution on the simulations of bubbling fluidized beds. Porsgrunn, Norway: Telemark University College; 2008.

[195] Saffman PG. The lift on a small sphere in a slow shear flow. Journal of Fluid Mechanics. 1965;22:385-400.

[196] Drew DA, Lahey RT. Analytical modeling of multiphase flow. In: Roco MC, editor. Particulate two-phase flow. Boston: Butterworth-Heinemann; 1993. p. 509-66.

[197] Schaeffer DG. Instability in the evolutions describing incompressible granular flow. journal of differential equations. 1987;66:19-50.

[198] Syamlal M, Rogers W, O'Brien TJ. MFIX Documentation: volume 1, Theory guide. 1993.

[199] Ogawa S, Umemura A, Oshima N. On the equations of fully fluidized granular materials. Z Angew Math Phys. 1980;31:483-93.

[200] Andrews AT, Loezos PN, Sundaresan S. Coarse-grid simulation of gas-particle flows in vertical risers. Ind Eng Chem Res. 2005;44:6022-37.

[201] Crowe CT, Troutt TR, Chung JN. Numerical models for two-phase turbulent flows. Annu Rev Fluid Mech. 1996;28:11-43.

[202] Enwald H, Peirano E, Almstedt AE. Eulerian two-phase flow theory applied to fluidization. Int J Multiphase Flow. 1996;22:21-66.

[203] Portela LM, Oliemans RVA. Possibilities and limitations of computer simulations of industrial turbulent dispersed multiphase flows. Flow Turbu Combust. 2006;77:381-403.

[204] Lindborg H, Lysberg M, Jakobsen HA. Practical validation of the two-fluid model applied to dense gas-solid flows in fluidized beds. Chem Eng Sci. 2007;62:5854-69.

[205] Di Natale F, Lancia A, Nigro R. Surface-to-bed heat transfer in fliudised beds: Effect of surface shape. Power Technology. 2007;174:75-81.

[206] Syamlal M, Gidaspow D. Hydrodynamics of fluidization: prediction of wall to bed heat transfer coefficients. J AIChE 1985;31:127.

[207] Schmidt A, Renz U. Numerical prediction of heat transfer in fluidized beds by a kinetic theory of granular flows. Int J Therm Sci. 2000;39:871-85.

[208] Lacey PMC. Developments in the theory of particle mixing. Journal of Applied Chemistry. 1954;4:257-68.

[209] Rowe PN, Nienow AW, Agbim AJ. The mechanism by which particles segregate in gas fluidized beds-binary system of near spherical particles. Trans Inst Chem Eng. 1972;50:310-23.

[210] Rowe PN, Nienow AW, Agbim AJ. A preliminary quantitative study of particle segregation in gas fluidized beds-binary system of near spherical particles. Trans Inst Chem Eng. 1972;50.

[211] Syamlal M. The particle-particle drag term in a multiparticle model of fluidization. National Technical Information Service: Springfield; 1987.

[212] Min J, Drake JB, Heindel TJ, Fox RO. Experimental validation of CFD simulation of a lab-scale fluidized-bed reactor with and without side-gas injection. Particle technology and fluidization. 2010;56:1434-46.

[213] Sinclair JL, Jackson R. Gas-particle flow in a vertical pipe with particle–particle interactions. J AIChE. 1989;35:1473-86.

[214] ANSYS Inc. ANSYS FLUENT Theory Guide, Release 13.0,2010.

[215] Fan R, Fox RO. Segregation in polydisperse fluidized beds: Validation of a multi-fluid model. Chemical Engineering Science. 2008;63:272-85.

[216] Liu R, Shen C, Wang J, Liu S. Effect of Particle Size of Corn Stalk Fast Pyrolysis on Physicochemical Properties of Bio-Oil. Journal of Biobased Materials and Bioenergy. 2010;4:391-6.

[217] Sun J, Chen MM. A Theoretical Analysis of Heat Transfer due to Particle Impact. International Journal of Heat Mass Transfer. 1987;31:969-75.

[218] Chang J, Yang S, Zhang K. A Particle-to-Particle Heat Transfer Model for Dense Gas-Solid Fluidized Bed of Binary Mixture. Chemical Engineering Research and Design. 2011;89:894-903.

List of Publications

The publications during the PhD study in University of Southampton are listed:

1） N.H. Dong, L.M. Armstrong, S. Gu, K.H. Luo, Effect of tube shape on the hydrodynamics and tube-to-bed heat transfer in fluidized beds, Applied Thermal Engineering, 60 (2013) 472-479.

2) N.H. Dong, S. Gu, K. Papadikis, L.M. Armstrong, K.H. Luo, Effects of feeding rate on catalytic pyrolysis of sawdust in bubbling fluidized beds, J. Bioprocess Eng. and Biorefinery, 1 (2012) 218-224.

3) N.H. Dong, S. Gu, L.M. Armstrong, K. Papadikis, K.H. Luo, CFD Modelling of thermo-chemical process in catalytic pyrolysis of sawdust in bubbling fluidised beds, In proceedings of CHT-12. Bath, UK, July 1-6 (2012)

4) D.K. Shen, S. Gu, N.H. Dong, A.V. Bridgwater, The thermal conversion of cellulose and hemicellulose in thermogravimetric apparatus and a fluidized-bed reactor, Bioten, Aston, UK, September 21-23 (2010)